AN ABSTRACT OF THE DISSERTATION OF

John M. Lahmann for the degree of Doctor of Philosophy in Chemical Engineering presented on September 7, 2018.

Title: Blood Processing Technologies for Cryopreserved Transfusion Products and Extracorporeal Treatment Applications.

Abstract approved: _____

Adam Z. Higgins

There is a significant need for technological advancement in blood processing. New technologies in rapid processing of frozen blood products could significantly improve management of the blood supply chain in the United States by enabling on-demand use of frozen blood products that can be stored for 10 years instead of the current 6 weeks of refrigerated shelf life. In addition, advancements in blood processing for the extracorporeal treatment of sepsis could potentially save over 100,000 lives every year in the United States alone. Here we describe a new mathematical modeling approach for the design of procedures to rapidly remove the cryoprotectant glycerol from frozen-thawed red blood cells. We employ a concentration dependent permeability parameter to account for the varied glycerol transport rates of red blood cells over the wide range of glycerol concentrations encountered during deglycerolization. Additionally, variability of glycerol permeability is addressed by optimizing procedures to account for faster and slower responding cells within the population. These mathematically optimized procedures resulted in a significant reduction in hemolysis when compared to previous procedures that used a fixed value for permeability and did not account for cell variability. Our

findings here indicate higher variability than anticipated within the cell population and between donors. Although ultra-rapid (< 1 min) removal of glycerol was not achieved, we achieved a significant reduction in processing times compared to the current standard. In addition to advancements in cryopreservation of blood products, new technologies were developed for applications in the extracorporeal treatment of sepsis. We presented a new hot embossing rapid prototyping approach for creation of high aspect ratio microfluidic devices in polycarbonate. We used a model system to test the effects of bifurcated microchannels on the removal of endotoxin from blood. We saw no significant effect of bifurcations on endotoxin removal, but reduction of channel width resulted in a significant increase in removal efficiency with up to 80% single pass clearance in the smallest width channel. This work forwards understanding on design of absorption-based blood perfusion devices to harness the unique flow properties of blood in microchannels.

Blood Processing Technologies for Cryopreserved Transfusion Products and Extracorporeal Treatment Applications

by
John M. Lahmann

A DISSERTATION

submitted to

Oregon State University

in partial fulfillment of
the requirements for the
degree of

Doctor of Philosophy

Presented September 7, 2018
Commencement June 2019

Doctor of Philosophy dissertation of John M. Lahmann presented on September 7, 2018.

APPROVED:

Major Professor, representing Chemical Engineering

Head of the School of Chemical, Biological, and Environmental Engineering

Dean of the Graduate School

I understand that my dissertation will become part of the permanent collection of Oregon State University libraries. My signature below authorizes release of my dissertation to any reader upon request.

John M. Lahmann, Author

ACKNOWLEDGEMENTS

First and foremost, I would like to thank my advisor, Dr. Adam Higgins, for all his support during this rather long journey. When things were difficult, his encouragement, scientific insight, and commitment to my professional success supported me, allowing me to realize my goals. I would also like to thank my committee members for their advice, guidance, and assistance. Having such a wealth of knowledge available to me from leaders in such diverse fields was invaluable. Additionally, I would like to thank all my collaborators and those who provided me with training and allowed me to use their equipment and resources. A very big thank you to all our lab interns throughout my graduate career. Their work, which could often feel tedious, resulted in valuable scientific data. I would like to thank all those who donated blood for these projects, your painful sacrifice is greatly appreciated. Thank you to my mom and dad for their support, they have always valued my pursuit of education and have always been there with encouragement when the going got tough. I would also like to thank my brother for all his graphic design help throughout the years and for empathetically listening to my problems and providing reassurance. Thank you to my in-laws for providing my family with the flexibility for me to pursue this PhD. I cannot thank you enough for your generosity and immeasurable help. Finally, I would like to thank my wife Emily. You have been by my side through the good and bad, thick and thin, and without you none of this would have been possible.

CONTRIBUTION OF AUTHORS

Chapter 2 was written under the guidance of Dr. Adam Higgins. Dr. James Benson developed the mathematical model discussed in Section 2.4.6 and used in Section 2.5.5. Dr. Benson also wrote Section 2.7. Chapter 3 was written with the guidance and advice of Dr. Adam Higgins. Dr. Higgins and Dr. Benson developed the mathematical modeling approach presented in Section 3.3.2. Cynthia Cruz-Sanchez assisted in testing the mathematically optimized deglycerolization procedures in Chapter 3. The manuscript of Chapter 4 was written with the advice of Dr. Adam Higgins. Jun Yang fabricated the lamina used in the experiments in Chapter 4. Dr. Kendra Sharp provided guidance on device design in Chapter 4 and Dr. Kate Schilke assisted with the coating strategy. Jolynn Meza Wynkoop assisted with the data collection in Appendix A.

TABLE OF CONTENTS

Page

Chapter 1: Introduction ..…… 1

1.1. Technologies for Cryoprotectant Removal from Frozen Blood ……...… 2

1.2. Blood Processing Technologies for the Treatment of Sepsis ……..... 4

Chapter 2: Concentration Dependence of the Cell Membrane Permeability to Cryoprotectant and Water and Implications for Design of Methods for Post-thaw Washing of Human Erythrocytes ……...……..……..… 6

2.1 Abstract …….……. 7

2.2 Introduction ……..……. 7

2.3 Membrane Transport Models ……...… 11

2.4 Water Transport in RBCs ……. 21

2.5 Glycerol Transport in RBCs ……. 30

2.6 Interaction Between Water and Glycerol Transport ……..... 36

2.7 Relative Rates of Water and Glycerol Transport ……. 37

2.8 Discussion and Conclusion ……..…… 40

2.9 Acknowledgements …….. 45

Chapter 3: Implications of Variability in Cell Membrane Permeability for Design of Methods to Remove Glycerol from Frozen-thawed Erythrocytes …..……...…… 46

3.1 Abstract …….……... 47

3.2 Introduction ……...……... 48

3.3 Materials and Methods ……....… 51

3.4 Results ……..…… 63

3.5 Discussion …… 73

TABLE OF CONTENTS (Continued)

Page

3.6 Conclusions ……..……..... 81

3.7 Acknowledgements …….. 82

Chapter 4: Effect of Bifurcations on the Clearance of Biotinylated Lipopolysaccharide (LPS) from Blood in High Aspect Ratio Microchannels ……...……..... 83

4.1 Abstract …… 84

4.2 Introduction …….. 84

4.3 Materials and Methods ……. 87

4.4 Results ...…….…….…. 94

4.5 Discussion ……..... 97

4.6 Conclusion …….. 102

4.7 Acknowledgements …… 103

Chapter 5: Conclusion and Future Directions ……....…..…….. 104

5.1. Technologies for Cryoprotectant Removal from Frozen Blood ……..... 104

5.2. Blood Processing Technologies for the Treatment of Sepsis ……..... 107

Appendix A. ……... 109

Appendix B. ……... 114

Bibliography ……..……...…. 126

LIST OF FIGURES

Figure Page

Figure 2.1. Solute transport through the phospholipid bilayer ……..……..… 13

Figure 2.2. Water transport through a water-specific pore ……..……...…. 15

Figure 2.3. Solute transport mediated by a carrier ……...……..... 17

Figure 2.4. Water and solute transport through a co-transporting membrane channel ……...……..… 21

Figure 2.5. Effect of solution osmolality on the osmotic water permeability of human RBCs at room temperature, 20°C–26°C ……...……..…… 29

Figure 2.6. Effect of solution osmolality on the glycerol permeability of human RBCs at room temperature, 20°C–25°C ……...…….…… 35

Figure 2.7. Plot of the nondimensional permeability parameter b (solid line), its limiting values (dotted lines), and the time scale parameter τ (dashed line) as a function of osmolality …….……...…….…… 39

Figure 2.8. Predictions of osmotically active cell volume during deglycerolization using either constant water and glycerol permeability parameters (A) or the concentration-dependent permeability models presented in sections 2.4.6 and 2.5.5 above (B) ……...……...…….. 43

Figure 3.1. Measurement of cell membrane permeability to glycerol …….…… 63

Figure 3.2. Effect of solution osmolality on the glycerol permeability of human RBCs at room temperature, 20°C-25°C, from the literature and this study ….….. 65

Figure 3.3. Cell volume predictions for the 3-step deglycerolization procedure optimized using concentration dependent permeability values …….……. 67

Figure 3.4. Hemolysis results for the 3-step optimized deglycerolization procedure with a glycerol permeability range of ±50% of the concentration dependent permeability parameter presented in this work……..…….. 69

Figure 3.5. Results of the time extension of a more conservative 2-step deglycerolization procedure …… 71

Figure 4.1. Process for creating a microfluidic lamina …… 89

LIST OF FIGURES (Continued)

Page

Figure 4.2. Schematic view and photo of device ……..……..……...….. 91

Figure 4.3. A lamina for the 250 μm width channels under a dissection microscope …. 95

Figure 4.4. Calibration curve for LPS-biotin diluted into 1x PBS using the modified ELISA protocol ……..…. 96

Figure 4.5. Percent LPS-biotin removal for the tested geometries …….. 97

Figure A.1. Temperature effects on scaling of the glycerol permeability parameter 109

Figure A.2. Effect of equilibration time in the first step of a three-step deglycerolization procedure on hemolysis at room temperature (squares) vs. 37 °C (dots) ……... 111

Figure A.3. Effect of equilibration time at 45 °C for a single donor (triangles) on hemolysis …….. 112

Figure B.1. Ideal operation of the bifurcations …….. 115

Figure B.2. Simulations of fluid flow at the first bifurcation for a lamina design with asymmetrical triangular “Z-shaped” headers ……... 116

Figure B.3. Simulations of fluid flow at the first bifurcation for a simpler symmetrical triangular header design ……... 117

Figure B.4. Simulations of fluid flow at the first bifurcation for wider lamina with a subdivided header ……..… 117

Figure B.5. Bifurcation induced mixing in low and high aspect ratio microchannels ... 120

Figure B.6. Overview of the photochemical machining and hot embossing process … 121

Figure B.7. The first “heat lamination” method for creating a high aspect ratio PEI master …… 123

Figure B.8. Magnified view of a high aspect ratio polycarbonate lamina showing the deeper header and the uniformly tall fins that form the channels ……. 124

LIST OF TABLES

Table Page

Table 2.1. Pathways for human erythrocyte glycerol and water transport and their relative contributions at room temperature ……...……...…….. 41

Table 3.1. Initial and final concentrations of permeating and non-permeating solutes for Coulter counter permeability measurements ……..……... 52

Table 3.2. Deglycerolization methods and solution compositions ……..…… 62

Table 4.1. Device fabrication parameters …… 88

Blood Processing Technologies for Cryopreserved Transfusion Products and Extracorporeal Treatment Applications

Chapter 1: Introduction

Since our earliest days, humans have looked to the blood as the source of health or illness. Ancient cultures often attributed sickness to an imbalance of "humours" in the blood [1]. The Greek philosopher Galen recommended bloodletting as a routine method of medical treatment, even noting from which parts of the body to let blood in order to treat specific diseases [2]. The earliest known document on surgery, a 3000 BC Egyptian manuscript, discussed the identification of systemic infection and its origins in the blood [3]. As scientific research progressed, interest in blood and blood processing applications progressed as well. William Harvey conducted the first known experiments in blood transfusion in 1666, and James Blundell in 1818 successfully transfused blood between two human donors for the first time [4]. While many medical treatments of the ancient world were rooted in superstition and other falsehoods, it is clear the importance of blood to the health and vitality of a person was understood far before modern science and medicine could explain its real function.

The first transfusions with refrigerated blood took place in the early 1900s [5, 6]. It was during this time that important discoveries in blood anticoagulants were made which were critical to both blood banking and blood processing technology [6, 7]. The ability to hypothermically store whole blood in anticoagulant without clotting led to the formation of modern blood banking systems [8]. In a similar fashion, anticoagulant treatment

allowed blood to be flowed through extracorporeal circuits for various treatments; the first known extracorporeal circuit being a cardiopulmonary bypass system called a heart and lung machine [9]. These early discoveries gave way to modern transfusion medicine and modern blood processing with products and technologies such as frozen platelets, frozen plasma, frozen red blood cells, kidney dialysis, and ECMO.

In our postmodern world, the development of systems and technology for blood storage and blood processing means that when every 2 seconds someone needs blood in the United States, there are blood products available to that individual on demand [10]. Additionally, formerly fatal conditions such as kidney failure are now considered chronic illnesses due to the prevalence of kidney dialysis facilities throughout the United States [11]. While great strides have clearly been made in blood storage and blood processing technology, there remain many shortcomings in current technology and many challenges to be solved. The need for blood products continues to outstrip their availability, due in part to the short storage life of refrigerated blood [12]. There are many diseases of the blood for which new extracorporeal processing devices could provide treatment options. This work aims to further the development of frozen blood storage through the development of faster cryoprotectant removal techniques and to use microfluidic blood processing technology for the treatment of sepsis.

1.1. Technologies for Cryoprotectant Removal from Frozen Blood

Since the 1960s, cryopreservation of red blood cells (RBCs) in 40% glycerol, a cryoprotectant, has been used for long-term blood storage [13]. Although cryopreserved blood is capable of being stored for up to 10 years, because of the laborious and time-

consuming post-thaw processing to remove the glycerol, frozen blood is only used in banking of rare blood types and in some military applications [14]. As more than 12 million units of packed RBCs are transfused every year in the United States, development of a long-term storage solution that still allows rapid availability of needed units of blood would be revolutionary [15]. Removal of glycerol in a timely manner and without significant cell lysis continues to stymie the development of a commercial device that would enable rapid use of cryopreserved blood [16, 17]. The current standard is the ACP215 cell washer, which uses a closed loop centrifugal bowl system to expose cells to saline wash steps, gradually removing excess glycerol and concentrating cells [18]. While successful, this system requires approximately 45 minutes to deglycerolize just one unit of blood, an unsustainable time in the presence of immediate need [14].

Recent research in our lab has focused on development of a device that can carry out ultra-rapid deglycerolization in a matter of minutes [19]. Furthermore, if these time scales could be achieved it may be possible to create a continuous deglycerolization device that could deglycerolize blood on demand for direct infusion into a patient [20]. Although no device currently exists that can prepare frozen blood in this manner, there have been attempts to bring this technology closer to reality through use of advanced mathematical modeling for design of rapid cryoprotectant removal procedures that can be applied to the development of novel blood washing devices [20, 21].

This work aims to reduce deglycerolization times by building on previous mathematical optimization strategies and providing new insight into cell membrane transport phenomena by examining the physiological processes involved in erythrocyte cryoprotectant transport. These analyses led to the development of a concentration

dependent permeability parameter for modeling glycerol transport in erythrocytes which is discussed in detail in Chapter 2. This is expanded upon in Chapter 3 where testing of deglycerolization protocols designed with the concentration dependent model revealed a higher than expected variability of glycerol permeability values within the cell population. While this presents a challenge to the development of ultra-rapid deglycerolization procedures, substantial progress in reduction of deglycerolization times was achieved.

1.2. Blood Processing Technologies for the Treatment of Sepsis

Sepsis is a condition responsible for approximately 1 million hospitalizations and 125,000 deaths every year in the United States [22]. The most common cause of sepsis is spread of a bacterial infection to the blood, causing symptoms including fever, low blood pressure, increased heart rate, and slow respiratory rate; if left untreated sepsis will lead to organ dysregulation, shock, and death [23]. Currently, primary treatment of sepsis includes aggressive antibiotic treatment alongside supportive antipyretics and vasopressors [24]. Treatment remains difficult however, as though bacteria may be eliminated from the blood, endotoxins (fragments of bacterial membrane components) remain in the bloodstream and continue to cause life-threatening symptoms [25].

Several extracorporeal blood processing devices have been proposed as potential treatments for sepsis including hemofiltration, plasmapheresis, adsorption of the inflammatory cytokines, and direct adsorption of endotoxin. Although there are no treatment devices approved for use in the United States, endotoxin adsorption devices have been used for many years in Japan and Europe with varying degrees of clinical

success [26]. Demand for more effective treatment technologies has turned research to microfluidic technology with the goal of increasing the efficiency of pathogen removal by harnessing the unique flow properties of blood in microchannel devices [27-30]. Additionally, these devices promise high throughput due to their scalable nature through parallelization [27].

Current research lacks significant examination of the effects of channel geometry at the microscale on the effectiveness of absorption of blood constituents. Chapter 4 addresses this deficiency by testing the effects of bifurcated flow in microchannels to determine if induced mixing of blood can increase the efficiency of these devices. A new method for rapid prototyping of microfluidic devices in thermoplastics through hot embossing and laser machining is presented. Additionally, a model system to test the effectiveness of these devices for absorbing endotoxin from blood is described. These advancements may allow for the design of more efficient adsorption devices for removal of blood constituents.

Chapter 2: Concentration Dependence of the Cell Membrane Permeability to Cryoprotectant and Water and Implications for Design of Methods for Post-thaw Washing of Human Erythrocytes

John M. Lahmann, James D. Benson, Adam Z. Higgins

Journal: *Cryobiology*

Address: https://doi.org/10.1016/j.cryobiol.2017.12.003

Date: Published February 2018

2.1 Abstract

For more than fifty years the human red blood cell (RBC) has been a widely studied model for transmembrane mass transport. Existing literature spans myriad experimental designs with varying results and physiologic interpretations. In this review, we examine the kinetics and mechanisms of membrane transport in the context of RBC cryopreservation. We include a discussion of the pathways for water and glycerol permeation through the cell membrane and the implications for mathematical modeling of the membrane transport process. In particular, we examine the concentration dependence of water and glycerol transport and provide equations for estimating permeability parameters as a function of concentration based on a synthesis of literature data. This concentration-dependent transport model may allow for design of improved methods for post-thaw removal of glycerol from cryopreserved blood. More broadly, the consideration of the concentration dependence of membrane permeability parameters may be important for other cell types as well, especially for design of methods for equilibration with the highly concentrated solutions used for vitrification.

2.2 Introduction

Membrane transport modeling has been used for decades to design and interpret methods for cell cryopreservation. Currently there are two main cryopreservation approaches, slow freezing and vitrification, and in both cases cell membrane transport plays a critical role. Slow freezing involves an initial step in which cells are loaded with a relatively low CPA concentration (~1 M), followed by freezing, thawing and removal of CPA. The addition and removal of CPAs results in transport of both water and CPA

across the cell membrane, which can cause damaging changes in cell volume. During freezing, the formation of ice removes liquid water from the extracellular medium and increases the solute concentration. This drives efflux of water from the cells. Vitrification differs from slow freezing in that high CPA concentrations (typically >5 M) are used to completely prevent formation of ice. Thus, for vitrification methods membrane transport is mainly important during CPA addition and removal.

Previous studies have typically assumed that the permeability of the cell membrane to water and CPA is constant and independent of solute concentration. However, the evidence suggests that the water permeability decreases as the solute concentration increases [31-35]. The effect of solute (or CPA) concentration on CPA permeability has received less attention in the literature. Most previous studies of the concentration dependence of CPA permeability involve permeability measurement for CPA concentrations less than 2 M [36, 37]. These studies have yielded conflicting results. In the case of human erythrocytes, the glycerol permeability has been investigated for concentrations up to 4 M, and a substantial decrease in permeability (by more than a factor of 5) was observed [38]. Such a large change in permeability has significant implications for design of CPA equilibration procedures. This is particularly true for vitrification methods, which involve large changes in CPA concentration and the concomitant potential for large changes in the membrane permeability to CPA. The concentration dependence of CPA permeability is also likely to be important for design of CPA addition and removal methods for human erythrocytes, which are currently cryopreserved using a high glycerol concentration.

In the 1950s it became well established that the addition of large concentrations of glycerol to erythrocytes could prevent freezing injury and allow for the bulk storage of blood [39, 40]. Shortly after, storage in 40% glycerol and freezing at −80 °C became the established standard for banking of frozen blood in North America. This established standard, set forth by the American Association of Blood Banks, has persisted since then due to the ease and safety of the cryopreservation process. However, removal of such large quantities of glycerol prior to transfusion is difficult, requiring expensive machinery and about an hour per unit of blood.

Glycerol is not inherently toxic to humans. However, removal of glycerol prior to transfusion, known as deglycerolization, is imperative in order to avoid post-transfusion hemolysis due to rapid influx of water into the RBCs and concomitant excessive swelling. The current practice to reduce deglycerolization-associated lysis is a post-thaw washing protocol using a series of saline solutions that facilitate the safe removal of glycerol from the cells by preventing excessive water influx [41, 42]. While this method has been used with great success for many years, the slow nature of the process generally does not allow for immediate use of frozen–thawed blood in emergencies and typically relegates its use to banking of rare blood types [43]. Recently there has been some renewed interest in speeding up the deglycerolization process through mathematical optimization and development of new blood processing technologies [19-21].

In our group, we have been exploring the potential for using mathematical modeling of water and glycerol transport across the RBC membrane to design ultra-rapid methods for deglycerolization. Our initial predictions suggested that glycerol could be safely removed in less than a minute without causing excessive cell volume changes.

However, experimental testing of these ultra-rapid deglycerolization methods resulted in hemolysis values that were higher than expected [19]. Therefore, we have sought to more systematically examine the biophysical properties of RBCs that are relevant to deglycerolization, including the cell membrane permeability to water and glycerol and the concentration dependence of these parameters.

The human RBC is a widely-used model system for studying transmembrane transport of water and solutes such as glycerol. The literature is extensive, spans several decades, and involves both biophysical and molecular investigations of transport kinetics and mechanisms. A great deal of information has become available regarding the mechanisms of water and glycerol transport, including the aquaporins and other transport proteins responsible [44-48]. This improved mechanistic understanding of the transport process has implications for selection of an appropriate membrane transport model. We are unaware of any single source that synthesizes all of this information.

In this review, we systematically explore the kinetics and mechanisms of membrane transport of water and glycerol in human RBCs, and provide a discussion of these transport mechanisms in the context of the two most widely used membrane transport models in the cryobiology literature: the two-parameter model and the Kedem-Katchalsky model [49]. In addition, we examine the concentration dependence of the cell membrane permeability to water and glycerol. It is our hope that this review will be useful for others who are interested in developing improved deglycerolization methods for human RBCs. It is also expected to be a useful resource for those interested in membrane transport modeling in general, as we provide an analysis of biological transport mechanisms and their relationship to membrane transport modeling strategies.

2.3 Membrane Transport Models

2.3.1. The two-parameter model

The simplest transport model for the case of a single permeable solute is known as the two-parameter (2P) model. It has its roots in work by Jacobs [50, 51], and is commonly expressed in terms of concentration driving forces as follows:

$$\frac{dW}{dt} = -L_{\mathrm{p}}ART\left(C_{\mathrm{n}}^{\mathrm{e}} + C_{\mathrm{s}}^{\mathrm{e}} - C_{\mathrm{n}}^{\mathrm{i}} - C_{\mathrm{s}}^{\mathrm{i}}\right),$$

$$\frac{dS}{dt} = P_{\mathrm{s}}A\left(C_{\mathrm{s}}^{\mathrm{e}} - C_{\mathrm{s}}^{\mathrm{i}}\right),$$

where W is the volume of intracellular water, S is the moles of intracellular permeating solute, L_{p} is the hydraulic conductivity, P_{s} is the solute permeability, A is the cell surface area, R is the ideal gas constant, T is the absolute temperature, C is the solute concentration, the superscripts *e* and *i* refer to extra- and intracellular conditions, respectively and the subscripts *n* and *s* denote nonpermeating and permeating solutes, respectively.

The above equations are based on the assumption that the fluxes of water and solute are non-interacting. There are several physical transport mechanisms that satisfy this criterion, including transport of water and solute via diffusion across the phospholipid bilayer, as well as transport of water and solute via separate transporter mechanisms (e.g., channels or carriers). Below, we describe the coefficients of the 2P model in terms of these physical transport mechanisms.

2.3.1.1. Bilayer diffusion

Our description of bilayer diffusion follows that given by Finkelstein [52]. The physical mechanism for diffusion of a solute across the bilayer is illustrated in Figure 2.1. At the membrane edges, the solute is assumed to be at chemical equilibrium and thus the concentration of solute just outside the membrane is related to the concentration just inside the membrane using the partition coefficient K_s:

$$K_s = \frac{C^e_{s,bilayer}}{C^e_s} = \frac{C^i_{s,bilayer}}{C^i_s}.$$

According to Fick's law, the diffusion of solute across the membrane is proportional to the concentration driving force:

$$\frac{dS}{dt} = D_s A\left(\frac{C^e_{s,bilayer} - C^i_{s,bilayer}}{\delta}\right),$$

where D_s is the diffusivity of the solute within the membrane bilayer, and δ is the membrane thickness. Combining these equations yields

$$\frac{dS}{dt} = \frac{D_s K_s A}{\delta}\left(C^e_s - C^i_s\right).$$

Comparison of this equation with the original 2P model reveals that in the case of bilayer diffusion the solute permeability is equal to

$$P_s = \frac{D_s K_s}{\delta}.$$

Similar reasoning can be used to show that the water permeability P_w is equal to

$$P_w = \frac{D_w K_w}{\delta},$$

where D_w is the diffusivity of water within the membrane bilayer and K_w is the partition coefficient for water. Typically the hydraulic conductivity L_p is used in the 2P model rather than the water permeability P_w. It is simple to convert between these parameters:

$$L_p = \frac{P_w \bar{v}_w}{RT}, \tag{1}$$

where $\bar{v}_w$ is the molar volume of water.

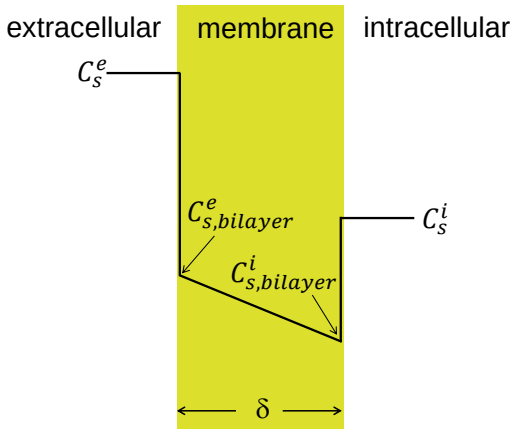

Figure 2.1. Solute transport through the phospholipid bilayer. *The solute partitions into the hydrophobic bilayer at the membrane edge and then diffuses down its concentration gradient.*

2.3.1.2. Transport through a water-specific pore

Our description of transport through a water-specific pore also follows that given by Finkelstein [52]. Figure 2.1 illustrates the driving forces for transport through a transmembrane pore that allows passage of water but excludes all solutes. Because solute molecules cannot enter the pore, there is a discontinuity in solute concentration at each of the pore edges. If we assume chemical equilibrium at the pore edges, then this discontinuity in concentration must be balanced by a discontinuity in pressure.

Specifically, the pressure must be higher outside of the pore than it is inside the pore in order to compensate for the tendency of water to flow from low to high solute concentration. This is exactly analogous to the usual description of osmotic pressure, in which pure water is separated from an aqueous solution by a semipermeable membrane, and a hydrostatic pressure develops in order to compensate for the tendency of water to flow from the pure water into the relatively solute-rich environment on the other side of the membrane. We can use the definition of osmotic pressure for an ideal and dilute solution to determine the pressure at the extracellular and intracellular pore edges, respectively:

$$P^{\mathrm{e}} - P^{\mathrm{e}}_{\mathrm{pore}} = RT(C^{\mathrm{e}}_{\mathrm{n}} + C^{\mathrm{e}}_{\mathrm{s}}),$$

$$P^{\mathrm{i}} - P^{\mathrm{i}}_{\mathrm{pore}} = RT\left(C^{\mathrm{i}}_{\mathrm{n}} + C^{\mathrm{i}}_{\mathrm{s}}\right).$$

If the pressure is the same in the extracellular and intracellular solutions (i.e., $P^{\mathrm{e}} = P^{i}$), then the pressure gradient driving flow of water through the pore is

$$P^{\mathrm{e}}_{\mathrm{pore}} - P^{\mathrm{i}}_{\mathrm{pore}} = -RT\left(C^{\mathrm{e}}_{\mathrm{n}} + C^{\mathrm{e}}_{\mathrm{s}} - C^{\mathrm{i}}_{\mathrm{n}} - C^{\mathrm{i}}_{\mathrm{s}}\right).$$

There are several possible approaches for modeling flow of water through the pore in response to this pressure gradient. Perhaps the simplest is to assume that the pore can be modeled as a macroscopic cylinder, for which the Hagen-Poiseuille equation yields

$$Q = \frac{\left(P^{\mathrm{e}}_{\mathrm{pore}} - P^{\mathrm{i}}_{\mathrm{pore}}\right)\pi r^4}{8\eta\delta} = -\frac{RT\left(C^{\mathrm{e}}_{\mathrm{n}} + C^{\mathrm{e}}_{\mathrm{s}} - C^{\mathrm{i}}_{\mathrm{n}} - C^{\mathrm{i}}_{\mathrm{s}}\right)\pi r^4}{8\eta\delta},$$

where Q is the volumetric flow rate through the pore, r is the pore radius and η is the viscosity of fluid in the pore. If there are n pores in the cell membrane and water only crosses the membrane via the pore pathway, the change in cell water volume is

$$\frac{dW}{dt} = nQ = -\frac{n\pi r^4}{8\eta\delta} RT\left(C_{\mathrm{n}}^{\mathrm{e}} + C_{\mathrm{s}}^{\mathrm{e}} - C_{\mathrm{n}}^{\mathrm{i}} - C_{\mathrm{s}}^{\mathrm{i}}\right).$$

Comparison of this equation with the original 2P model shows that, in the case of osmotic transport through a water-specific pore, the hydraulic conductivity is

$$L_{\mathrm{p}} = \frac{n\pi r^4}{8\eta\delta A}.$$

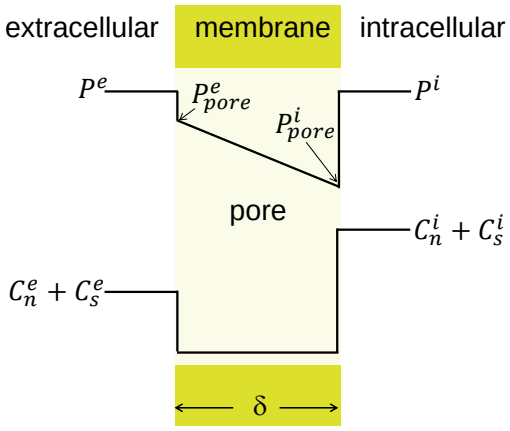

Figure 2.2. Water transport through a water-specific pore. *Exclusion of both permeating and nonpermeating solutes from the pore leads to a discontinuity in concentration, which is balanced by discontinuity in pressure. Flow of water through the pore is driven by a pressure gradient.*

2.3.1.3. Transport via a carrier protein

There are several possible approaches for modeling carrier-mediated transport. We will use the relatively simple modeling approach presented by Kolber and LeFevre, which assumes that the solute and carrier reach chemical equilibrium at the membrane edges and that the resulting solute-carrier complex diffuses across the membrane [53].

This process is illustrated in Figure 2.3. The molar flow rate of solute can be expressed in terms of the concentration gradient of solute-carrier complexes:

$$\frac{dS}{dt} = D_{\mathrm{sc}} A \frac{\left(C_{\mathrm{sc}}^{\mathrm{e}} - C_{\mathrm{sc}}^{\mathrm{i}}\right)}{\delta},$$

where D_{sc} is the diffusivity of the solute-carrier complex in the membrane. At the membrane edges, the concentration of solute-carrier complexes can be expressed in terms of the equilibrium constant for complex dissociation K_{sc}:

$$C_{\mathrm{sc}}^{\mathrm{e}} = \frac{C_{\mathrm{s}}^{\mathrm{e}} C_{\mathrm{c}}^{\mathrm{e}}}{K_{\mathrm{sc}}}; \quad C_{\mathrm{sc}}^{\mathrm{i}} = \frac{C_{\mathrm{s}}^{\mathrm{i}} C_{\mathrm{c}}^{\mathrm{i}}}{K_{sc}}.$$

The flux of solute-carrier complexes across the membrane must be balanced by an equal and opposite flux of free carriers. Assuming D_{sc} is equal to the diffusivity of free carrier, equal and opposite concentration gradients will be established across the cell membrane (see Figure 2.3), which results in a constant total carrier concentration: $C_{\mathrm{c,total}} = C_{\mathrm{sc}}^{\mathrm{e}} + C_{\mathrm{c}}^{\mathrm{e}} = C_{\mathrm{sc}}^{\mathrm{i}} + C_{\mathrm{c}}^{\mathrm{i}}$. Thus, the concentration of solute-carrier complexes can be expressed as

$$C_{\mathrm{sc}}^{\mathrm{e}} = \frac{C_{\mathrm{c,total}} C_{\mathrm{s}}^{\mathrm{e}}}{K_{\mathrm{sc}} + C_{\mathrm{s}}^{\mathrm{e}}}; \quad C_{\mathrm{sc}}^{\mathrm{i}} = \frac{C_{\mathrm{c,total}} C_{\mathrm{s}}^{\mathrm{i}}}{K_{\mathrm{sc}} + C_{\mathrm{s}}^{\mathrm{i}}}.$$

Substituting this into the above differential equation yields

$$\frac{dS}{dt} = \frac{D_{\mathrm{sc}} A C_{\mathrm{c,total}}}{\delta} \left(\frac{C_{\mathrm{s}}^{\mathrm{e}}}{K_{\mathrm{sc}} + C_{\mathrm{s}}^{\mathrm{e}}} - \frac{C_{\mathrm{s}}^{\mathrm{i}}}{K_{\mathrm{sc}} + C_{\mathrm{s}}^{\mathrm{i}}} \right),$$

which can be simplified to

$$\frac{dS}{dt} = \frac{D_{\mathrm{sc}} A C_{\mathrm{c,total}} K_{\mathrm{sc}}}{\delta (K_{\mathrm{sc}} + C_{\mathrm{s}}^{\mathrm{e}})(K_{\mathrm{sc}} + C_{\mathrm{s}}^{\mathrm{i}})} \left(C_s^{\mathrm{e}} - C_{\mathrm{s}}^{\mathrm{i}}\right).$$

Comparison of this equation with the original 2P model reveals that, in the case of carrier-mediated solute transport, the apparent solute permeability is a function of the intracellular and extracellular solute concentrations:

$$P_{\mathrm{s}} = \frac{D_{sc} C_{\mathrm{c,total}} K_{\mathrm{sc}}}{\delta (K_{\mathrm{sc}} + C_{\mathrm{s}}^{\mathrm{e}})(K_{\mathrm{sc}} + C_{\mathrm{s}}^{\mathrm{i}})}.$$

Examination of this equation shows that for low solute concentrations ($C_s << K_{sc}$), the value of P_s is essentially constant and equal to $D_{sc}C_{c,total}/\delta K_{sc}$. However, as the solute concentration becomes large ($C_s >> K_{sc}$), the value of P_s approaches zero. This is because the carriers become saturated at high solute concentrations. Saturation at high solute concentrations is a key feature of the carrier-mediated transport mechanism.

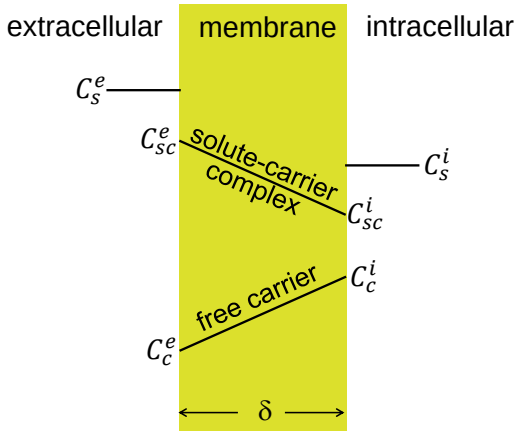

Figure 2.3. Solute transport mediated by a carrier. *At the membrane edges, solute and free carrier combine to form a solute-carrier complex. This complex then diffuses across the membrane down its concentration gradient.*

2.3.2 The Kedem and Katchalsky model

Although it is more complicated than the 2P model, the Kedem-Katchalsky (KK) model [54] is commonly used in the RBC permeability literature. The KK model

behaves similarly to the 2P model, but accounts for interaction between solute and water fluxes via an interaction parameter σ. The typical form of the KK model is

$$\frac{d(W + \bar{v}_s S)}{dt} = -L_p ART\left(C_n^e - C_n^i + \sigma\left(C_s^e - C_s^i\right)\right),$$

$$\frac{dS}{dt} = P_s A\left(C_s^e - C_s^i\right) + (1-\sigma)\left(\frac{C_s^e + C_s^i}{2}\right)\frac{d(W + \bar{v}_s S)}{dt},$$

where $\bar{v}_s$ is the molar volume of solute. This model is derived from the theory of linear irreversible thermodynamics, which assumes that fluxes are proportional to thermodynamic driving forces. To arrive of the final equations shown above, the thermodynamic driving forces were converted to the relevant solute concentrations by assuming that solutions were ideal and dilute and that the system was near equilibrium. The KK model is particularly useful in cases where water and solute cross the cell membrane through the same pore.

2.3.2.1. Water and solute transport through a co-transporting pore

Water and solute fluxes would be expected to interact in a pore that allows passage of both water and solute. Figure 2.4 illustrates the driving forces within such a co-transporting channel. Because nonpermeating solutes cannot enter the pore, the concentration of nonpermeating solute within the pore is equal to zero. However, permeating solutes can enter the pore to some extent, resulting in a total solute concentration within the pore that is nonzero. The degree to which the permeating solute

can enter the pore can be described using an equilibrium constant $K_{s,pore}$, where a value of $K_{\mathrm{s,pore}} = 0$ corresponds with complete exclusion of the solute from the pore:

$$K_{\mathrm{s,pore}} = \frac{C^{\mathrm{e}}_{\mathrm{s,pore}}}{C^{\mathrm{e}}_{\mathrm{s}}} = \frac{C^{\mathrm{i}}_{\mathrm{s,pore}}}{C^{\mathrm{i}}_{\mathrm{s}}}\,.$$

The discontinuity in total solute concentration at the pore edges must be compensated by a discontinuity in pressure:

$$P^{\mathrm{e}} - P^{\mathrm{e}}_{\mathrm{pore}} = RT\left(C^{\mathrm{e}}_{\mathrm{n}} + C^{\mathrm{e}}_{\mathrm{s}} - C^{\mathrm{e}}_{\mathrm{s,pore}}\right),$$

$$P^{\mathrm{i}} - P^{\mathrm{i}}_{\mathrm{pore}} = RT\left(C^{\mathrm{i}}_{\mathrm{n}} + C^{\mathrm{i}}_{\mathrm{s}} - C^{\mathrm{i}}_{\mathrm{s,pore}}\right).$$

Combining these equations and assuming equal pressures in the intracellular and extracellular solutions results in

$$P^{\mathrm{e}}_{\mathrm{pore}} - P^{\mathrm{i}}_{\mathrm{pore}} = -RT\left(C^{\mathrm{e}}_{\mathrm{n}} - C^{\mathrm{i}}_{\mathrm{n}} + \left(1 - K_{\mathrm{s,pore}}\right)\left(C^{\mathrm{e}}_{\mathrm{s}} - C^{\mathrm{i}}_{\mathrm{s}}\right)\right).$$

As above, we will model pressure-driven flow through the pore using the equation for laminar flow through a macroscopic cylinder. This results in a volumetric flow rate through a single pore of

$$Q = \frac{\left(P^{\mathrm{e}}_{\mathrm{pore}} - P^{\mathrm{i}}_{\mathrm{pore}}\right)\pi r^4}{8\eta\delta} = -\frac{RT\left(C^{\mathrm{e}}_{\mathrm{n}} - C^{\mathrm{i}}_{\mathrm{n}} + \left(1 - K_{\mathrm{s,pore}}\right)\left(C^{\mathrm{e}}_{\mathrm{s}} - C^{\mathrm{i}}_{\mathrm{s}}\right)\right)\pi r^4}{8\eta\delta},$$

and a total volumetric flow rate per cell of

$$\frac{d(W + \bar{v}_{\mathrm{s}}S)}{dt} = nQ = -\frac{RTn\pi r^4}{8\eta\delta}\left(C^{\mathrm{e}}_{\mathrm{n}} - C^{i}_{n} + \left(1 - K_{\mathrm{s,pore}}\right)\left(C^{\mathrm{e}}_{\mathrm{s}} - C^{\mathrm{i}}_{\mathrm{s}}\right)\right).$$

Comparison of this equation and the original KK model shows that the interaction parameter is equal to

$$\sigma = 1 - K_{\mathrm{s,pore}},$$

and the hydraulic conductivity is equal to

$$L_{\mathrm{p}} = \frac{n\pi r^4}{8\eta\delta A}.$$

The interaction parameter is often referred to as the reflection coefficient because it represents the extent to which the solute can enter the pore (a reflection coefficient of 1 means all solute is "reflected" at the pore entrance and no solute enters the pore).

In addition to the pressure gradient within the pore, there is also a gradient in the concentration of permeating solute. This concentration gradient drives diffusion of solute through the pore. The overall flux of solute includes the diffusive flux as well as the flux due to bulk convective flow through the pore, resulting in a total molar flow rate per cell of

$$\frac{dS}{dt} = n\pi \mathrm{r}^2 D_{\mathrm{s,pore}} \frac{\left(C^{\mathrm{e}}_{\mathrm{s,pore}} - C^{\mathrm{i}}_{\mathrm{s,pore}}\right)}{\delta} + C^{*}_{\mathrm{s}} \frac{d(W + \bar{v}_{\mathrm{s}} S)}{dt},$$

where $D_{\mathrm{s,pore}}$ is the diffusivity of solute within the pore and $C^{*}_{\mathrm{s}} = 0.5\left(C^{\mathrm{e}}_{\mathrm{s,pore}} + C^{\mathrm{i}}_{\mathrm{s,pore}}\right)$ is the average solute concentration in the pore. Substituting this equation and the definition of $K_{s,pore}$ into the above differential equation yields

$$\frac{dS}{dt} = \frac{n\pi \mathrm{r}^2 D_{\mathrm{s,pore}} K_{\mathrm{s,pore}}}{\delta}\left(C^{\mathrm{e}}_{\mathrm{s}} - C^{\mathrm{i}}_{\mathrm{s}}\right) + (1-\sigma)\left(\frac{C^{\mathrm{e}}_{\mathrm{s}} + C^{\mathrm{i}}_{\mathrm{s}}}{2}\right)\frac{d(W + \bar{v}_{\mathrm{s}} S)}{dt}.$$

Comparison of this equation and the original KK model shows that the solute permeability is equal to

$$P_{\mathrm{s}} = \frac{n\pi r^2}{A}\frac{D_{\mathrm{s,pore}} K_{\mathrm{s,pore}}}{\delta}.$$

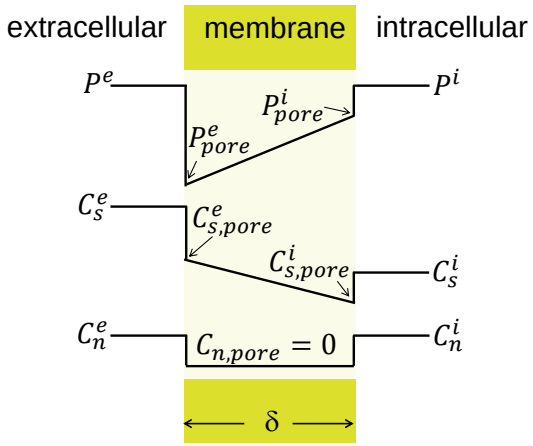

Figure 2.4. Water and solute transport through a co-transporting membrane channel*. The channel entirely excludes nonpermeating solute and partially excludes permeating solute, resulting in a net decrease in the total solute concentration within the pore. When the permeating solute concentration is higher in the extracellular solution than it is inside the cell, this leads to a pressure gradient driving convective flow out of the cell, as well as a concentration gradient driving solute diffusion into the cell.*

2.4. Water Transport in RBCs

The mechanism of water transport in human RBCs has been studied and debated for more than 50 years. We now know that water predominantly crosses the RBC membrane through pores formed by aquaporin-1 (AQP1), although the existence of aqueous pores in the RBC membrane was postulated well before the discovery of the aquaporin family of membrane proteins. In this section, we review the historical evidence for existence of membrane pores, as well as the more recent evidence that water is transported via AQP1.

2.4.1. Kinetics of water transport

When human RBCs are exposed to hypo- or hypertonic solution, they reach a new equilibrium cell volume much more rapidly than most other cell types. This is because the RBC membrane is particularly permeable to water. For example, the water permeability of human RBCs is about 10-fold higher than that of granulocytes, platelets, lymphocytes and oocytes [55]. The water permeability of RBCs is also generally higher than that of lipid membranes, ranging from about 2-fold to 100-fold higher depending on the composition of the lipid membrane [56, 57]. These data suggest the presence of a non-lipid component of the RBC membrane that enhances water transport.

2.4.2. Activation energy for water transport

The water permeability of human RBCs is only weakly dependent on temperature, yielding an activation energy for water transport of 14–20 kJ/mol [44, 58-61]. This activation energy is lower than that of many other cells types [55]. It is also lower than the activation energy for lipid membranes, which ranges between about 35 kJ/mol and 120 kJ/mol [56]. The activation energy for water transport in human RBCs is comparable to the activation energy for the self-diffusion of water [62], suggesting an aqueous pathway for the transport of water through the RBC membrane [63, 64].

2.4.3. Comparison of osmotic and diffusional water permeability

The water permeability of human RBCs has been determined in two different types of experiments. The first involves exposure to hypo- or hypertonic conditions and measuring the resulting change in cell volume caused by bulk flow of water across the

membrane. The water permeability determined from these experiments is known as the osmotic water permeability. In the second type of experiment, the exchange of radioactively labeled water is measured in the absence of an osmotic driving force. These experiments yield the diffusional water permeability. Comparison of the osmotic and diffusional permeabilities provides information about the mechanism of water transport. In the case of bilayer diffusion, the osmotic and diffusional permeabilities are expected to be identical because in both cases water (or labeled water) diffuses through the bilayer down its concentration gradient (see Figure 2.1). This expectation has been substantiated in experiments with lipid membranes, in which the osmotic and diffusional permeability have been shown to be approximately equal [56, 65]. However, for aqueous pores the mechanism and driving force for water transport are very different in the two types of experiments. If there is an osmotic driving force across the pore, then a pressure gradient develops and drives bulk flow of water through the pore (see Figure 2.2). However, in the absence of an osmotic driving force, no pressure gradient develops and movement of water through the pore occurs by random diffusional motion. Pressure driven flow through the pore is expected to be faster than diffusion and consequently the osmotic permeability is expected to be higher than the diffusional permeability. This is indeed the case for human RBCs. At room temperature, the diffusional permeability is approximately $3x10^{-3}$ cm/s [57, 60, 66-68] and the osmotic permeability is about 6 times higher [57, 58, 69, 70].

2.4.4. Effects of inhibitors

The osmotic water permeability is dramatically reduced by the mercurial compounds PCMB (*p*-chloromercuribenzoate) and PCMBS (*p*-chloromercuribenzene sulfonate), and the inhibitory effect of these compounds can be completely reversed by adding excess cysteine [71]. This provides evidence for involvement of a protein in the water transport process. To characterize the specificity of the water transporter, Macey and Farmer (1970) compared the effects of inhibitors on water and solute permeabilities [71]. PCMBS was found to have a similar effect on transport of water, urea and methylurea, but a negligible effect on many other small polar nonelectrolytes. However, treatment with phloretin substantially reduced the membrane permeability to urea and methylurea without affecting the water permeability. Together, these results suggest the presence of water-specific pores in the RBC membrane that are blocked by treatment with PCMB and PCMBS, but not by treatment with phloretin. After maximal inhibition with mercurial compounds the residual water permeability is consistent with diffusion across the bilayer. The resulting permeability value is about 10-fold lower than the control value and similar to that obtained for bilayer membranes [56, 61]. In addition, the activation energy for water transport increases after PCMBS inhibition to a value consistent with the activation energy for bilayer membranes, and the osmotic and diffusional permeabilities become approximately equal [61]. The inhibition studies were used to quantitatively analyze the contributions of channel transport and bilayer transport to the water permeability under control conditions, yielding an osmotic water permeability comprising about 90% channel transport and 10% bilayer transport, and

diffusional water permeability comprising about 50% channel transport and 50% bilayer transport [57].

2.4.5. Identification of the water transporting protein

In the late 1980s, the protein that is predominantly responsible for transmembrane water transport in human RBCs was discovered [72], and in the early 1990s a role for this protein as a water channel was suggested [73] and subsequently demonstrated using experiments with Xenopus oocytes [74]. The water channel protein was originally called CHIP28, but it is now known as aquaporin-1 (AQP1). It is expressed at high levels in human RBCs, having a copy number of approximately 200,000 molecules per cell [47]. AQP1-mediated water transport is inhibited by mercuric chloride, consistent with previous studies of inhibition of water transport in RBCs [74]. Experiments on Colton null RBCs, which lack AQP1, are also consistent with previous inhibition studies. The osmotic water permeability of Colton null RBCs is about 10-fold lower than that of normal RBCs, suggesting that about 90% of water is transported via AQP1 in normal RBCs [44]. This is consistent with the approximately 10-fold reduction in water permeability caused by treatment of normal human RBCs with mercurial compounds [57]. In addition, the activation energy for water transport is about 2-fold higher in Colton null RBCs [44], which is consistent with the approximately 2-fold increase in activation energy after treatment of normal RBCs with mercurial compounds [57].

Whereas AQP1 is responsible for the majority of water transport in RBCs, there is evidence that an additional membrane protein, UT-B, may also contribute to water transport [75]. UT-B is expressed in human RBCs at a copy number of about 14,000

molecules per cell [47] and has been shown to be permeable to water with a single channel permeability similar to that of AQP1 [75]. In experiments with knockout mice, Yang and Verkman concluded that AQP1 was responsible for about 90% of water transport, UT-B was responsible for 8% and the remaining 2% was presumably due to diffusion across the bilayer [75]. In humans, aquaporin-3 (AQP3) may also contribute to water transport. AQP3 has been estimated to have a copy number of about 15,000 in human RBCs [46], and a single channel water permeability about 30% that of AQP1 [45]. Although the extent to which UT-B and AQP3 contribute to water transport in human RBCs is uncertain, the combined effects of these membrane proteins is not expected to exceed about 10% of the overall water transport, as about 90% of water transport can be attributed to AQP1 [44].

2.4.6. Summary of water permeability values reported in the literature

Figure 2.5 summarizes the osmotic water permeability values at room temperature that have been reported in the literature. The data are presented in terms of the water permeability parameter $P_{\mathrm{w}}A/W_0$, where W_0 represents the cell water volume under isotonic conditions. This parameter is inversely related to the time scale of osmotic water transport. Because of the speed with which water crosses the RBC membrane, it has been particularly challenging to obtain accurate water permeability measurements. It is in part because of experimental difficulties that there is so much spread in the reported permeability values. In particular, the permeability reported by Saari and Beck appears to be a clear outlier, with a value much lower than the general trend [76]. This is

probably because Saari and Beck used a modified time to lysis method, whereas the other studies used more accurate methods.

The dependence of water permeability on the solution osmolality has been considered in two different contexts. The first involves experiments in which RBCs are exposed to hypo- or hypertonic solutions containing nonpermeating solutes (e.g., salts) but lacking permeating solutes (e.g., ethylene glycol). In 1968, Rich et al. reported a water permeability that decreased as the solution osmolality increased [77] and two years later Farmer and Macey instead suggested that the water permeability was dependent on the direction of water flow [78]. In 1980, Levin et al. again reported that the water permeability decreased as the solution osmolality increased [79]. However, more recent studies indicate that the water permeability is independent of the solution osmolality and the direction of water flow, and that previous observations of concentration- and directional-dependence of water permeability were most likely caused be experimental artifacts [69, 70].

However, in experiments involving exposure to permeating solutes such as ethylene glycol, a strong concentration-dependence of the water permeability has been observed [58, 80]. The grey-filled symbols in Figure 2.5 show that ethylene glycol has an inhibitory effect on water transport. This inhibitory effect may be caused by binding of ethylene glycol at the entrance or exit to the water channel, resulting in steric hindrance to water flow [80]. Water permeability measurements obtained in the presence of glycerol are shown with the black-filled circles. The effect of glycerol on water transport is less clear, but it appears that glycerol may also have an inhibitory effect [58].

Cryopreserved RBCs are exposed to solution concentrations ranging from isotonic conditions (~0.3 osmol/kg) to about 7 osmol/kg. As shown in Figure 2.5, this corresponds to water permeability values that vary by more than an order of magnitude. To account for this concentration dependence, we fit the data in Figure 2.5 using the following phenomenological model:

$$\frac{P_{\mathrm{w}}A}{W_0} = \frac{a_{\mathrm{w}}}{b_{\mathrm{w}}M + 1},$$

where M is the average solution osmolality and a_{w} and b_{w} are fit parameters. The form of this model is similar to that presented in Section 2.3.1.3 for carrier-mediated transport, and is consistent with the inhibition of water transport by solute binding at the pore edge, as proposed by Toon and Solomon [80]. A fit of this model to the data presented in Figure 2.5 (excluding the data point from Saari and Beck [76]), resulted in best-fit parameters $a_{\mathrm{w}} = 1020\ \mathrm{s}^{-1}$ and $b_{\mathrm{w}} = 2.83$ kg/osmol.

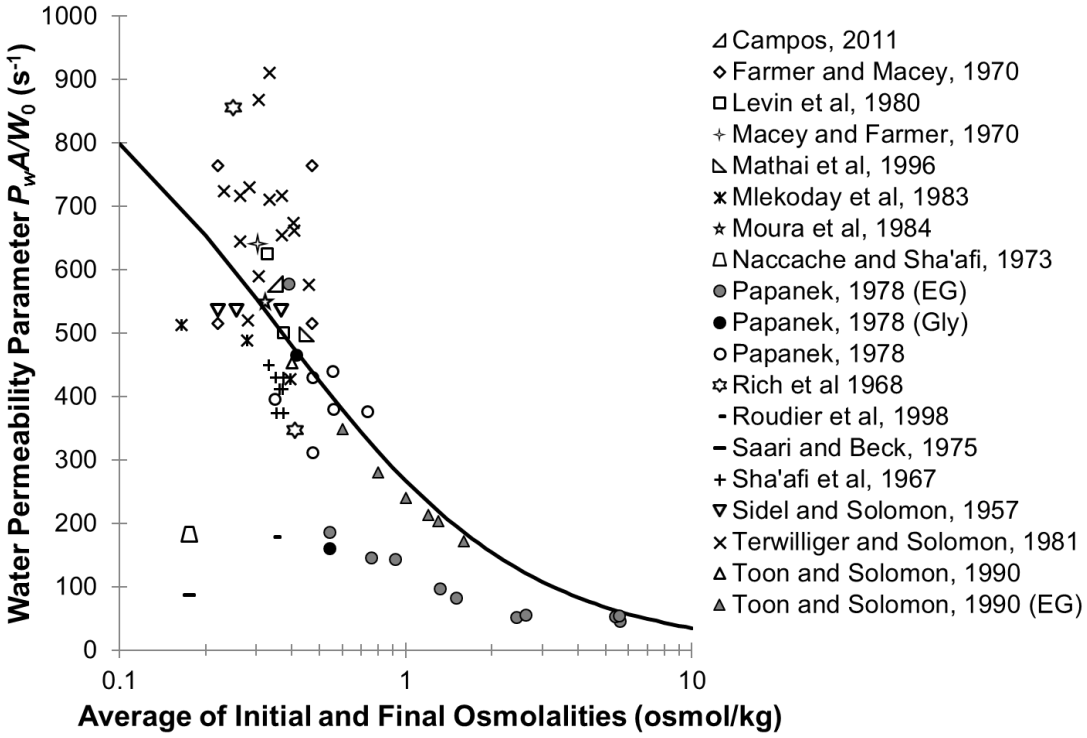

Figure 2.5. Effect of solution osmolality on the osmotic water permeability of human RBCs at room temperature, 20°C–26°C *[44, 46, 57-59, 69-71, 76-83]. Grey-filled symbols show water permeability values in the presence of ethylene glycol (EG) and black-filled symbols show water permeability values in the presence of glycerol. All other symbols represent water permeability measurements obtained after exposure to solutions containing only nonpermeating solutes (e.g., salts). The line shows the best-fit concentration-dependent permeability model (see text for details). In two cases, the water permeability was reported as a best-fit parameter using the KK model [58, 80]. In these cases, the corresponding permeability for the 2P model was estimated as described previously [84]. Briefly, the published KK parameters were used to predict the cell volume response after exposure to 1 M CPA, and the resulting predictions were used to obtain best-fit permeability values using the 2P model.*

2.5. Glycerol Transport in RBCs

While the presence of a facilitated pathway for glycerol transport in human RBCs has been suspected for over 50 years [85], it wasn't until 1998 that the glycerol transporter was identified as AQP3 [46]. In this section we review the early literature on the kinetics and mechanism of glycerol transport in human RBCs, as well as more recent literature focused on the role of AQP3 in glycerol transport.

2.5.1. Kinetics of glycerol transport

The kinetics of glycerol transport has been found to vary widely in different mammals, from relatively fast glycerol transport in the rat to 100-fold slower transport kinetics in the ox [86]. These differences in permeability have been postulated to be caused by differences in membrane lipid composition [87], or by the presence of glycerol transporter proteins in some mammals but not in others [85]. In comparison to most other mammals, glycerol transport is relatively fast in human RBCs [86].

2.5.2. Activation energy for glycerol transport

The temperature dependence of the glycerol permeability in human RBCs has not been as thoroughly studied as the temperature dependence of the water permeability. Reported values of the activation energy for glycerol transport range from 15 kJ/mol to 40 kJ/mol [38, 48, 59, 88]. In comparison, the activation energy for glycerol transport through lipid bilayers is substantially higher, ranging from about 50 kJ/mol to 80 kJ/mol [89, 90]. This suggests the presence of a hydrophilic pathway through the bilayer that reduces the energetic barrier to glycerol transport in human RBCs.

2.5.3. Effects of inhibitors

Glycerol transport in human RBCs is significantly reduced by copper ions at concentrations as low as 10^{-7} molar [38, 85, 91-93]. Exposure to copper also affects the activation energy for glycerol transport, increasing it to 80–100 kJ/mol [38, 93], a value comparable to that observed for bilayer membranes [89]. Mercury ions and the mercurial compound PCMB have also been found to inhibit glycerol transport in human RBCs [85]. The inhibitory effects of copper, mercury and PCMB can be reversed by addition of sulfhydryl compounds such as cysteine [85].

Hydrogen ions also inhibit glycerol transport [38, 93, 94]. Under acidic conditions, the glycerol permeability is more than an order of magnitude lower than the permeability at neutral pH, and comparable to the residual permeability after maximal inhibition with copper ions [38]. The glycerol permeability is approximately independent of pH above pH 7. Under acidic conditions, the activation energy for glycerol transport is 80–120 kJ/mol, comparable to the activation energy in the presence of copper ions [38]. These data suggest that copper and hydrogen ions inhibit a glycerol transporter protein and that under conditions of maximal inhibition, residual glycerol transport is due to bilayer diffusion.

Certain small nonelectrolytes have also been found to inhibit glycerol transport, including ethylene glycol, isopropanol, 1,2 propanediol, 1,3 propanediol and dimethylsulfoxide [38, 92, 94]. Because of the similarity of these molecules to glycerol, the inhibitory effect has been interpreted as competition for a binding site on a glycerol transporter protein [38, 92, 94]. Experimental data is consistent with such an

interpretation in that the inhibitory effect of these molecules is diminished as the glycerol concentration increases [38].

2.5.4. Identification of the glycerol transporting protein

In 1998, Roudier and colleagues demonstrated that human RBCs express AQP3 [46], an aquaporin known to be permeable to glycerol [45, 95]. They also showed that Colton null RBCs (which lack AQP1) express AQP3 and have a glycerol permeability similar to that of normal RBCs, strongly suggesting that AQP3 is main glycerol transporter in human RBCs [46]. AQP3 is a member of a group of aquaporins that are permeable to both water and glycerol known as aquaglyceroporins. In general, the properties of AQP3 are consistent with the glycerol permeability properties of human RBCs. The activation energy for glycerol transport via AQP3 is about 25 kJ/mol [96, 97], which is consistent with the activation energy for glycerol transport in human RBCs. AQP3-mediated glycerol transport has been shown to be inhibited by acidic pH [97] and copper ions [98], as is glycerol transport in human RBCs. Although human RBCs exhibit saturable glycerol transport kinetics [38, 92, 94, 99], the effects of glycerol concentration on AQP3-mediated transport have not yet been completely resolved. Echevarria and colleagues did not observe evidence of saturation up to a glycerol concentration of 0.165 molar [95]. However, glycerol transport has been found to be saturable in the aquaglyceroporins AQP9 and AQP10 [100, 101]. It is quite possible that saturation would also be observed for AQP3 at glycerol concentrations higher than those used by Echevarria et al. [95]. Further evidence that AQP3 is the main glycerol transporter in human RBCs has been obtained by studying RBCs from individuals lacking AQP3. The

glycerol permeability of AQP3-null RBCs is nearly two orders of magnitude lower than that of normal RBCs, and nearly identical to the permeability of copper-treated RBCs [48]. In addition, AQP3-null RBCs exhibit a higher activation energy for glycerol transport than control cells, which is consistent with glycerol transport through the bilayer [48]. Together, these previous studies provide strong evidence that AQP3 is the primary route of glycerol transport in human RBCs.

Although its name suggests that it operates as a membrane pore, AQP3 appears to exhibit more complex behavior than would be expected for a physical pore. For example, the water and glycerol permeabilities are both affected by pH, but over a different pH range, with the water permeability being more substantially reduced at pH 6 than the glycerol permeability [97]. This type of behavior would not be expected for a physical pore with a selectivity based entirely on molecular size. The mechanism of AQP3-mediated water and glycerol transport has been postulated to involve formation of successive hydrogen bonds with AQP3 [97].

2.5.5. Summary of glycerol permeability values reported in the literature

Published glycerol permeability values for human RBCs at room temperature vary widely, as shown in Figure 2.6. In particular the permeability value reported by Toon and Solomon is substantially larger than other reported values; the reason for this discrepancy is unclear [80]. In addition, the permeability values reported by Jay and Rowlands [102] and Saari and Beck [76] are both lower than the general trend. Both of these studies used a modified time to lysis method for determination of the permeability values, which is known to be prone to error. After excluding the data point from Toon

and Solomon, the trend is reasonably consistent showing a decreasing permeability as the average solution osmolality increases. Such a decreasing trend is consistent with carrier mediated transport (see section 2.3.1.3 and Figure 2.3). It is also consistent with a pore or channel in which transport is dependent on the formation of successive hydrogen bonds, where the hydrogen bonding sites become saturated as the glycerol concentration increases [97]. To quantify the concentration-dependence of the glycerol permeability, we fit the data in Figure 2.6 to the phenomenological model described above (section 2.4.6), resulting in best-fit parameters $a_s = 0.173\ s^{-1}$, and $b_s = 1.03$ kg/osmol.

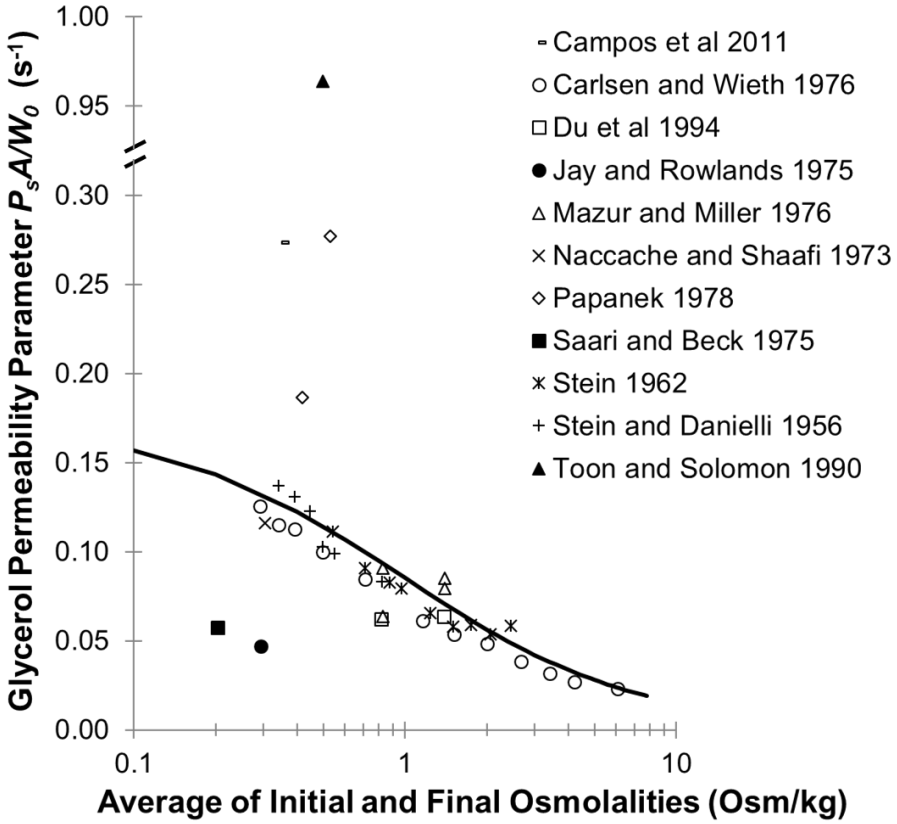

Figure 2.6. Effect of solution osmolality on the glycerol permeability of human RBCs at room temperature, 20°C–25°C *[38, 58, 59, 76, 80, 83, 88, 92, 94, 102, 103]. The line shows the best-fit concentration-dependent permeability model (see text for details). The data point from Toon and Solomon was omitted from the fit [80]. In two cases, the glycerol permeability was reported as a best-fit parameter using the KK model [58, 80]. In these cases, the corresponding permeability for the 2P model was estimated as described previously [84]. Briefly, the published KK parameters were used to predict the cell volume response after exposure to 1 M CPA, and the resulting predictions were used to obtain best-fit permeability values using the 2P model.*

2.6. Interaction Between Water and Glycerol Transport

The most commonly used method for identifying interaction between water and solute transport is based on examination of the reflection coefficient σ (see section 2.3.2). In the case of non-interacting water and solute fluxes, the reflection coefficient is expected to be $\sigma = 1 - P_s \bar{v}_s / RTL_p$, and when the fluxes do interact the reflection coefficient is expected to be lower than this value [49]. The reflection coefficient for glycerol transport in human RBCs has been reported to be between 0.52 and 0.88 [58, 104, 105], whereas the non-interacting value is expected to be nearly 1. However, the accuracy of solute reflection coefficients reported for human RBCs has been called into question because of the potential for experimental artifacts which cause the value of σ to be underestimated [106, 107]. The estimates for σ obtained from experiments on human RBCs represent the aggregate effects of multiple pathways for water and glycerol transport. About 90% of water transport is mediated by AQP1, and AQP1 is not permeable to glycerol [45]. Nonetheless, Zeuthen and Klaerke reported a glycerol reflection coefficient of σ = 0.94 for AQP1 [97]. The large majority of glycerol transport is mediated by AQP3, which is also permeable to water [45]. The glycerol reflection coefficient for AQP3 has been reported to be about σ = 0.15 [97]. When the RBC membrane is considered as a whole, it is clear that the majority of water and glycerol fluxes would not be expected to interact because water and glycerol predominately cross the membrane using different pathways.

2.7. Relative Rates of Water and Glycerol Transport

It is often useful to consider the dimensionless versions of models. The process of nondimensionalizing, for example, often brings out useful "lumped" parameters that take on special significance with respect to overall model behavior. Classical examples are the Reynold's or Peclet numbers in fluid dynamics. Exploration of nondimensional forms of the 2-parameter model was introduced by Katkov [108], and used by Benson et al. [109], Davidson et al. [110], and others in the context of cryobiology. In particular, Benson [111] defines the parameters

$$b = \frac{P_{\mathrm{s}}}{L_{\mathrm{p}} R\ T\ M_{\mathrm{iso}}},$$

$$\tau = \frac{L_{\mathrm{p}} R\ T\ M_{\mathrm{iso}} A}{W_0},$$

where M_{iso} is the isotonic osmolality. Note that these are arbitrary choices of reparametrizing parameters, but they are natural for the systems dealt with in cryobiology.

As discussed in Benson [111], we observe that *b* is independent of cell size and surface area, and as such it is a function of membrane transport alone, and that two different cells with similar *b* values will have similar volume extrema due to anisosmotic solution exposure. They will be different only in the amount of time their process will take, which is a function of τ.

Therefore, in the context of the discussion of concentration dependent transport, we are interested in the concentration dependence of the ratio of solute to water permeability. We begin with *b* as defined above, with the hydraulic conductivity replaced as defined in equation 1:

$$b = \frac{P_s}{\frac{P_w \bar{v}_w}{RT}\, RT m_{iso}} = \frac{P_s}{P_w \bar{v}_w m_{iso}}.$$

We can rewrite this equation in terms of the permeability parameters in Figures 2.5 and 2.6, which allows insertion of the concentration dependent models defined in sections 2.4.6 and 2.5.5:

$$b = \frac{P_s A/W_0}{\bar{v}_w m_{iso} P_w A/W_0} = \frac{\frac{a_s}{1+b_s M}}{\bar{v}_w\, m_{iso}\, \frac{a_w}{1+b_w M}} = \frac{1}{\bar{v}_w\, m_{iso}} \frac{a_s + a_s b_w M}{a_w + a_w b_s M}.$$

Then the minimal value of b when the average osmolality $M = 0$ is

$$b = \frac{a_s}{\bar{v}_w\, m_{iso}\, a_w},$$

and the limiting value as M increases is

$$b = \frac{a_s b_w}{\bar{v}_w\, m_{iso}\, a_w b_s}.$$

Next, we consider the time-scale parameter τ. Here we observe that using the concentration dependent model defined in section 2.4.6, we get

$$\tau = \frac{L_p ART m_{iso}}{W_0} = \frac{P_w A\, \bar{v}_w\, m_{iso}}{W_0} = \bar{v}_w\, m_{iso} \frac{a_w}{1+b_w M},$$

The concentration dependence of these parameters can be seen in Figure 2.7.

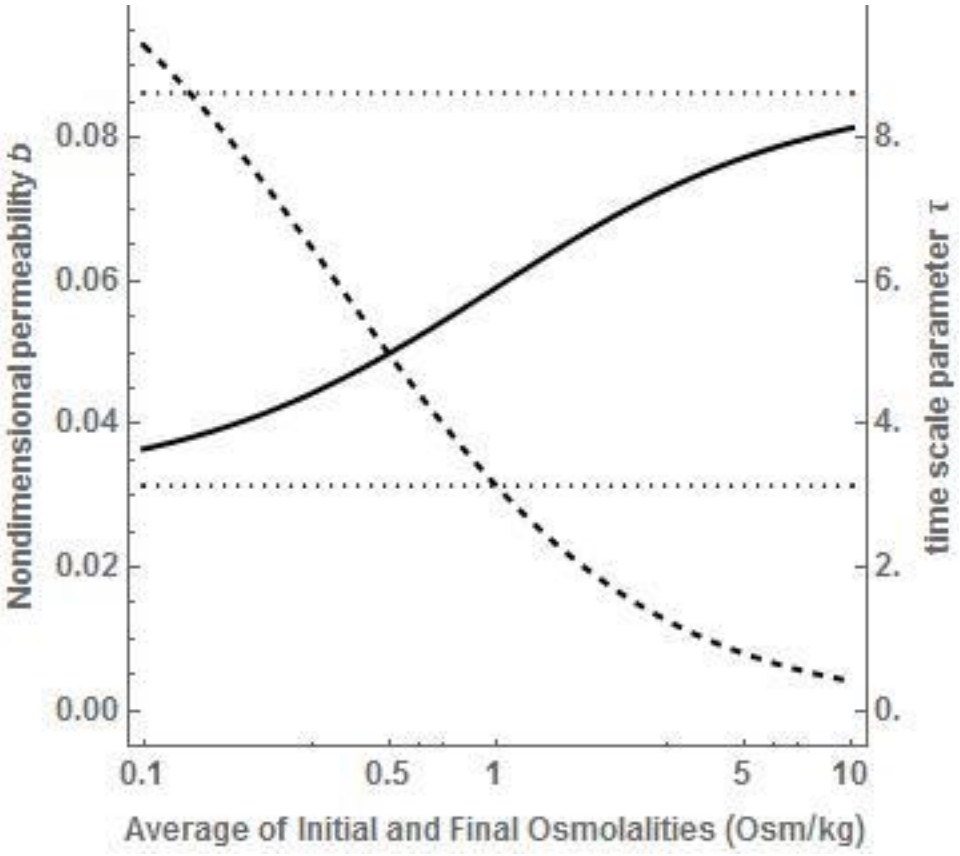

Figure 2.7. Plot of the nondimensional permeability parameter b (solid line), its limiting values (dotted lines), and the time scale parameter τ (dashed line) as a function of osmolality. *Predictions are shown for* $M_{iso} = 0.3$ *mol/L and* $\bar{v}_w = 0.018$ *L/mol, which results in a dimensionless product* $\bar{v}_w\, m_{iso} = 0.0054$.

Note that the values of the nondimensional permeability parameter are constrained between b = 0.031 and b = 0.086, a range where the maximum is 2.7 times the minimum value. Therefore, though the water and solute permeability values change dramatically over the range of concentrations, their ratios, and thus the magnitude of volume response, remain much more consistent. On the other hand, the time scale factor τ is also critical

when designing protocols, and this scale is dependent explicitly on the water permeability without the solute permeability.

Compared with many other cell types, human RBCs have a relatively low *b* value, which indicates that glycerol transport is much slower than water transport. It is instructive to compare the *b* values for RBCs with those of, say human oocytes where b=1.62 for ethylene glycol at 22 °C [110, 112]. Here given the same chemical potential gradients, solute transport will be 40 times faster relative to water transport in oocytes than in RBCs. This is not to say that the oocyte will react to anisosmotic media on a faster time-scale. For oocytes, the time-scale parameter $\tau = 0.004$ s^{-1}, compared with the range of about 4 s^{-1} to 0.2 s^{-1} for RBCs. This indicates that RBCs are expected to respond to anisosmotic exposure between 50 and 1000 times faster than oocytes. Note that for human oocytes the concentration dependence of water and solute permeability (or of their unitless counterparts) has not been explored in the literature.

For low *b*, the classic swell–shrink volume response to CPA removal protocols has a "sharper" and higher maximum than the response for high *b* value, where the volume increases more gradually to its maximum. Therefore, the higher *b* value at high concentrations appears to make designing deglycerolization simpler, causing RBCs to be relatively less responsive to a stepwise reduction in extracellular glycerol.

2.8. Discussion and Conclusion

We have compiled the most relevant research on modeling considerations for human erythrocyte water and glycerol transport. It is apparent after evaluating the available data and mathematical models that neither the KK model nor the 2P model

accurately describes the transport phenomena in RBCs. As can be seen in Table 1, the transport mechanisms for water and glycerol are complex and involve multiple pathways. Most of the water transport occurs via AQP1 while almost all the glycerol transport occurs via AQP3. Under these conditions there would be very little overall water–solute interaction except the small amount that occurs in AQP3. Therefore, the KK model does not provide a physically reasonable description of water and glycerol transport in human RBCs. The 2P model is also physically inconsistent with the transport mechanisms. The 2P model assumes no solute–water interaction; from experimental evidence, this is not completely true. AQP3 is known to be permeable to both water and glycerol so there will be water–glycerol interaction within this pore.

Table 2.1: Pathways for human erythrocyte glycerol and water transport and their relative contributions at room temperature

	Bilayer	**AQP1**	**AQP3**	**UT-B**
Water	5 to 8%	84 to 87% [b]	2% [c]	6% [d]
Glycerol [a]	1 to 2%	0%	98 to 99%	0%
# per cell	--	200,000	15,000	14,000

[a] *Glycerol transport values estimated from rate of glycerol uptake reported in normal vs. AQP3 deficient cells [48].*

[b] *Water transport through AQP1 based on comparison between Colton Null RBCs and normal RBCs [44, 46].*

[c] *Water transport through AQP3 estimated based on published single pore permeability values for AQP1 and AQP3 (P_{AQP1} and P_{AQP3}, respectively [45]) and the reported number of AQP1 and AQP3 pores per human RBC (N_{AQP1} and N_{AQP3}, respectively [46, 47]), by solving the following system of equations:*

$$\frac{N_{\mathrm{AQP1}} P_{\mathrm{AQP1}}}{\text{total permeability}} = \text{fraction transported via AQP1},$$

$$\frac{N_{\mathrm{AQP3}} P_{\mathrm{AQP3}}}{\text{total permeability}} = \text{fraction transported via AQP3}.$$

[d] *Water transport through UT-B was estimated as described above, using the published single pore permeability [75] and the number of pores per cell [47] for UT-B.*

To truly represent the physics of water–glycerol transport in human RBCs a more complete physical model would be needed. Such a model would require additional parameters to account for each pathway that water and glycerol can take across the cell membrane. Table 1 serves to outline what parameters would need to be individually determined for each transported species and pathway. A water permeability would be needed for each of the four pathways for water transport, a glycerol permeability would be needed for the bilayer and AQP3, a reflection coefficient would be needed for AQP3, and activation energies would be needed for each water and solute pathway. These 13 parameters would be difficult to determine experimentally, and even if parameter values were available, the resulting model would still be based on the questionable assumption that AQP1 and AQP3 obey the pore models described in sections 2.3.1.2 and 2.3.2.1.

It is evident in the compiled data in Figures 2.5 and 2.6 that both water and glycerol permeabilities are dependent on the solute concentration. Such a concentration

dependence is not predicted by traditional pore models (see sections 2.3.1.2 and 2.3.2.1). In the case of glycerol transport through AQP3, saturation of a binding site in the channel is a very likely explanation for the observed concentration dependence. The concentration dependence of water transport is possibly explained by partial occlusion of the channels by other solutes. This could be caused by glycerol or other solutes partially entering the channel [113, 114]. A more complete understanding of the processes involved in this concentration dependence may need to be investigated before a more advanced physical model can be realized.

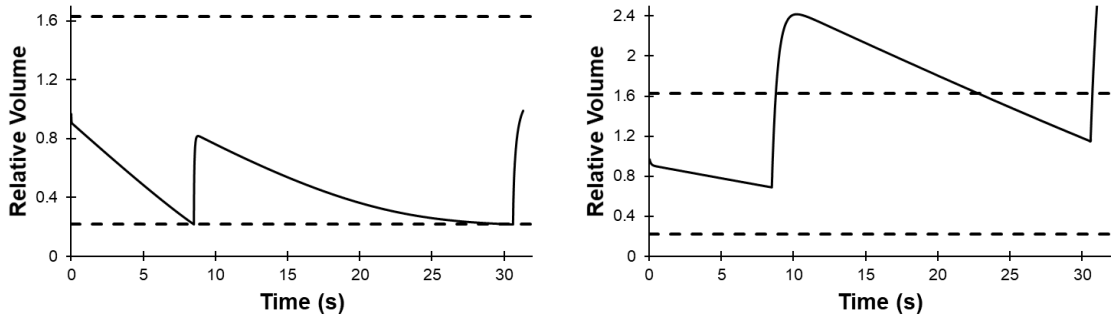

Figure 2.8. Predictions of osmotically active cell volume during deglycerolization using either constant water and glycerol permeability parameters (A) or the concentration-dependent permeability models presented in sections 2.4.6 and 2.5.5 above (B)*. In both cases, a three-step deglycerolization process was used, with exposure times and solution compositions as defined in [19]. The constant permeability parameters used for the predictions in panel A were* $P_wA/W_0 = 440\ s^{-1}$ *and* $P_sA/W_0 = 0.065\ s^{-1}$.

Despite the fact that neither the KK model nor the 2P model accurately portrays the physics of human RBC water–glycerol transport, they are both capable of fitting experimental data under most conditions; however, the KK model requires an additional

"fudge factor" of the reflection coefficient [49]. Given that both models would need to be treated as phenomenological models for human RBCs, we recommend use of the simpler 2P model. A limitation of the traditional 2P model is that it does not account for the concentration dependence of permeability. The synthesis of literature values for water and glycerol permeability shown in Figures 2.5 and 2.6 clearly show that both change significantly over the range of concentrations encountered during RBC cryopreservation. Figure 2.8 illustrates the importance of accounting for the concentration dependence of permeability when designing rapid deglycerolization procedures. In our previous study we used constant permeability parameters to mathematically optimize exposure times and solution compositions for a three-step deglycerolization procedure [19]. Although the resulting procedure was not predicted to cause excessive cell volume changes (Figure 2.8A), it resulted in significant hemolysis. In contrast, when the concentration dependent permeability models presented here (see sections 2.4.6 and 2.5.5) were used with the same timing and solute concentrations in each step, the cell volume was predicted to expand far past the upper osmotic tolerance limit (Figure 2.8B). This could be part of the reason hemolysis values were higher than expected [19]. The addition of these concentration dependent parameters to the existing transport models may enable development of more robust procedures for rapid deglycerolization of human erythrocytes. We plan to further explore these procedures in future work.

The concentration dependence of permeability values for RBCs shown in Figures 2.5 and 2.6 also has much broader implications. Many other cell types are known to express aquaporins and aquaglyceroporins [115-117], and it is reasonable to expect a similar concentration dependence of permeability values for other cell types as well. In

addition to glycerol, aquaglyceroporins have been shown to transport other commonly used CPAs, including ethylene glycol and dimethyl sulfoxide [118]. Thus, it is likely that the concentration dependence of the cell membrane permeability to water and CPA has broad relevance for design of cell cryopreservation procedures, especially when high CPA concentrations are used, such as for vitrification. The potential importance of the concentration dependence of CPA permeability has received little attention in the literature, and it is common to assume constant permeability values to make predictions over the broad range of CPA concentrations encountered during cell vitrification [109, 110, 112, 119-121]. These predictions could have significant errors. The changes in permeability shown in Figures 2.5 and 2.6 are large: more than an order of magnitude for water and more than a factor of 5 for glycerol. Such large changes in permeability would dramatically change the time scale of membrane transport, as well as the magnitude of predicted cell volume changes. The results presented here highlight the need for future studies to better characterize the concentration dependence of cell membrane permeability parameters.

2.9 Acknowledgments

This work was supported by a National Science Foundation grant (#1150861) to Adam Higgins, and the National Science and Engineering Research Council (RGPIN-2017-06346 to JB), and the National Institute of Child Health and Human Development (5R01HD083930-02 to JB).

Chapter 3: Implications of Variability in Cell Membrane Permeability for Design of Methods to Remove Glycerol from Frozen-thawed Erythrocytes

John M. Lahmann, Cynthia Cruz-Sanchez, James D. Benson,

Jason P. Acker, Adam Z. Higgins

3.1 Abstract

Blood is currently prepared for freezing in a solution of 40% glycerol. While glycerol is not inherently toxic to humans, it must be removed prior to transfusion to prevent osmotic hemolysis. The current deglycerolization procedure requires about 45 minutes per unit of blood. We previously presented predictions suggesting that glycerol can be safely removed from erythrocytes in less than one minute. However, experimental evaluation of these methods resulted in much higher hemolysis than expected. Here we extend our previous study by considering both concentration-dependence of permeability and variability in permeability values in the mathematical optimization algorithm. To establish a model for the concentration dependence of glycerol permeability, we combined literature data with new measurements of permeability in the presence of 40% glycerol. To account for variability we scaled the concentration-dependent model to define a permeability range for optimization. Methods designed using a range extending to 50% of the concentration dependent permeability had a duration of less than 3 min and resulted in hemolysis ranging from 34% to 83%; hemolysis values were highly dependent on the blood donor. Extending the permeability range to 5% of the concentration dependent value yielded a 30 min method that resulted in an average hemolysis of 12%. Our results suggest high variability in the glycerol permeability between donors and within a population of cells from the same donor. Such variability has broad implications for design of methods for equilibration of cells with cryoprotectants.

3.2 Introduction

Hypothermic storage and transfusion of preserved human erythrocytes was introduced around the beginning of the 20th century and since has become the de facto standard of for red blood cell (RBC) banking due to its overall simplicity and relatively low cost [5, 6]. It was not until the 1950s and 60s that the process of cryopreservation and transfusion of frozen-thawed RBCs gained widespread acceptance in transfusion medicine and became an ardently pursued topic among cryobiology researchers [13, 40, 122]. During the period of rapid progress in the field of RBC cryopreservation a significant problem arose, which was how to go about removing up to 40% glycerol from frozen-thawed cells in a timely and efficient manner [17]. This important, however time consuming and laborious final processing step, reduces the glycerol content to a low enough concentration to prevent post-transfusion lysis [17]. This is typically done by gently coaxing the glycerol out of the cells using wash steps with gradually decreasing strengths of hypertonic saline, preventing the cells from being exposed to extreme osmotic gradients which would otherwise cause injury and hemolysis due to rapid water influx [17, 123].

While progress in glycerol removal technology has slowed recently, there have been significant advancements in this field since the turn of the century. Perhaps the most significant technological development in recent years is the invention of the ACP215 cell washer [16]. This automated system uses a closed loop centrifugal washing bowl to expose the cells to a series of saline wash steps, removing the excess glycerol and concentrating the cells. Additionally, this system is approved for post-process storage of the frozen-thawed-deglycerolized blood for up to 2 weeks [18]. While this system has

enjoyed the spotlight as state of the art for over a decade, it still requires roughly 45 minutes to deglycerolize one unit of blood. When compared to the ease of hypothermic storage, the time and difficulty of post-thaw processing has relegated cryopreserved blood to primary use in storage of rare blood types and military applications [14]. Recently, there is some renewed interest in creating cryopreserved blood reserves for use in natural disasters or other adverse events [124].

More recent work has focused on streamlining this final processing step in hopes that reduction in the processing time and increasing usability would result in more widespread acceptance of cryopreserved RBCs in transfusion medicine [19, 21, 125]. New devices have been proposed that enable continuous glycerol removal, and ultra-rapid glycerol removal procedures have been proposed with the intent of reducing the deglycerolization time to less than a minute, albeit with limited success [19-21]. Although the proposed devices that use microfluidic or dialysis-based technology to deglycerolize cells are promising concepts, the inherent problem remains that the limiting step in rapid deglycerolization is the rate at which intracellular glycerol can be removed from an erythrocyte without damaging and/or lysing the cell.

Mathematical modeling has been an extremely useful tool in the cryobiology community for optimization of complex problems such as cryoprotectant addition and removal, freezing rates, and avoiding toxicity. A key parameter required for these modeling approaches is the cell membrane permeability. Erythrocytes are simple cells and are relatively easy to obtain, making them an indispensable model cell in cryobiology research [126-130]. Erythrocytes have been well studied within the context of the classic membrane transport models used in cryobiology and there are several decades of data on

transport parameters available from many sources [125]. Close examination of previously published permeability parameters has helped shed light on transport modeling anomalies including a distinct solute concentration dependence of water and glycerol transport. However, the data is sparsely populated at higher glycerol concentrations, with only one study coming close but not extending to the highest concentrations of glycerol experienced by cells that undergo cryopreservation in 40% glycerol [38, 125].

In our previous work, we used membrane transport modeling to design methods for removing glycerol from RBCs as rapidly as possible without causing osmotic damage. However, the methods resulted in hemolysis values that were much higher than expected [19]. Predictions in that study used constant values for water and glycerol permeability. In this current work, we build upon our previous research to examine the reasons for this increased hemolysis. First, we measured the glycerol permeability in 40% glycerol using a Coulter Counter, thereby extending the available data set to include the full range of concentrations encountered during RBC cryopreservation. We then combined this data with existing measurements available in the literature, updating our previously published concentration dependent glycerol permeability model [125]. Finally, we further refined our mathematical optimization approach to account for cell-to-cell variability in glycerol permeability. Our results suggest that the RBC permeability to glycerol varies widely, which has significant implications for design of RBC deglycerolization methods.

3.3 Materials and Methods

3.3.1. Determination of the cell membrane permeability to glycerol

3.3.1.1. Solution preparation

To estimate the glycerol permeability RBCs were exposed to an osmotically matched solution containing a relatively high glycerol concentration. The resulting cell swelling due to glycerol influx was measured using a Coulter counter and fit to the two-parameter transport model to determine the glycerol permeability. Experiments were done under isotonic conditions, as well as for 40% w/v glycerol (i.e., the concentration used for RBC cryopreservation). Two solutions were prepared for each of these experiments. The first solution is the initial solution with which the cells are diluted before being injected into the Coulter counter beaker. The second solution is the solution with relatively high glycerol concentration into which the cells are injected. The solutions use NaCl as the non-permeating solute and glycerol as the permeating solute, and are buffered with 12 mM Na_2HPO_4, and adjusted to pH 7.0. Solution osmolality was checked with an Advanced Instruments Model 3300 osmometer (Advanced Instruments Inc., MA, U.S.) and adjusted as necessary. Table 3.1 gives the initial and final solution compositions for both experimental conditions.

Table 3.1. Initial and final concentrations of permeating and non-permeating solutes for Coulter counter permeability measurements

	Initial composition (mOsm/kg)			Final composition (mOsm/kg)		
	Glycerol	Salts	Total	Glycerol	Salts	Total
Isotonic (fresh RBCs)	0	290	**290**	97	193	**290**
40% glycerol (frozen-thawed RBCs)	6500	450	**6950**	6650	300	**6950**

3.3.1.2. Blood collection and storage

Blood for the glycerol permeability experiments under isotonic conditions (290 mOsm/kg) was collected fresh daily from healthy volunteers via venous puncture into 3.2% equivalent sodium citrate vacuum tubes (BD Vacutainer). Immediately prior to each experiment the blood was centrifuged at 1400 g for 10 minutes, and the plasma and buffy coat removed. The packed red cells were diluted 1:5000 into isotonic buffered saline to prepare them for injection into the Coulter counter beaker.

To prepare blood for experiments in the presence of 40% glycerol, blood collected from volunteer donors was glycerolized, frozen, and thawed using a procedure similar to that used by Lusianti et al. [19]. Blood was processed on the same day within 1 hour of collection. The packed red cells were glycerolized in Glycerolyte 57 (Fenwal Inc., IL, U.S.) using a two-step addition procedure for a final glycerol composition of 40% w/v. In the first step 1.5 mL of Glycerolyte 57 was added via syringe pump over a 3-minute period to 4 mL of packed red cells. The cell solution was then allowed to equilibrate for 5 minutes. The second addition was 5 mL of Glycerolyte 57 over a 3-minute period. The glycerolized cells were stored in 1 mL aliquots and frozen in a -80 °C freezer in a

Nalgene® Cryo 1°C freezing container (Thermo Scientific, NC, U.S.). Blood was stored frozen for up to 2 months. Prior to use, blood was thawed in a 37 °C water bath for one minute. The blood was then centrifuged at 1400 g for 10 minutes and the packed red cells were diluted 1:5000 into the 40% glycerol dilution solution (see Table 3.1) and allowed to equilibrate for approximately one hour before sample injection into the Coulter counter beaker.

3.3.1.3. Equipment configuration

An experimental setup similar to that employed by Vian et al. was used to obtain real time volume excursions of the erythrocytes after exposure to different glycerol concentrations [131]. At the core of this configuration is a Beckman Coulter Multisizer 3 Coulter counter (Beckman Coulter, IN, U.S.) providing real time measurement of the erythrocyte volume. The Coulter counter was fitted with a 50 μm aperture tube which reduced the noise floor sufficiently to make volume measurements as low as 20 fl. Since the glycerol permeability parameter is temperature dependent, a water jacketed beaker was used as the sampling vessel. The jacketed beaker was connected to a temperature-controlled bath and circulated with 20 °C water. For the cell suspension in the beaker to be considered well mixed, the beaker was affixed atop a customized platform with a micro stirring motor in the base that manipulated a small stir bar in the jacketed beaker.

With this entire setup in place, the door to the Coulter counter needed to be open to allow for the water supply and return lines as well as to allow for cell injection. Since this would result in a much higher experimental noise than during normal operation, several steps were employed to reduce noise and ensure run-to-run accuracy. First, it was very

important that the tubing for the water line was secured to the Coulter counter using tape, as any movement of the tubing introduced a large amount of noise into the readings. Second, the magnetic stirrer and the movement of water in the jacketed beaker imparted a large amount of electrical noise into the readings. To deal with this a wire "faraday cage" was inserted into the water jacket portion of the beaker and grounded by a wire to the chassis of the Coulter counter. Introduction of an electrolyte into the water bath (2% NaCl) further reduced this interference. Finally, all calibration and noise floor measurements needed to be taken with the full experimental setup running in the exact way that a cell sample would be introduced into the Coulter counter. Calibration was performed with 5 µm latex beads (Beckman Coulter, IN, U.S.), however, the Coulter counter cannot be calibrated properly with spherical beads when measuring erythrocytes, so an additional shape factor correction was employed which is discussed in further detail in section 3.3.1.5.

3.3.1.4. Sample injection and experimental procedure

A volume of 0.15 ml of each dilute cell solution was loaded into a syringe prior to each run. 10 ml of exposure solution was allowed to come to temperature equilibrium in the jacketed beaker and then the instrument was zeroed to eliminate electrical noise that may manifest as an erroneous cell count. The cell solution was injected simultaneously to pressing the capture button ensuring the time of the highest solute gradient, when the cells are first injected, was accurately recorded. Each run consisted of a series of cell volume measurements (~3000 counts) recorded over 10 s intervals followed by a pause time between measurement intervals. After initial test runs the procedure timing was

adjusted to ensure the new steady state cell volume was reached. The low solution osmolality experiments consisted of six 10-second volume measurements followed by no wait time for a total experiment time of 1 minute. The high concentration solution experiments consisted of fifteen 10-second measurement intervals with 5 minutes of spacing, for 75 minutes of total experiment time.

Data was recorded as individual pulses corresponding to a single cell volume. All volumes below 20 fl and above 150 fl were ignored which are well outside of the range expected for intact erythrocytes under all experimental conditions. This also eliminated erroneous data below the noise floor. This cutoff additionally excludes larger white blood cells and double pulses from multiple cells entering the aperture simultaneously.

3.3.1.5. Shape factor correction

It has been observed that human erythrocytes do not give accurate cell volumes in a Coulter counter due to their biconcave-discoid shape and high deformability [132, 133]. Coulter counters are typically calibrated with rigid spherical beads that yield the same particle volume no matter their orientation as they flow through the aperture. This method of calibration is reasonably effective for most cell types because of their approximately spherical shape. However, the non-spherical shape of erythrocytes leads to an apparent volume that depends on the cell orientation as it flows through the Coulter counter aperture. Typically, a red cell will flow through the aperture in an orientation that will make it appear smaller than its actual volume [132]. To account for this phenomenon a shape factor correction was applied to bring the measured volume in line with the known volume of erythrocytes. The shape factor, α, is calculated as,

$$\propto = \frac{V_{apparent}}{V_{actual}}.$$

The actual erythrocyte volume was determined for each blood sample under isotonic conditions using a hematology analyzer (ABX Micros 60 hematology analyzer, HORIBA ABX SAS, Kyoto, Japan) that had been calibrated using standard methods for clinical laboratories.

The magnitude of the shape factor α is expected to depend on shape of the cell, which changes during the experiments as a result of cell swelling. When an erythrocyte expands from its isotonic state, it will typically become more spheroid in shape [134]. For simplicity, we assumed the shape factor varied linearly with cell volume. Shape factor correction was applied simultaneously with the fit to the data to determine the glycerol permeability, as described in detail below.

3.3.1.6. Fitting the cell volume data to determine the glycerol permeability

To determine the cell membrane permeability to glycerol, cell volume predictions were fit to cell volume measurements after applying a shape factor correction. The cell volume *V* can be expressed in terms of the volumes of intracellular water, glycerol and osmotically inactive components:

$$V = W + \bar{v}_s S + \bar{v}_b V_{iso}$$

where *W* is the intracellular water volume, $\bar{v}_s$ = 71 mL/mol is the molar volume of glycerol, *S* is the moles of intracellular glycerol, $\bar{v}_b$ = 0.43 is the osmotically inactive

volume fraction [135], and V_{iso} is the cell volume under isotonic conditions. The value of V_{iso} was determined for each blood sample using a hematology analyzer, as described above.

Values of W and S were predicted as a function of time by numerically solving the two-parameter model [51]:

$$\frac{dW}{dt} = -L_p ART\left(M_n + M_s - \frac{N+S}{\rho_w W}\right), \quad (1)$$

$$\frac{dS}{dt} = P_s A\left(M_s - \frac{S}{\rho_w W}\right), \quad (2)$$

where, L_p is the hydraulic conductivity, P_s is the glycerol permeability, A = 130 μm^2 is the cell membrane surface area [136], R is the ideal gas constant, T = 293 K is the temperature, M_n is the extracellular osmolality of nonpermeating solutes, M_s is the extracellular glycerol osmolality, ρ_w = 1 kg/L is the density of pure water and N is the osmoles of intracellular nonpermeating solutes. Intracellular nonpermeating solutes are retained within the cell and thus N remains constant and can be defined as $N = M_{iso} W_{iso} \rho_w$, where M_{iso} = 290 mOsm/kg is the isotonic osmolality and $W_{iso} = V_{iso}(1 - \bar{v}_b)$ is the cell water volume under isotonic conditions. The value of L_p was calculated using the concentration dependent model from our previous work [125], resulting in L_p = 2 x 10^{-6} μm Pa^{-1} s^{-1} for the experiments under isotonic conditions and L_p = 2 x 10^{-7} μm Pa^{-1} s^{-1} for the experiments in 40% glycerol.

The predictions for cell volume as a function of time were used to apply a shape factor correction to the experimental data. As described above, we assumed that the shape factor varied linearly with cell volume. To establish this linear relationship, we defined shape factor values corresponding to the initial and final (steady-state) cell volumes (α_i and α_f, respectively), resulting in the following equation for the shape factor as a function of cell volume:

$$\alpha = \alpha_i + (\alpha_f - \alpha_i)\left(\frac{V - V_i}{V_f - V_i}\right)$$

This equation was used to assign a shape factor corresponding to the predicted cell volume at each time point. This α-value was then used to correct each of the Coulter counter volume measurements. To apply this shape factor correction, the initial and final cell volumes must be known. In the initial and final states, the cell is in equilibrium with its environment. The equilibrium cell volume V_{eq} can be calculated based on the solution composition using the following equations:

$$V_{eq} = W_{eq} + \bar{v}_s S_{eq} + \bar{v}_b V_{iso}$$

$$W_{eq} = W_{iso}\frac{M_{iso}}{M_n}$$

$$S_{eq} = M_s W_{eq} \rho_w$$

Best-fit values of P_s, α_i and α_f were determined by varying the values of these parameters to minimize the sum of the error squared between the predicted cell volume and the shape-factor-corrected cell volume measurements.

3.3.2. Mathematical optimization of deglycerolization procedures

Our mathematical optimization approach was similar to that described in our previous study [19]. The basic approach is to identify the fastest method for going from 40% glycerol to isotonic conditions without causing excessive cell volume changes. We considered 3-step procedures in which the cells were diluted with saline solution in each step, reaching isotonic conditions in the third step. The saline concentration, dilution factor and duration of each of the first two steps were varied in the optimization algorithm. The solution composition in the third step was fixed at isotonic conditions with negligible glycerol concentration. For each candidate 3-step procedure, cell volume changes were predicted by numerically solving Eqs. 1 and 2 using Heun's method. These predictions were used to exclude procedures that cause excessive cell volume changes by using the osmotic tolerance limits as constraints on cell volume. The optimal procedure was defined as the shortest procedure that did not violate these cell volume constraints.

In our previous work, we assumed that the glycerol and water permeability values were constant and did not vary during the deglycerolization process [19]. However, we recently completed a comprehensive review of the RBC permeability literature and found that both water and glycerol permeability vary substantially over the range of concentrations encountered during deglycerolization [125]. In this study, we improve upon our previous approach by using concentration dependent models for both water and glycerol permeability. In addition, we assumed in our previous study that the methods we designed using a single glycerol permeability value could be applied to all RBCs. However, there is evidence in the literature that the glycerol permeability varies within a population of RBCs (Jay and Rowlands 1975). To account for this cell-to-cell variability,

we predicted cell volume changes for a “slow” cell (with low glycerol permeability) and a “fast” cell (with high glycerol permeability) and applied the cell volume constraints to these predictions. This enables design of methods that avoid excessive cell volume changes for cells with permeability values that span the range between the slow and fast cells.

The mathematical optimization was carried out using custom-written code in MATLAB (MathWorks, Inc., Natick, MA). The MATLAB function “fmincon” was used to implement the interior point algorithm [137-139] to minimize the duration of the deglycerolization method using the osmotic tolerance limits as constraints on the cell volume. To increase the likelihood of finding a global minimum, a grid search approach was used with a wide range of initial guesses for the saline concentrations, dilution factors and step durations.

3.3.3. Evaluation of the mathematically optimized procedures

Testing of the mathematically optimized deglycerolization procedure was conducted in the same manner as Lusianti et al. [19]. First, blood was collected from volunteer donors, glycerolized, frozen and stored in 1 mL aliquots at -80 °C. Batches of frozen blood were stored for up to 1 month before being used in experiments.

Immediately prior to each experiment, an aliquot of frozen blood was thawed in a 37°C water bath for 1 minute. The frozen-thawed blood was divided into two equal volumes, one for measuring the total hemoglobin and one for the deglycerolization experiment. For the deglycerolization experiment, the blood was transferred to a round bottom flask on a linear shaker, and a series of solution additions were performed to bring

the cells to isotonic conditions as outlined in Table 3.2. After the final addition, the cell suspension was centrifuged at 1,400 g for 10 minutes and the supernatant analyzed for hemoglobin using Harboe's direct spectrophotometric method [140]. Total hemoglobin was determined by diluting the same volume of blood from the same aliquot used in the deglycerolization 1:1000 into DI water and pipetting vigorously to lyse the cells. The total hemoglobin was compared to the hemoglobin in the supernatant from the deglycerolization experiment to determine percent hemolysis as follows:

$$\%\ Hemolysis = \frac{Supernatant\ Hemoglobin * (100 - \%\ Hematocrit)}{Total\ Hemoglobin}.$$

Two types of mathematically optimized procedures were examined. The solution compositions and exposure times for these methods are shown in Table 3.2. The same four donors were used in both procedures. The first procedure consisted of a single experiment from each donor for each set of deglycerolization times tested. For the second procedure each donor was tested in triplicated for each set of deglycerolization times. All diluent solutions consisted of saline, buffered with 12 mM disodium phosphate, and adjusted to a pH of 7. In the third dilution step, the diluent solution also contained 0.2% glucose. Initially, we tested a 3 step method that was designed using the cell volume constraints from our previous paper [19] and a glycerol permeability range from 50% to 150% of the concentration dependent permeability value (see Eq. 3 in the results section). We tested this mathematically optimized method, as well as similar methods with exposure times in the vicinity of the optimum. We then examined methods designed to be more robust using a more conservative upper osmotic tolerance limit and a broader range of glycerol permeability values.

Table 3.2. Deglycerolization methods and solution compositions

	Initial Mathematically Optimized Procedure [a]		More Conservative Mathematically Optimized Procedures [b]	
Step	Addition	Final Composition	Addition	Final Composition
Initial	n/a	0.1 mL Thawed RBC	n/a	0.2 mL Thawed RBC
1	0.322 mL 8.3% saline, wait for 29 s, **39 s** [c], 49 s	M_n: 2300 mOsm/kg M_s: 1000 mOsm/kg	0.230 mL 6.7% saline, wait for 1.85–20 min	M_n: 1550 mOsm/kg M_s: 2170 mOsm/kg
2	0.247 mL 0.14% saline, wait for 80 s, **100 s** [c], 120 s	M_n: 1400 mOsm/kg M_s: 600 mOsm/kg	5.11 mL 4.4% saline, wait for 0.9–10 min	M_n: 1340 mOsm/kg M_s: 140 mOsm/kg
3	40.0 mL 0.66% saline	M_n: 300 mOsm/kg M_s: ~0 mOsm/kg	35.0 mL 0.23% saline	M_n: 300 mOsm/kg M_s: ~0 mOsm/kg

[a] *Mathematically optimized procedure using cell volume constraints defined as* $0.22 < (W + \bar{v}_s S)/W_{iso} < 1.63$*, and a glycerol permeability range from 50% to 150% of the concentration-dependent permeability defined in Eq. 3 (see Results)*

[b] *More conservative procedures designed using cell volume constraints defined as* $0.22 < (W + \bar{v}_s S)/W_{iso} < 1.5$ *and glycerol permeability down to 5% of the concentration dependent value defined in Eq. 3.*

[c] *Bold times denote the time output from the mathematical optimization; other times are a systematic investigation around the optimized times.*

3.3.4. Statistics

Statistical analysis for the tested deglycerolization procedures was carried out by 2-way ANOVA using experiment time as the independent variable and donor as a blocking factor. Significance between groups was determined with Fisher's least significant differences method. All analysis was done using Statgraphics software (Statpoint

Technologies, Inc., The Plains, VA). Results are presented as the mean ± the standard error of the mean.

3.4 Results

3.4.1. Concentration dependent permeability parameter

The output of the Coulter counter is a series of volume measurements made on cells undergoing swelling due to influx of glycerol. These measurements are first corrected with the shape factor correction to account for the non-spherical shape of the red blood cells. Figure 3.1 (left) shows that the red blood cell volume measured using a Coulter counter, which was calibrated with rigid spheres, is much lower than the volume measured using a hematology analyzer, which was calibrated using a clinical reference sample with known red blood cell volume. Figure 3.1 (right) shows a representative transient volume response of red blood cells during glycerol influx. After applying the correction, the cell volumes are in line with those measured on the calibrated hematology analyzer.

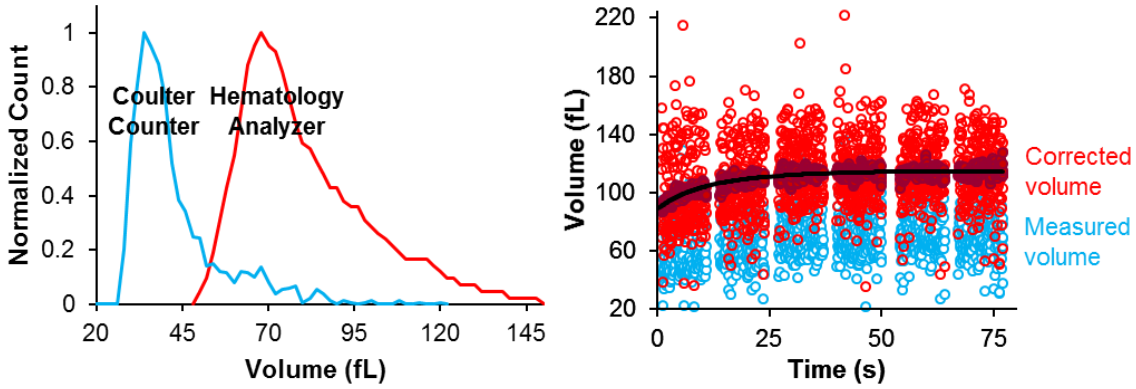

Figure 3.1. Measurement of cell membrane permeability to glycerol*. Left: Representative RBC volume distributions under isotonic conditions measured using a*

Coulter counter and a hematology analyzer. Volumes measured using the Coulter counter are erroneously low because of the RBCs' non-spherical shape. Right: Representative transient response of RBCs after exposure to an isotonic solution containing glycerol. To fit the data for the membrane permeability to glycerol, the volumes measured using the Coulter counter (blue symbols) were first corrected for shape effects (red symbols). The dark red symbols show a running average over 60 consecutive data points, and the solid line shows the best-fit curve using Eqs. 1 and 2. The initial and final shape factors for this fit were $\alpha_1 = 0.659$ and $\alpha_2 = 0.670$ which are explained in more detail in Section 3.3.1.5.

After applying the shape factor correction and fitting the data to the two-parameter model, the resulting glycerol permeability is $P_s = 3.43 \pm 0.11$ μm/min under isotonic conditions and $P_s = 0.65 \pm 0.12$ μm/min in the presence of 40% glycerol. Figure 3.2 shows other published values for human erythrocyte permeability, expressed as the permeability parameter, P_sA/W_{iso}, in which P_s is combined with the constants A and W_{iso} [125]. The measured permeability parameters from this study are $P_sA/W_{iso} = 0.145 \pm 0.004$ s^{-1} and $P_sA/W_{iso} = 0.027 \pm 0.005$ s^{-1} for the low and high glycerol concentrations respectively and appear to be in good agreement with the other published values.

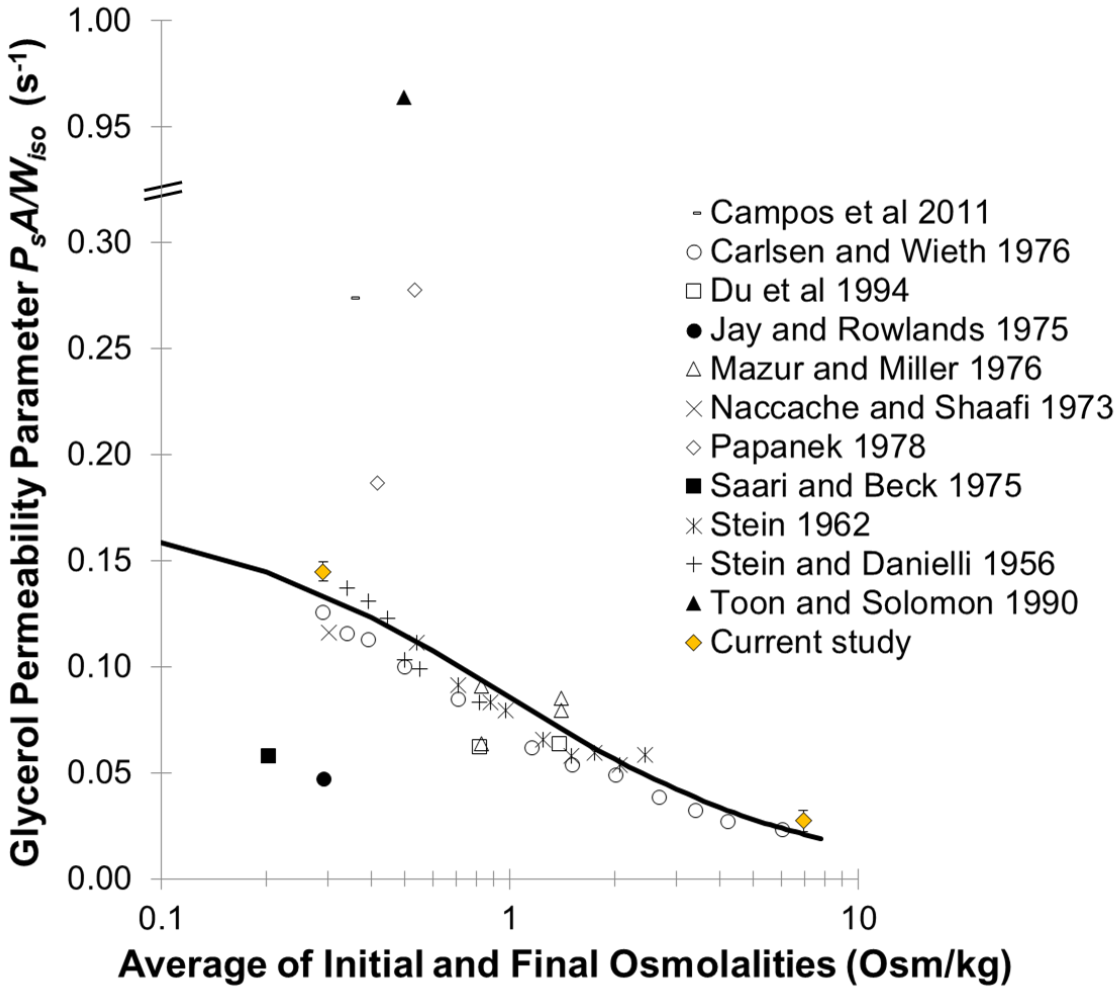

Figure 3.2. Effect of solution osmolality on the glycerol permeability of human RBCs at room temperature, 20°C-25°C, from the literature and this study *[38, 58, 59, 76, 80, 83, 88, 92, 94, 102, 103]. The line shows the best-fit concentration-dependent permeability model which we previously reported on and have updated here to include the data in this work [125]. The data point from Toon and Solomon was omitted from the fit [80].*

In our recent work we established a concentration dependent permeability parameter using a phenomenological fit to the published values. This equation, which based on saturation kinetics, is of the form,

$$\frac{P_s A}{W_0} = \frac{a_s}{b_s M + 1}, \quad (3)$$

where M is the solution osmolality, and a_s and b_s are fit parameters [125]. Figure 3.2 shows the updated fit for the concentration dependent permeability parameter which includes the data from this study. The new parameter values for the concentration dependent fit equation are a_s = 0.175 s^{-1}, and b_s = 1.05 kg/osmol.

3.4.2. Mathematically optimized 3-step deglycerolization procedures

In a previous study we mathematically optimized a 3-step deglycerolization method using a constant glycerol permeability of P_s = 1.8 μm/min, resulting a method with a duration of less than 1 minute; while the predictions were promising, experimental evaluation of the optimized method resulted in unacceptable levels of hemolysis [19]. Here we improve upon our previous approach by considering both concentration-dependence and variability in the glycerol permeability in the optimization algorithm. Figure 3.3 shows cell volume predictions for a 3-step deglycerolization procedure that was mathematically optimized using a permeability range defined as 50% to 150% of the concentration dependent permeability (Eq. 3). In the first step of this procedure, addition of saline solution causes rapid influx of water that brings the cell up to the upper osmotic tolerance limit nearly instantaneously, while glycerol leaves the cell at a much slower

pace slowly shrinking the cell toward the lower osmotic tolerance limit. Predictions are shown for a "fast" cell with glycerol permeability of 150% of the concentration dependent value, and for a "slow" cell with glycerol permeability of 50% of the concentration-dependent value. The fast cell shrinks until it just reaches the lower osmotic tolerance limit. The next saline addition results in another rapid influx of water and the cell with the lower glycerol permeability, which has higher internal glycerol, takes in more water and reaches the upper cell volume limit. In the final step a similar trend is seen.

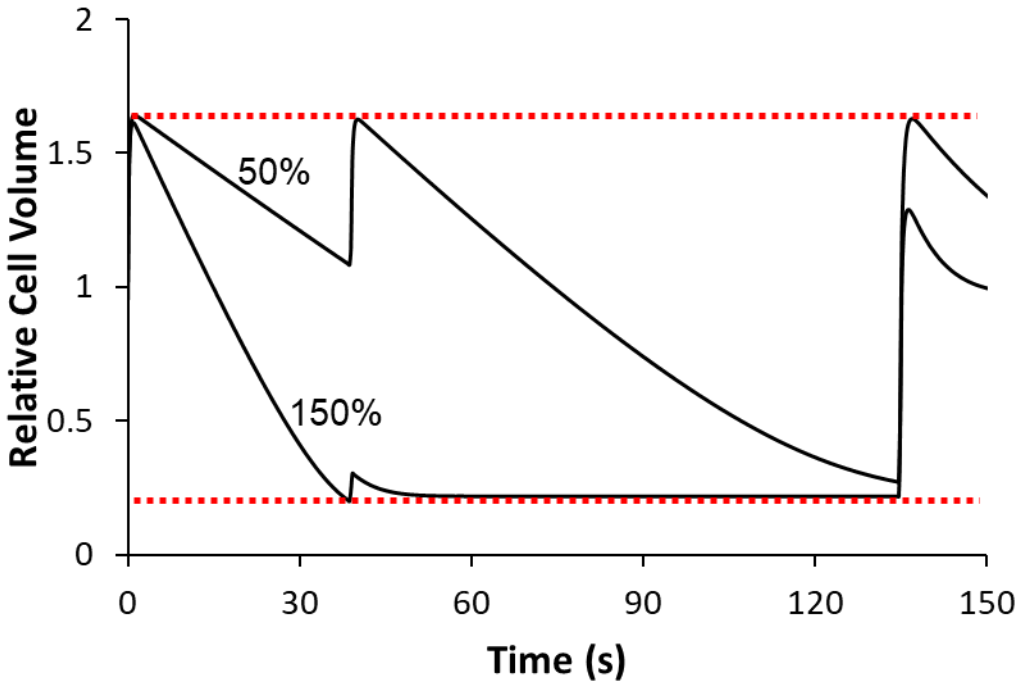

Figure 3.3. Cell volume predictions for the 3-step deglycerolization procedure optimized using a glycerol permeability range from 50% to 150% of the concentration dependent permeability parameter given by Eq. 3*. Volume predictions for the fastest and slowest responding cells are shown. The upper and lower cell volume constraints are*

shown with the dashed red lines. The relative cell volume on the vertical axis is the relative osmotically active cell volume defined as $(W + \bar{v}_s S)/W_{iso}$.

The hemolysis results from testing the 3-step optimized procedure are presented in Figure 3.4. The time given by the optimized procedure was 39 s in the first step and 100 s in the second step. A systematic investigation of ±10 s for the first step and ± 20 s for the second step was conducted to examine if small changes in the step timing would improve the results. There was no significant difference in hemolysis between any of the timing groups. Hemolysis for the optimized procedure was 39.7% ± 6.9 %. In contrast, we previously obtained a much higher hemolysis of 70.5% for a mathematically optimized procedure using a fixed value for P_s [19].

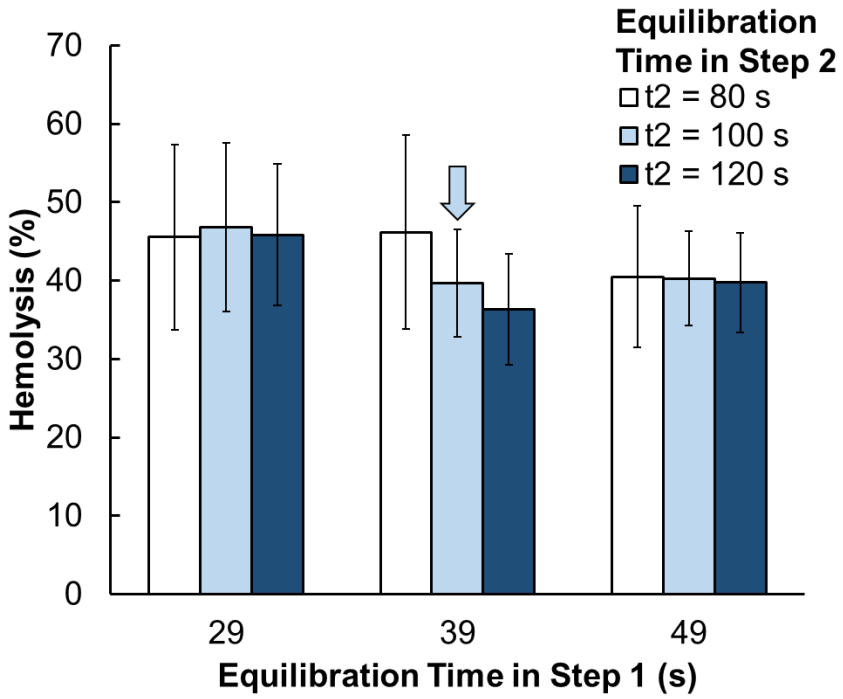

Figure 3.4. Hemolysis results for the 3-step optimized deglycerolization procedure with a glycerol permeability range of ±50% of the concentration dependent permeability parameter presented in this work*. The arrow denotes the mathematically optimized procedure. The other procedures are a systematic investigation of step timing around the optimum. Each mean is the average of 4 data points, each of which was obtained using blood from a separate donor.*

While the mathematically optimized method shown in Figures 3.3 and 3.4 is an improvement over our previous method, the levels of hemolysis are still too high for clinical application. Thus, we sought to develop more conservative methods. First, we applied a more conservative upper osmotic tolerance limit while keeping the permeability range at 50% to 150% of the concentration dependent permeability. Predictions for the

resulting mathematical optimized method are shown in Figure 3.5A. Reducing the upper osmotic tolerance limit resulted in a method that was slightly longer than that shown in Figure 3.3, with similar cell volume trends. The main difference can be seen in the first step of the deglycerolization method. The more conservative method results in equilibration of the “fast” cell at the lower osmotic tolerance limit, whereas our previous method shown in Figure 3.3 would result in an equilibrium volume below the lower osmotic tolerance limit. Consequently, extending the duration of the more conservative method is not expected to result in excessive shrinkage for the fast cell, and the timing of solution exchanges is driven entirely by how long it takes to remove sufficient glycerol from the slow cell. As shown in Figure 3.5D, the hemolysis values for this more conservative method range from about 34% to 83%, depending on the donor. This is similar to the hemolysis values shown in Figure 3.3 and is still too high for clinical application.

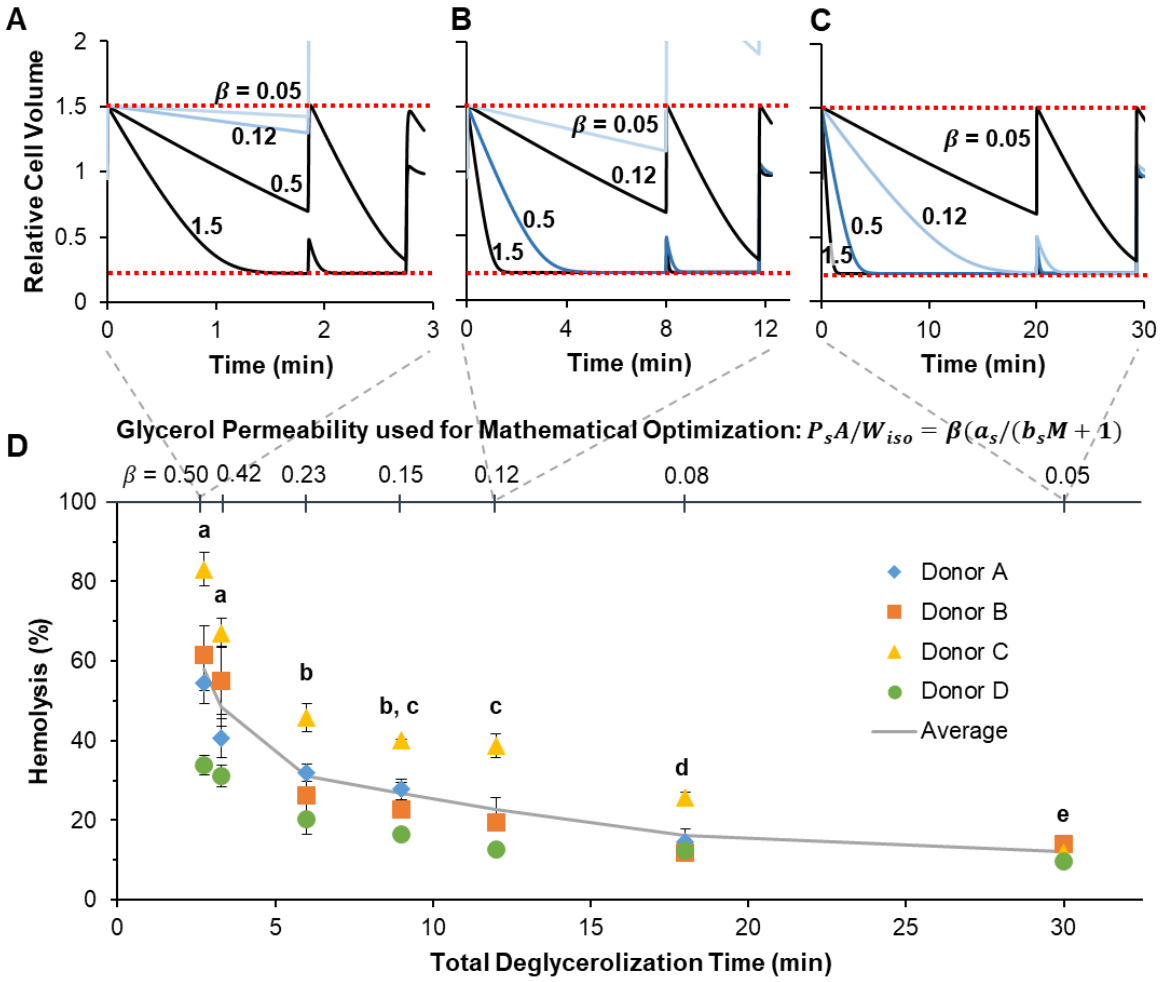

Figure 3.5. Effect of expanding the glycerol permeability range on the mathematically optimized procedures. *In all cases, the osmotic tolerance limits (OTLs) were set at* $0.22 < (W + \bar{v}_s S)/W_{iso} < 1.50$, *and the highest glycerol permeability was 150% of the value from the concentration dependent model (Eq. 3). The lowest glycerol permeability was varied from β = 5% to 50% of the value from the concentration dependent model. Panels A-C show cell volume predictions for mathematically optimized procedures with β = 50%, 12% and 5%. The dashed red lines show the OTLs. Panel D shows experimental results for mathematically optimized procedures for various β values. Each data point shows the average hemolysis for individual donors (n = 3), emphasizing the donor*

sensitivity to the deglycerolization procedures; the average of all donors is given by the line. Statistically homogeneous groups are denoted by the like lowercase letters; distinct letters indicate a significant difference ($p < 0.05$).

Therefore, we examined the effects of broadening the permeability range in the optimization algorithm. In particular, we postulated that a portion of the cells were responding more slowly during deglycerolization. To examine this possibility, we defined a permeability scaling factor β, and designed methods using β values ranging from 0.05 to 0.5 (i.e., permeability values ranging from 5% to 50% of the concentration dependent value given by Eq. 3). Figure 3.5A-C shows optimized methods for $\beta = 0.5$, $\beta = 0.12$ and $\beta = 0.05$. In each of these panels, the black lines show the cell volume predictions corresponding to the permeability range used during optimization. The blue lines show predictions for other β values. In general, the effect of reducing β is to extend the duration of the method, without changing the composition of the solutions in each step. The shortest method is shown in Figure 3.5A; in this case the method is expected to be effective for cells with glycerol permeability greater than 50% of the concentration dependent value. However, more slowly responding cells (depicted by the blue lines for $\beta = 0.12$ and $\beta = 0.05$) are expected to swell beyond the upper osmotic tolerance limit and lyse. The slowest method is shown in Figure 3.5C; this method is expected to be effective for cells with glycerol permeability greater than 5% of the concentration dependent value.

When total deglycerolization time is extended in this manner, a trend of lower hemolysis at longer times emerges, as shown in Figure 3.5D. The fastest method had a duration of less than 3 minutes and resulted in an average hemolysis of 58% ± 10%, while the slowest method lasted 30 minutes and resulted in 12% ± 1% hemolysis. This decrease in hemolysis is statistically significant ($p < 0.0001$) and indicates that there is a subset of slower responding cells within the population that requires a longer deglycerolization time. Individual donors are broken out in Figure 3.5 to illustrate the broad range of response to deglycerolization. This donor to donor variability is more pronounced at shorter times with hemolysis converging at longer deglycerolization times. Donor had a statistically significant effect on hemolysis ($p < 0.0001$) and pairwise comparison of hemolysis values between donors resulted in significant differences in all cases with the exception of the comparison between donors B and C. The AABB standard for deglycerolized blood is recovery of at least 80% of the RBCs, which corresponds to a hemolysis level of less than 20% [42]. For donor D, a method with a duration of only 9 minutes (which is 5 times faster than the current state of the art) resulted in only 16% ± 1% hemolysis, meeting the clinical standard. However, this 9 min method yielded hemolysis values exceeding 20% for the other three donors. The 30 min deglycerolization method yielded hemolysis values lower than 14% for all four donors.

3.5 Discussion

There have been many glycerol permeability measurements made over the past half-century, but only one study by Carlsen and Wieth had extended permeability measurements into the upper range of concentrations used in the high-glycerol method

for cryopreservation [38]. These are important values to consider since at high concentrations glycerol transport appears to be much slower. Here we add to the existing literature by providing measurements at the two relevant extremes for deglycerolizing frozen-thawed RBCs in 40% glycerol, confirming the trend that was first observed over forty years ago.

Based on this new data, we developed a concentration dependent permeability model and used it for design of RBC deglycerolization methods. We initially accounted for cell to cell variability by predicting the response of cells with glycerol permeability ranging from 50% to 150% of the value from the concentration dependent permeability model. This permeability range was chosen based on data presented by Jay and Rowlands [102], who reported a normal distribution of glycerol permeability values with a standard deviation of ± 25%. Based on this, we expected that a permeability range of ± 50% (i.e., about two standard deviations) would account for about 95% of the cell population. However, the resulting deglycerolization methods yielded hemolysis exceeding 35%; clearly this approach was not effective for 95% of the cell population, as we had originally expected.

We were able to obtain improved results by using a broader range of permeability values for designing deglycerolization methods, but this also extended the duration of the procedure. For example, decreasing the glycerol permeability from 50% to 5% of the concentration dependent value increased the protocol duration from ~ 3 min to 30 min, but also substantially decreased hemolysis from about 58% to 12%. These results suggest a much slower responding cohort of cells than we had originally anticipated. In addition to this cell-to-cell variability, we also saw a very broad distribution of response

to deglycerolization between donors. The combination of cell-to-cell variability and donor-to-donor variability makes it particularly challenging to design methods for rapidly removing glycerol from frozen-thawed RBCs.

3.5.1. Cell-to-Cell Variability

Our observation of reduced hemolysis for longer deglycerolization times is consistent with a cohort of cells with much lower glycerol permeability than that predicted based on the permeability data shown in Figure 3.2. Nearly all of these permeability measurements were made on a suspension of RBCs and as a result represent the "average" response of the cell population. When making permeability measurements on an entire population of cells the subtleties of a small fraction of cells having far reduced response or even no response is easily lost due to the rapid shift in volume for a large percentage of the cell population. Thus, it is possible that previous permeability data does not accurately reflect a subpopulation of RBCs with relatively low glycerol permeability, either due to reduced expression of the glycerol transporting protein aquaporin 3 (AQP3) or loss of AQP3 functionality. Previous studies suggest that this subpopulation of cells may be a result of the RBC aging process.

Significant consideration has been given to the morphological and physiological changes that occur over the typical 120-day period of an erythrocyte's lifespan, with much attention given to understanding the final senescent phenotype as the cells approach eryptosis [141-148]. During the normal aging process erythrocytes are constantly remodeling their membrane structure. The remodeling results in the loss of and

alterations to the bilayer components, irreversibly altering protein composition and function [141-143, 145, 148-151].

One of the clearest consequences of aging is the loss of membrane bilayer by exovesiculation, a phenomenon that has been observed in cells of various age and studied *in vitro,* and to a lesser extent, *in vivo* [141, 142, 149]. Prior to shedding of exocytic vesicles, a rearrangement of membrane proteins takes place creating protein-poor sections that may be more readily lost to exovesiculation [142, 143]. Loss of these membrane protein-poor vesicles results in changes to the erythrocyte membrane topography causing protein aggregation, potentially making them more susceptible to crosslinking [145]. Erythrocytes also lose antioxidant function as they age, resulting in oxidation of membrane proteins [146]. These modifications to the membrane structure play a major role in preparing and signaling for removal through eryptosis [145, 152]. However, erythrocyte membrane modification due to age may also result in a subpopulation of cells with altered transport function.

Several studies have investigated age-related changes in membrane protein band 3 function [145, 146, 148, 150, 152]. A breakdown of the band 3 protein has been observed as erythrocytes age and an increased susceptibility to band 3 crosslinking has been reported in older erythrocytes [145, 146, 148, 150]. Loss of band 3 function has many implications for erythrocyte aging and removal, but it also appears to have a direct functional relationship with multiple transport processes. Bartosz and Gwozdzinski studied ion transport in aging cells and found that loss of band 3 function resulted in a significant reduction in transport of a spin labeled anion [144]. Bosman and Kay found that a degradation in band 3 in aged erythrocytes resulted in increased glucose efflux and

reduced influx but saw no change in L-glucose permeability or hemolysis leading them to conclude there were no problems with the integrity of the membrane bilayer, but protein transport function had been compromised [150]. Other changes in permeability have been reported with less direct correlation to the age-related changes in the membrane protein structure [153-155], however, there is consensus that cell age plays a direct role in the deviations from normal transport function.

Based on these previous studies of the effects of cell age on membrane transport function, it is plausible that a small constituent of the oldest erythrocytes have undergone morphological and functional changes which have led them to have impaired glycerol transport function. This is consistent with previous work by Pallotta et al. which showed the disappearance of the densest RBCs after freeze-thaw and deglycerolization, leading them to hypothesize the oldest cells are lysing. While there is no direct evidence that the densest bands of cells that disappeared after washing had reduced glycerol permeability, this explanation is consistent with the results of the current study, which shows that the slower responding RBCs are more susceptible to damage during deglycerolization.

While our results can be explained in terms of a cohort of cells with relatively low glycerol permeability, there are other possible explanations for our observation that extending the deglycerolization time reduced hemolysis. One possibility is uptake of salts during cryopreservation and the subsequent requirement for a slower washing process to remove these intracellular salts. Post-hypertonic hemolysis was proposed over 50 years ago as a mechanism by which cells lyse upon return to isotonic conditions as a result of internalization of ions during exposure to hypertonic conditions [122, 130, 156]. When a concentration of approximately 0.8 M ionic solute is reached during freezing, the RBC

membrane becomes leaky to cations [130, 157]. This causes the cell to load with salts, upsetting the isotonic balance and causing post storage lysis when attempting to return the cell to isotonic conditions. Mechanisms and models have been proposed to explain this phenomenon, but there has been no consensus on mechanisms of the salting-in process [158, 159]. If the RBCs have a higher internal solute concentration than expected after thawing, the longer deglycerolization times may be allowing them to rebalance their ionic solutes. In this case the ion transport rate of slower responding cells becomes the limiting step for which the exact mechanisms and kinetics are not currently known.

Another possible explanation for our observation of reduced hemolysis for longer deglycerolization times is changing levels of AQP3 in the membrane due to aquaporin translocation. Recently there has been work examining the role of aquaporin translocation as a regulatory mechanism for cells responding to environmental stimuli [160]. Aquaporin translocation could result in slower glycerol transport if erythrocytes were to remove the aquaporins responsible for glycerol transport from the membrane in response to their environment, such as being exposed to high solute concentrations. Submembrane translocation of AQP4 has even been observed in response to osmotic gradients in HEK293 cells transfected with the human AQP4 gene [161]. We are currently unaware of any direct evidence that aquaporin translocation occurs in erythrocytes, but there has been some investigation into expression of AQP1 in human erythrocytes in response to the environmental stress posed by renal disease. Buemi et al. noticed changes in AQP1 expression levels in uremic patients, with a rapid return to normal levels post hemodialysis [162]. Antonelou et al. observed a similar lowered expression level pre-hemodialysis, and noted more exovesiculation and not much endovesiculation,

corroborating the idea that oxidative damage results in similar morphological and functional changes to aging [163]. Buemi et al. also noted that due to erythrocytes lacking a nucleus, and therefore the cellular mechanisms for transcription, the changes in expression levels of AQP1 witnessed is likely due to modification of the protein structure and not subsurface relocalization [162]. It would appear erythrocytes utilize other mechanisms to deal with environmental stresses than the cell types in which these translocation phenomena have been observed. Further research is needed to understand if and to what extent erythrocytes undergo aquaporin translocation, which could have implications not only for the variability in permeability parameters in response to high osmotic gradients, but also for the concentration dependence of glycerol transport.

3.5.2. Donor-to-donor variability

We observed a significant difference in the hemolysis post deglycerolization in different populations of cells between donors. Several studies have examined the differences between donors' erythrocyte lysis time using a glycerol lysis test (GLT) in the context of a clinical diagnostic tool for certain hemopathic diseases [164-167]. Additionally, the same glycerol lysis tests have been performed to investigate the impact of chemical exposure, drug exposure, or heredity on the rate of erythrocyte lysis in response to glycerol [164, 168, 169]. It is also important to note that while osmotic fragility can potentially be a factor in these tests, there is often little correlation between osmotic fragility, tested using decreasing NaCl compositions, and glycerol lysis time [164, 168]. As an example of the range of lysis times one could expect for different disease states, Sauer et al. used an acidified glycerol lysis test and found an average time

for 50% hemolysis of 53.7 s, 162 s, and > 600 s, for hereditary spherocytosis, control, and β-thalassemia minor, respectively [170]. While it is entirely possible one or multiple of our donors exhibited some level of reduced glycerol permeability due to a disease state, prescription drug use, or iron deficiency, etc., what is interesting is how broad the range for "healthy" GTL values are. Typically GLT values have a range of at least 50 to 150% of the average value, and in some cases cells take many times longer to lyse [164, 165, 170]. These large discrepancies in the range for glycerol transport between donors is well illustrated with the converging hemolysis data illustrated in Figure 3.5. As glycerol is given more time to leave the cells of the slower responding donors, the hemolysis converges and the distribution of permeability within the erythrocyte population becomes the greater factor influencing hemolysis. Another important observation to note, which has additional implications in cell-to-cell variability, is the reduced rate of lysis of the final 10 to 20 % of cells in glycerol lysis tests [164, 170]. It is obvious that a certain percentage of the cells respond much slower to glycerol within an individual donor, though little attention has been paid to the reasoning for this mechanism in past works.

3.5.3. Implications of variability in Ps for design of CPA equilibration methods

Erythrocytes are not the only cells to have a broad range of cryoprotectant permeabilities. Oocytes are a good example of cells that have also been shown to have a broad range of permeability values, and unlike erythrocytes, permeability measurements are able to be made on individual oocytes giving true measurements on a cell-to-cell basis [171]. Van den Abbeel et al. measured the permeability of oocytes to several different CPAs and found standard deviations to be ±24% to over ±50% of the mean indicating a

very large distribution of permeabilities [171]. Although this current work is specific to erythrocyte deglycerolization, it is easy to see how incorporating a distribution of permeability parameters could be extended to the many other cell types and cryoprotectants encountered in cryobiology mathematical modeling. Procedures optimized with this strategy have a lot higher likelihood of better representing the realities encountered when dealing with the diversity of biological systems.

3.6 Conclusions

Here we have added our own permeability measurements at the two glycerol concentration extremes that are relevant for the high glycerol method for erythrocyte cryopreservation. We have updated the concentration dependent permeability parameter which we have previously reported on and used it in the 2-P model to optimize deglycerolization protocols. We found the new optimized procedure to have much higher hemolysis than expected, so we investigated extending deglycerolization time. Our findings indicate there is a much larger discrepancy in glycerol permeability than expected in human erythrocytes both for the cell-to-cell response within an individual, and between different donors. These factors will make ultra-rapid deglycerolization very challenging. In this study we were able to reduce deglycerolization time to as low as 9 minutes while meeting the established criteria for cell recovery for one of the donors; to meet the criteria for all four donors a deglycerolization time of 30 min was required. A promising direction for future work in reduction of deglycerolization time would be employing elevated temperatures during the process to speed up glycerol transport.

3.7 Acknowledgements

We would to thank the volunteer blood donors for providing blood samples for this study, as well as the Oregon State University Student Health Center for performing blood collections and providing use of their hematology analyzer. This work was supported by a National Science Foundation grant to A.Z.H. (Grant No.1150861).

Chapter 4: Effect of Bifurcations on the Clearance of Biotinylated Lipopolysaccharide (LPS) from Blood in High Aspect Ratio Microchannels

John M. Lahmann, Jun Yang, Kendra V. Sharp, Kate F. Schilke, Adam Z. Higgins

4.1 Abstract

Microfluidic blood perfusion is a very promising technology for adsorption of blood constituents due to the unique properties of blood flow in microchannels. One potential application of these devices is the adsorption of endotoxin from patients with sepsis where high efficiency is desired to rapidly treat patients before sepsis symptoms can progress. Here we employ a model system to test the effect of bifurcations in microchannels with different widths to determine if induced mixing has a beneficial effect on endotoxin removal from blood. Microfluidic devices with up to a 4:1 aspect ratio were fabricated from polycarbonate using a double hot embossing process with an intermediate laser machining step. The model system used streptavidin coated channels to bind biotinylated lipopolysaccharide (LPS-biotin) from 40% hematocrit washed human blood. Our results indicated no significant effect of the bifurcations under the experimental conditions for the geometries tested. The 125 μm wide straight channels were the most effective, having a single pass clearance of LPS-biotin of 80% for a 30 s residence time at a flow rate of 1 mL / min. This experimental design proved effective for exploring potential geometries for blood adsorption devices to quantify LPS interaction with the walls of microchannels.

4.2 Introduction

Sepsis is a life-threatening condition responsible for approximately one million hospitalizations per year in the United States with 12.5% of those cases becoming fatal [22, 172]. Sepsis is an inflammatory immune response usually caused by foreign bacteria in the blood which can stem from a primary infection elsewhere such as the gut or lungs.

Symptoms include fever, increased heart rate, low blood pressure and suppressed breathing [23, 24]. Progression of this immune response leads to organ dysregulation, reduced blood flow to the tissues, septic shock, and ultimately, death [23, 24, 173]. The recommended treatment in the US is early intervention with antibiotics to eliminate the bacterial infection and suppression of symptoms with antipyretics and vasopressors [24]. In many cases antibiotics alone are not enough for treatment, because though they help eliminate live bacteria from the bloodstream, bacterial fragments known as endotoxin remain in circulation and continue to cause an inflammatory immune response [25, 174]. Endotoxins are composed of fragments of lipopolysaccharides (LPS) which are bacterial membrane components that are released from live bacteria during exovesiculation and during the destruction of bacteria [25].

Since destruction of live bacteria does not eliminate circulating endotoxin, one potential treatment option for sepsis is cleaning endotoxin from the blood through extracorporeal hemoperfusion devices. Recently this treatment strategy has seen a lot of interest within the scientific and medical communities [25, 29, 30]. Several extracorporeal treatment strategies have been attempted with limited success including hemofiltration, plasmapheresis, adsorption of the inflammatory cytokines, and direct adsorption of endotoxin [175-177]. The most successful and well-known blood cleaning approach is a treatment that involves adsorption of endotoxin to immobilized polymyxin B through a hemoperfusion cartridge [26, 176-178]. Several of these treatment devices are in clinical trials or are approved for use outside of the US [177, 178]. While immobilized polymyxin B hemoperfusion is currently the gold standard for endotoxin removal, it has shown questionable effectiveness in clinical trials, leaving room for

improved treatment strategies [26]. Recently, new functionalized coatings have been applied to hollow fiber cartridges and membranes with highly selective absorption of endotoxin, showing high single pass removal *in vitro* [179, 180].

Microfluidics for extracorporeal blood treatment emerged in the 2000s and has continued to be a promising area of research due to the unique properties of blood flow in microdevices [27, 29, 181]. At the microscale, channel dimensions can be sufficiently reduced so that the residence times required for complete mixing are on the order of a few seconds [182, 183]. Additionally, there are unique flow properties to blood when under laminar flow conditions ($1 < Re < 2300$) in microchannels that result in cell migration, cell margination, and enhanced mixing [182, 184-186]. As such, several applications of microfluidic technology have been proposed to exploit these phenomena for clearance of endotoxin from the blood [27-30]. One such device uses magnetic nanoparticles to bind pathogens and endotoxin and a magnetic spleen-like device to pull the endotoxin from circulating blood [30]. Other devices use flow margination in microchannels to separate bacteria and endotoxin from perfused blood [27, 29].

While microfluidic treatments are promising for blood processing, one limitation is fabrication of larger, scaled up devices that can process more than a few hundred microliters a minute [27-29]. Additionally, many of the rapid-prototyped microfluidic devices for research purposes are fabricated from materials such as polydimethylsiloxane (PDMS) and silicon that would be difficult materials for use in large scale manufacture of treatment devices. Hot embossing has emerged as a potential method for scaled up manufacture of thermoplastic microfluidic devices due to its potential translation to high throughput systems such as roll embossing [187-191]. A downside to using hot

embossing for rapid prototyping is that the master molds are typically time consuming and costly to make [192, 193]. Laser machining of master molds has the potential to make the turnaround time for new masters faster and more cost effective [188, 193]. Both metal and polymer molds have been laser patterned with success achieving up to a 2:1 H:W channel aspect ratio on successfully replicated parts [187, 193, 194]. Nevertheless, channel depths in successfully replicated high aspect ratio devices have remained relatively small which would severely limit most microdevices in blood cleaning applications where up to L/min flow rates are desirable [187, 193].

Here we use a double transfer hot embossing process using a polyethelimide (PEI) master with an intermediate laser patterning step for rapid prototyping of up to 4:1 H:W aspect ratio polycarbonate microchannel devices with maximum heights of 0.5 mm. Multiple geometries are assessed to determine if induced mixing of blood with bifurcating channels increases blood adsorption device efficiency. To test the potential effectiveness of the devices for LPS removal, a model system is utilized in which biotinylated-LPS doped blood is flowed through streptavidin coated channels and the effluent concentration measured with enzyme linked immunosorbent assay (ELISA).

4.3 Materials and Methods

To test the performance of different geometries of blood perfusion microfluidic devices in potential sepsis treatment applications, a rapid prototyping approach for manufacture of high-aspect ratio devices was developed. The result of this process is a polycarbonate “lamina” with high aspect ratio channels with either 125 μm or 250 μm channel width. Channel geometry was either 60 mm long straight channels, or fifteen 4

mm long channels offset to create bifurcations. As described in detail below, LPS clearance was assessed by coating the lamina with streptavidin, assembling the lamina into a housing and flowing blood with biotinylated-LPS through the device. The effluent was collected and analyzed by ELISA to determine the effectiveness of each configuration.

4.3.1. Lamina fabrication

Lamina were fabricated using a multistep embossing approach involving laser patterned polyetherimide (PEI) masters to hot emboss the polycarbonate (PC) lamina. Figure 4.1 outlines the process used to create the lamina. Embossing was done with a Jenoptic HEX 01 hot embossing tool (Jenoptic AG, Germany) and laser patterning was done with an ESI 5330 UV laser (Electro Scientific Industries, Inc., USA). AutoCAD was used to draw all device geometries for laser patterning. Fabrication parameters are outlined in Table 4.1. Slide 40112N Silicone mold release aerosol spray (McMaster-Carr, Santa Fe Springs, CA) was lightly applied to the pieces prior to each embossing step.

Table 4.1. Device fabrication parameters

Laser Parameters:		PEI Master	
Velocity	(mm/s)	100	
Frequency	(kHz)	30	
Laser Power	(W)	2.5	
Repetitions	(Passes)	4 x 11	
Embossing Parameters:		PEI Master	PC Lamina
Emboss Temp.	(°C)	220	160
Emboss Force	(N)	50000	4000
Hold Time	(min)	60	70
Removal Temp.	(°C)	20	35

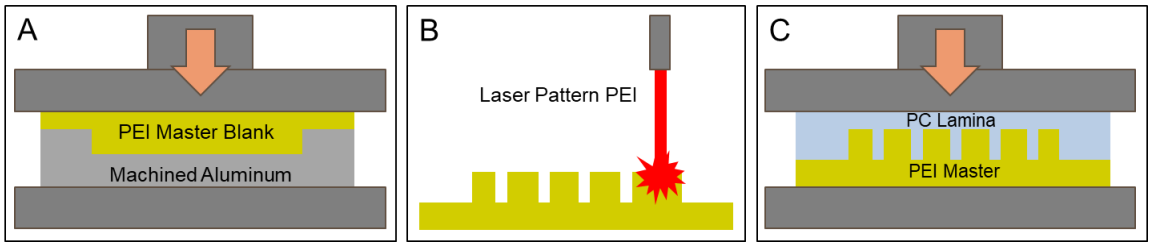

Figure 4.1. Process for creating a microfluidic lamina*. A) A piece of PEI is hot embossed against an aluminum block with a recessed area milled out that defines the outer boundaries of the device. B) The raised feature on the PEI "blank" is laser patterned with the desired channel configuration. C) PC is embossed with the finished PEI master forming a PC lamina with microchannels. The material removed by the laser machining forms the walls and the remaining PEI forms the channels in the PC.*

The process flow for creating a lamina was as follows: First, a milled aluminum block was used to create a raised feature by embossing PEI into a rectangle with dimensions 60L x 14.5W x 0.5D mm and triangular header regions at each end. This created a blank PEI master to be patterned with different channel geometries. Next, the laser tool was precisely aligned with the raised portion of the PEI master plate and the desired channel pattern was laser machined into the PEI master. The plate was then sonicated in 1% Alconox detergent for 2 hours to remove the laser soot from the surface and grooves. These cuts formed the channel walls of the finished PC lamina after embossing. The PEI master was embossed with a polycarbonate substrate to form a lamina. Typically, a PEI master could be used to emboss several polycarbonate laminae before breakage occurred. After a lamina was imprinted it was sanded with a rotary sanding wheel with 340 and then 600 grit wet sandpaper to polish the devices flat. This

step brought the tips of the channel walls perfectly flush with the outer edge of the device and ensured the entire device had a smooth top surface for creating a leak-proof seal.

4.3.2. Lamina cleaning and coating

Each lamina was first sonicated in a 1% Alconox detergent solution for 60 minutes to remove excess release agent and debris. Then the lamina was sonicated in 70% ethanol immediately prior to streptavidin coating. To coat the lamina, first a few drops of 70% ethanol were run down the length of the channels and wicked away from the header holes. This process wetted the device and lowered the surface tension, preventing air bubbles from being trapped in the channels after the streptavidin was applied. As soon as the ethanol was wicked away, but with the surface still wetted, 0.5 mL of 1 mg/mL streptavidin (VWR International LLC., USA) was pipetted over the channel region of each lamina and spread evenly with the pipette tip. The streptavidin was allowed to absorb to the channels for 1 hour, after which it was rinsed with ultra-pure water 4 times and the lamina edges dried with a Kimwipe. Two control experiments were conducted with F108 coated lamina. For these experiments, a 1% solution of Pluronic F108 (Sigma-Aldrich Inc., USA) was applied in the same manner as the streptavidin coating.

4.3.3. Housing fabrication and assembly

The assembled device seen in Figure 4.2 consisted of two housing plates which sandwiched two PDMS gaskets against the lamina in the middle. The housing plates were machined out of 3/4” polymethyl methacrylate acrylic sheets with threaded fluid feed holes for tubing connections and twelve 1/4” holes for bolting the device together.

Stainless steel nuts and bolts with washers on both sides were threaded and tightened to 80 cNm with a torque screwdriver. The PDMS gaskets were laser cut to have the same bolt pattern and fluid feed holes as the housing and lamina. When the device was assembled, the fluid was fed from the back side of the lamina through fluid feed holes. This was done to prevent gasket collapse in the header region, which happened when fluid was fed directly into the header region from the patterned side.

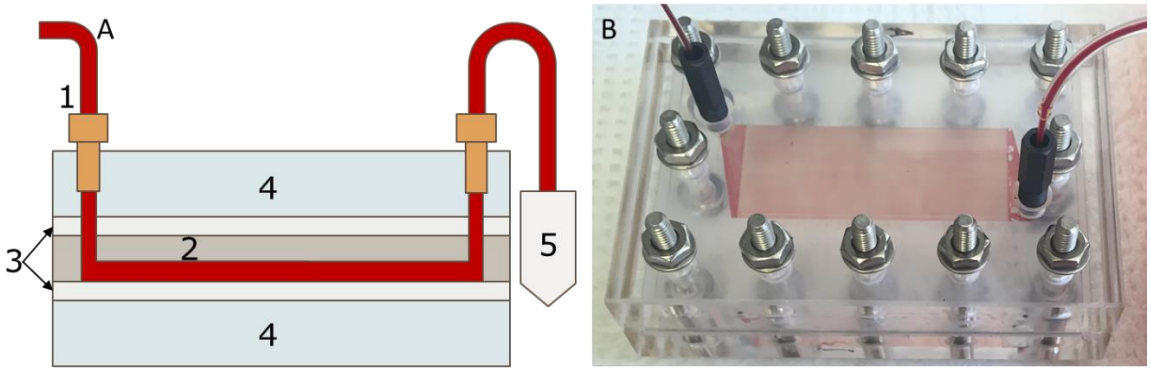

Figure 4.2. Schematic view and prototype of device *A) Schematic view of the assembled device. (1) The blood is fed from the syringe through threaded fittings in the housing. 2) The polycarbonate lamina has the channels facing downward. Blood is fed through feed holes in the back of the lamina to prevent gasket sagging in the header region. 3) PDMS top and bottom gaskets prevent leaking from the channels and the feed hole. 4) The acrylic housing applies even pressure across the lamina. 5) The blood outlet is the same design as the inlet, and blood effluent is collected into Eppendorf tubes. B) Picture of assembled device with blood flowing through an embossed lamina. The housing is compressed together with 12 bolts tightened with a torque screwdriver to 80 cNm, making a leak-proof seal without pressing the gasket into the channels.*

4.3.4. Blood preparation

Blood was collected from healthy donors via venipuncture into 3.2% equivalent sodium citrate vacuum tubes (BD Vacutainer), refrigerated, and used within 7 days of collection. Prior to each experiment, blood was allowed to come to room temperature and was centrifuged at 1400 g for 10 minutes and the plasma and buffy coat discarded. The blood was then resuspended in 1x sterile PBS pH 7.2. This process was repeated to wash the cells, and the final hematocrit adjusted to 40% with PBS. For each experiment, 5 mL of washed blood was prepared. The blood was then doped with 7.5 µL of 330 µg / mL LPS-Biotin (InvivoGen, USA) that had been vortexed for 1 minute. LPS-doped blood was then loaded into a 5 mL syringe, which had been assembled to contain a small stir bar; this stir bar was used for manual mixing during experiments, as described in detail below.

4.3.5. Device operation

Prior to each experimental run, 10 mL of sterile 1x PBS was primed through the device using a gentle manual pulsing motion to clear small air bubbles that would otherwise remain stuck in the channels. After the device was primed, a starting sample of the blood was collected and the PBS syringe was disconnected from the inlet tubing. Then the blood syringe was connected and loaded into the pump, taking special care not to introduce any bubbles into the line during the syringe transition. Immediately after the syringe was seated in the pump, the small stir bar in the syringe was externally manipulated with a magnet back and forth down the length of the syringe to thoroughly mix the blood. This process was continued throughout each experiment to keep the blood

entering the device mixed. Blood was pumped at 1 mL/min for a residence time of 30 s. One mL of blood was flowed through the device before sample collection began to ensure negligible effects of dilution with the priming PBS. Two samples were collected for 30 s intervals (0.5 mL each), after which the syringe pump was stopped, and an ending sample of the syringe was taken. Each experiment consisted of a pre-run syringe sample, a post-run syringe sample, and two samples of the device effluent.

4.3.6. ELISA procedure

Blood samples were spun down at 1,000 g for 15 minutes and analyzed for LPS-biotin concentration using the CEB526Ge LPS ELISA from Cloud-Clone Corp. (Lifome Biolabs, USA). The protocol provided by the manufacturer was modified for detection of LPS-Biotin as follows. This immunoassay has an antibody specific to LPS bound to a microplate. If used in the prescribed fashion for detection of non-biotinylated LPS, the LPS competes for binding sites with the LPS-biotin included in the kit's "reagent A", which is added in the first step. Completion of the standard protocol results in an inversely proportional response to non-biotinylated (native) LPS. Since the goal of this experiment was detection of LPS-biotin, the first step of adding the kit's "reagent A" was eliminated and instead 100 µL of our sample was added. All remaining steps were followed per the kit instructions. This method was verified with a calibration curve of LPS-Biotin in washed blood, prepared the same way as the blood for experiments. Results were immediately read on a BioTek Synergy 2 (BioTek Instruments, Inc., USA) plate reader at A_{450} per the kit recommendation. Starting and ending syringe

concentrations were averaged, the two device effluent concentrations were averaged, and the overall percent removal was calculated for each run as follows:

$$\%\ Removal\ = 100 * \left(1 - \frac{Effluent\ conc.}{Syringe\ conc.}\right).$$

4.3.7. Statistics

Statistical analysis was carried out by 2-way ANOVA using Statgraphics software (Statpoint Technologies, Inc., The Plains, VA) with channel width and channel geometry (straight or bifurcated) as the independent variables. Significance between device geometries was determined with Fisher's least significant differences method to the 95% confidence level. Endotoxin removal results are presented as the mean ± SEM.

4.4 Results

4.4.1. Lamina fabrication

Laminae were fabricated with up to a 4:1 channel height to width ratio using the double hot embossing with laser machining method described depicted in figure 4.3. Channel width was either 125 μm or 250 μm and channel height was 500 μm. The channel walls are nearly vertical with this method and measure approximately 80 μm wide at half-height. The bottoms of the channels appear nearly flat making each channel a rectangular slit. Even after thorough cleaning some soot from the laser patterning can be seen on the tips of the channels on the embossed PC lamina. This is at the very deepest point of the PEI master and is embedded in the PC after embossing. After embossing with the same PEI master several times the soot diminishes to nearly undetectable levels.

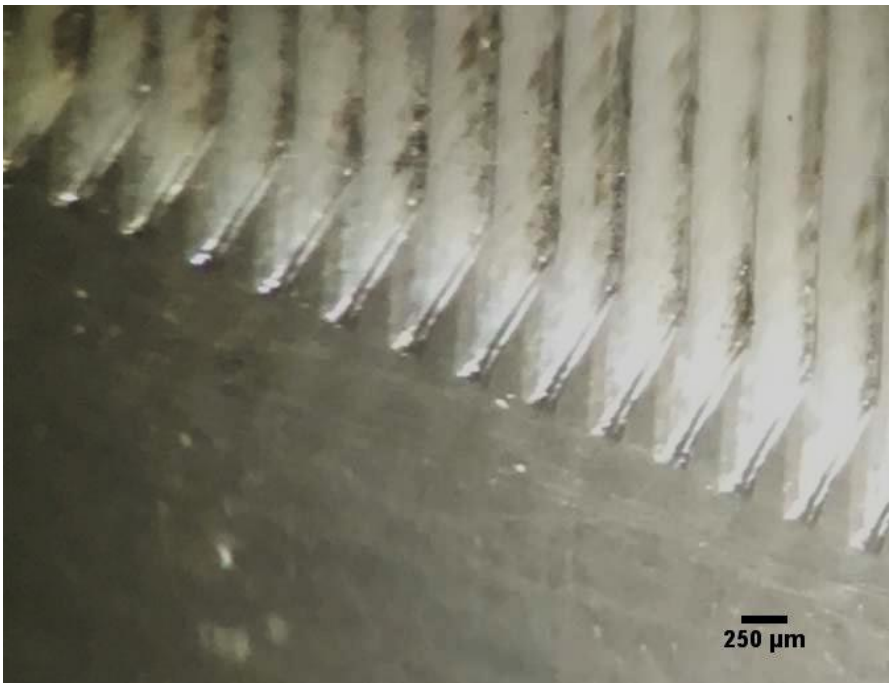

Figure 4.3. A lamina with 250 µm wide channels under a dissection microscope. *Image taken looking down the length of the channels from the header region. The channels have nearly vertical sidewalls and are rectangular. Some soot from the laser process that is transferred from the PEI master is visible on the tips of the PC lamina after embossing.*

4.4.2. ELISA calibration curve

Due to modification of the ELISA protocol to measure LPS-biotin instead of non-biotinylated LPS, a new calibration curve was generated for the method. Figure 4.4 gives the calibration curve for LPS-biotin in PBS washed blood. The calibration curve is in the linear range for the absorbance values measured in the LPS-biotin removal experiments. The measured average of the initial syringe concentration was 25% lower than the average syringe concentration at the end of each experiment. To account for the discrepancy in measured LPS, the beginning and end syringe LPS concentration was

averaged, and two experimental time points of the device effluent were also averaged. The fractional removal was calculated on a per experiment basis.

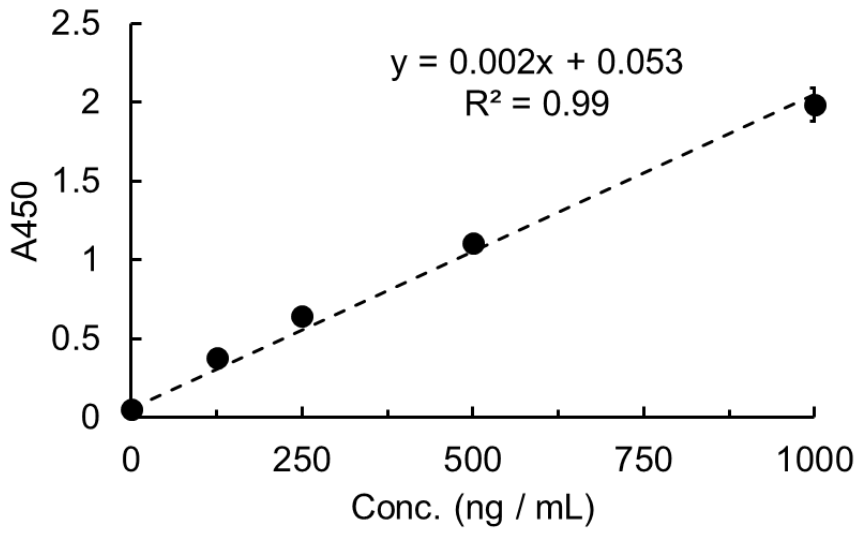

Figure 4.4. Calibration curve for LPS-biotin diluted into PBS using the modified ELISA protocol. *Absorbance exhibits linear response in the concentration range of interest.*

4.4.3. LPS-biotin removal

Figure 4.5 shows the percent removal for each device geometry (n = 3). Significantly higher removal ($p < 0.05$) was seen in the narrower 125 µm wide channel devices. The highest removal at 80 ± 13% was seen with the 125 µm wide straight channel device. The lowest removal, 49 ± 10%, was seen in the 250 µm wide straight channel device. There was no significant difference ($p > 0.05$) between straight and bifurcated channels. Control experiments were conducted using 125 µm wide channels

coated with Pluronic F108 and showed a reduction in LPS-biotin of 15% and 22% for straight and bifurcated channels respectively.

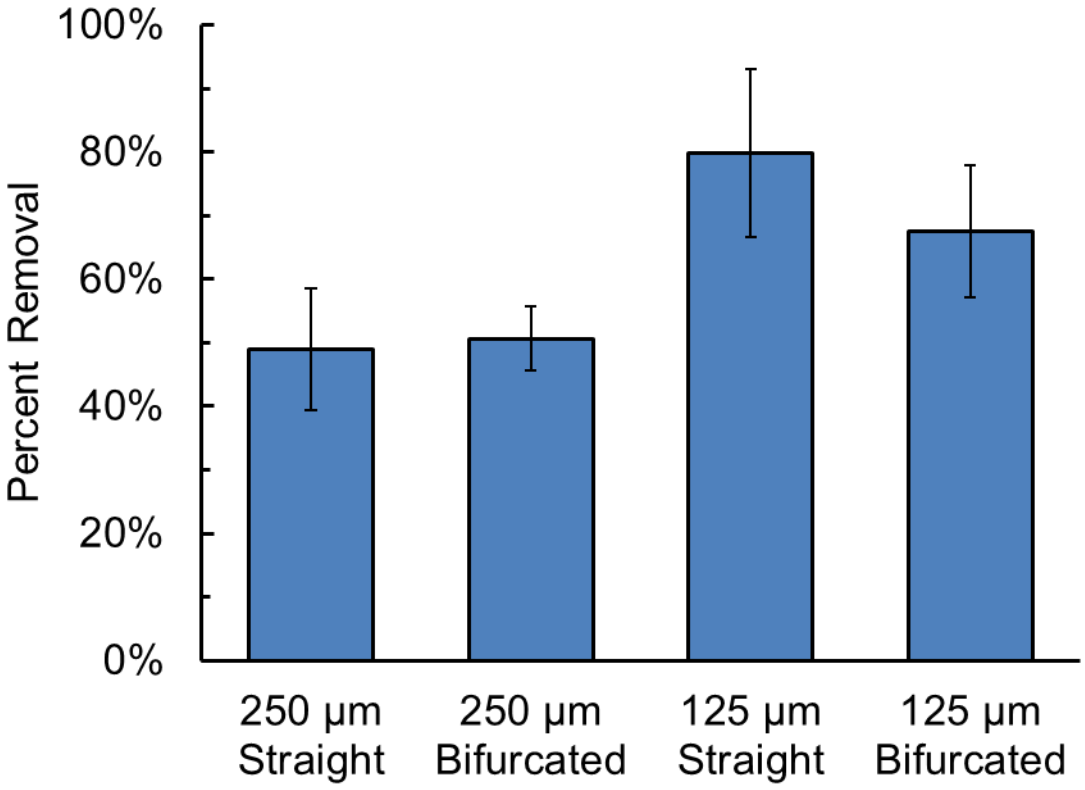

Figure 4.5. Percent LPS-biotin removal for the tested geometries*. A significant difference in removal was seen between the 125 µm and 250 µm wide channels ($p < 0.05$).*

4.5 Discussion

The original intent of this study was to determine if the induced mixing by bifurcating flow would increase the efficiency of LPS capture in microfluidic devices. LPS aggregates can range in size from 10 to > 200 nm in aqueous solutions and therefore

would have very low self-diffusion rates, making it take too long for an aggregate to migrate across the channel to the wall. We hypothesized that by bifurcating the flow, LPS locked up in the middle of the channel would be placed in proximity of the wall multiple times while it traversed the length of the device. Any beneficial effect of capture caused by aiding lateral movement of LPS should be more pronounced as the channel dimensions approach the mesoscale and the diffusion path length to the channel walls increases, hence two channel widths (250 and 500 μm) were tested to determine if there was a greater benefit at larger dimensions. It was also hypothesized that disruption of the established blood flow would enhance capture since after each bifurcation the red blood cells would be disrupted from their usual flow streamlines, which concentrate at approximately 0.5 to 0.6 the distance from the channel center [27]. After disruption at the bifurcation, the blood cells would laterally migrate toward the new channel center, effectively pushing smaller particles such as the endotoxin aggregates toward the channel walls [186].

The results of this study indicate that bifurcating the flow under the conditions tested had no significant effect on LPS-biotin capture. One possible explanation for this result is that the distance between bifurcations was insufficient to allow complete flow margination and migration of the LPS-biotin to the channel walls. If this is the case, longer bifurcation distances might result in a beneficial effect on LPS-biotin binding. In addition to relocalization of the LPS-biotin near the walls, another factor that may mask the beneficial effects of bifurcations is the enhanced particle diffusivity in high hematocrit flows [182, 185, 195]. If we consider a 100 nm endotoxin aggregate in water, the diffusivity would be $\sim 5*10^{-12}$ cm^2/s. These particles would have a characteristic

diffusion time ($t_D=l^2/D$) from the center of a 250 μm wide channel of 52 minutes. Since the residence time is approximately 30 seconds there appears to be enhanced particle motion under these conditions.

High hematocrit blood flow is an extremely complex system that has been widely studied for many years. Many physical and mathematical models have arisen to give perspective into this dynamic, multiphase system, and many theories have been developed to explain the motion of blood cells and other blood constituents [196, 197]. While many have tried to simplify this system for easier study, certain inherent properties are lost when only dilute multiphase flow or rigid particles are studied [183, 184]. Two of the earliest observations that paved the way for more complex hemodynamic models are the Segré–Silberberg effect for describing lateral migration particles away from walls, and the Fåhræus–Lindqvist effect to describe the non-Newtonian nature of flowing blood due to the lateral migration of red cells toward the middle of channels resulting in an increased effective viscosity [198, 199]. This shear-dependent lateral movement of high hematocrit blood and formation of a cell-free layer in microchannels results in many unique properties. These properties may help explain why adsorption devices such as the one in the present investigation may not benefit from induced mixing by bifurcating flows, especially when wall interaction with small particles like LPS is preferred.

While LPS can be considered a macromolecule with a molar mass of 10-20 kDa, it is typically found as aggregates with different characteristics dependent on factors such as bacterial origin, concentration, and containing media, among others [200, 201]. Of primary concern to this research is the size and physical conformation of LPS vesicles or aggregates, which can vary based on the above factors [200-202]. Santos et al. used light

scattering spectroscopy to determine the average diameter of LPS from *E. coli* O26:B6 to be 190 nm when the concentration of LPS was ≥ 40 μg/mL [202]. Risco and Pinto da Silva used freeze-fracture to determine the diameter of *E. coli* O111:B4 LPS aggregates (the same serotype used in this study) to be 10-80 nm in aqueous solutions or ≥ 200 nm in serum and up to micrometers in length [201]. Ryder et al. used dynamic light scattering to determine the size of *P. aeruginosa* LPS in PBS to have a bimodal distribution with an average size of of 89 nm for the lower mode and 408 nm for the upper mode [203]. In any case we can consider LPS to be a deformable particle with highly variable size, especially under laminar flow conditions in PBS washed blood.

To gain perspective on the behavior of LPS in microchannels we can look at other blood components that have similar characteristics. Platelets are a well-studied deformable particle around 2 μm in diameter, present in moderately high concentrations in human blood [204, 205]. Of particular interest is the way in which high-hematocrit red blood cells and platelets interact under laminar flow conditions in microchannels. Under laminar flow in microchannels with a sufficiently high flow rate, flow margination takes place and red blood cells migrate toward the center of the channel, pushing platelets and white blood cells toward the walls [186, 206, 207]. This effect appears to be predominately a consequence of the high concentration of deformable red cells and their propensity toward aggregating in the middle portions of microchannels or microtubules due to their lateral motion under these flow conditions [184, 186, 195, 206]. At hematocrits of 40%, platelet concentration at the wall can be from 5 times to an order of magnitude higher, increasing with shear rate (240 s^{-1} – 1200 s^{-1}) as demonstrated by Aarts et al. [186]. While the shear rate under the flow conditions in this study is up to an order

of magnitude lower than the range tested, it is likely that the platelet concentration near the wall will be several times higher than that near the channel center with most of the platelets occupying the third of the channel closest to the walls. If so, we speculate that LPS will migrate toward the outer walls in a similar pattern to platelets and white blood cells, as red cells migrate inward. This places LPS near the wall, in the ideal location for surface adsorption when equilibrium positions are reached. Red blood cells rapidly migrate toward equilibrium positions at approximately 0.5 to 0.6 of the centerline distances, which occurs within the first few millimeters of downstream length while smaller particles such as LPS take much longer to migrate outward [27]. Bifurcations could disrupt the process in which red cell migration potentially "pushes" LPS aggregates toward the walls resulting in decreased LPS adsorption. If this is the case, bifurcation lengths that are too short may disrupt this process keeping endotoxin more evenly mixed across the channel width.

Another consequence of high hematocrit blood flow is induced mixing due to the motion and migration of red blood cells. This results in much higher diffusivity for particles and solutes [182, 185, 195]. Particle diffusivity in blood also appears to increase with increasing shear rate and hematocrit [182, 185]. Saadatmand et al. found the dispersion of 1 μm fluorescent tracer particles in blood to be approximately 5 times higher at 20% hematocrit than at 0% [182]. They also reported an increase in dispersion with flow rate in 10% hematocrit blood in a 50 μm capillary tube to nearly double with every doubling of flow rate [182]. Cha and Beissinger tested multiple hematocrits against shear rate and found a similar increased dispersion when hematocrit was 45%, which also happened to be the hematocrit at which diffusivity was maximal [185]. Vahidkhah et al.

modeled the interaction of a single cell and platelet and found that under shear rates of 100-1000 s^{-1} the diffusion of platelets would be enhanced by 2 to 3 orders of magnitude over Brownian motion alone [195]. This phenomena appears to be a function of the deformability and migration of the red blood cells since flows with rigid spheres or tracer particles do not seem to have the same level of enhanced diffusivity [183, 208]. Taking into consideration both the shear induced migration and enhanced diffusivity of high hematocrit blood flow in microchannels, one can see how an absorption device, especially at the ~100 μm scale, could perform well for adsorption of LPS. In addition, reducing the channel width with the same flow rate not only decreases the diffusion distance, but increases the enhanced particle diffusivity as well.

4.6 Conclusion

Here we have demonstrated microscale bifurcations with the intent of increasing absorption efficiency in a model endotoxin adsorption device. We saw no effect of bifurcations under the conditions tested, likely due to the enhanced diffusivity and localization of LPS near the walls in high-hematocrit blood flow. Although we saw no significant increase in absorption with bifurcations in the 125 or 250 μm wide channels tested, at larger mesofluidic scales they may provide a beneficial effect. While future work could examine different bifurcation geometry, this work indicates that reducing channel dimensions can increase endotoxin adsorption device efficiency.

4.7 Acknowledgements

We would like to thank the volunteer blood donors for providing blood samples for this study, as well as the Oregon State University Student Health Center for performing blood collections. This project has been made possible with support of the Oregon State University Venture Development Fund (http://campaignforosu.org/uvdf/), as well as funding from the National Science Foundation (award #1414400).

Chapter 5: Conclusion and Future Directions

The goals of this work were to further the development of frozen blood storage through the development of faster cryoprotectant removal techniques and to use microfluidic blood processing technology for the treatment of sepsis. Significant strides were made on both of these topics. The 2-parameter model for cell membrane transport was refined to include a concentration dependent permeability parameter for glycerol, allowing for more accurate mathematical modeling of rapid deglycerolization procedures. Deglycerolization procedures were developed using this new model and then were tested, revealing previously unanticipated variability in permeability within the cell population and within individual donors. This discovery opens the door to further research which will continue toward the goal of ultra-rapid deglycerolization. On the topic of microfluidic blood processing, a new rapid prototyping method was conceived to create high aspect ratio microchannels. This method was then used to create a device to test the impact of microchannel width and bifurcations on removal of biotinylated lipopolysaccharide as an analog for endotoxin. It was determined that though bifurcations showed no effect on removal of biotinylated lipopolysaccharide, microchannel width was statistically significant. This data can be used to further refine the microfluidic device for optimal removal of endotoxin and treatment of sepsis.

5.1. Technologies for Cryoprotectant Removal from Frozen Blood

The 2-parameter model for modeling cell membrane transport has been one of the most useful tools in cryobiology since the first half of the 20th century [50, 51]. Although a relatively simple model compared to some of the other modeling approaches used in

cryobiology, it fits experimental conditions and predicts cell behavior under many experimental conditions [49]. Although this model has been used for making experimental predictions for red blood cell deglycerolization in the past, here we identified an important shortcoming of the model for predicting cell volume excursions when glycerol content is as high as 40%. The over 5 times higher permeability seen at low glycerol concentration compared with this upper limit experienced by cells that have been glycerolized, frozen, and thawed, appears to be a result of the method by which glycerol crosses the cell membrane. In Chapter 2 the in-depth analysis of water and glycerol transport proteins revealed the importance of AQP3 as the primary glycerol transporter in human erythrocytes. Although the exact physical mechanism this transporter uses to move glycerol across the membrane is not fully understood, it has been speculated to be a facilitated diffusion process in which the protein must bind a single glycerol molecule and transport it across the membrane. Processes such as these can become saturated which appears to be why there is a dramatic drop in the permeability parameter at high glycerol concentrations.

In addition to the concentration dependence to glycerol transport in RBCs, this work aimed to be a starting dialog about variability in transport parameters. Variability in the permeability parameter for membrane transport has been known for some time but has not been incorporated into mathematical models for cryoprotectant loading or unloading [102, 171]. In applications where long cryoprotectant loading and unloading times are acceptable, permeability variability can be avoided by simply extending the time for these processes. However, when attempting to minimize cryoprotectant removal times as in ultra-rapid deglycerolization of RBCs, discrepancies between the

permeabilities of cells for individual donors or a permeability distribution within the cell population becomes significant and an obstacle that must be overcome. The testing of different deglycerolization procedures in Chapter 3 revealed a much broader distribution of the glycerol permeability for RBCs than we had anticipated. Even though we had applied our concentration dependent model and accounted for a permeability range within the cell population of ±50%, hemolysis of cells during the deglycerolization experiments was much higher than anticipated. While Chapter 3 addressed the physiological processes that may be causing such a reduction in permeability, the distribution of permeability values, and especially the lower permeability values, is a major barrier to the development of ultra-rapid deglycerolization.

Although glycerol transport appears to be very slow in a small subset of the cell population, it has been hypothesized that these cells are the oldest cells and therefore are very near eryptosis [14]. When red blood cells near their end of life they make changes that result in reduced functionality including loss of hemoglobin, loss of cell membrane, and oxidation of cell membrane proteins [141, 142, 145, 149]. If these cells are disappearing during standard deglycerolization procedures, they likely have undergone functional changes that gives them a far reduced glycerol permeability as discussed in Chapter 3. Upon exposure to deglycerolization solutions, rapid water influx would cause these cells to swell and lyse. Because these cells have reduced functionality and are close to being removed from circulation anyway, it may be beneficial that they are removed from the blood that is about to be transfused and may result in a higher quality blood product for the patient. A possible future direction for this work would be to provide direct evidence that the oldest cells or functionally oldest cells are the cells that have

reduced glycerol permeability. Another method to shorten glycerol transport time is to increase temperature, which speeds up the transport process. Red blood cells can withstand temperatures up to approximately 47 °C, at which spectrin denatures and the membrane loses integrity [209, 210]. At these temperatures glycerol transport is much faster than at room temperature. This is discussed in further detail in Appendix A where initial deglycerolization experiments at elevated temperature achieved nearly double the glycerol removal rate. If deglycerolization can be accelerated and procedures designed that can carry out the process in several minutes, a continuous deglycerolization device that allows the use of frozen-thawed blood on demand may still be a possibility.

5.2. Blood Processing Technologies for the Treatment of Sepsis

Since the beginning of research in the use of microfluidic devices for blood treatment, the prospect of harnessing the unique characteristics of blood flow in microchannels has promised advanced treatment platforms with improved safety and efficiency. The application of microfluidic technology to blood absorption devices offers enhanced safety through reduced treatment volumes and greater efficiency through enhanced mixing and margination of blood constituents [27, 29, 181, 182]. In Chapter 5, we attempted to further increase blood adsorption device efficiency by bifurcating microchannels to induce mixing. To do this we developed a new rapid prototyping approach for fabricating high aspect ratio channels. This approach allowed for a height to width aspect ratio to nearly 4:1, double that of similar hot embossing rapid prototyping approaches [187, 193, 194]. We also developed a unique model system for testing the adsorption of endotoxin. In this system, streptavidin coated channels were used to absorb

biotinylated endotoxin. The streptavidin-biotin interaction is one of the strongest non-covalent bonds in nature [211]. This system allowed for direct and simple characterization of the channel geometry without the additional complication of variables such as coating binding affinity to endotoxin or channel coverage of more complex coatings. Testing of these devices showed there was a significant effect on removal for different widths of channels, with the smaller 125 μm wide channels showing single pass clearance upward of 80% with a relatively short residence time of 30 s. However, bifurcations had no significant effect on removal of biotinylated lipopolysaccharide for any of the channel geometries tested.

When blood flow in a microchannel is disrupted it takes more time for the lateral migration of RBCs to push smaller particles like platelets or LPS toward the channel walls [27, 29, 186, 206, 207]. While the 4 mm lengths between bifurcations in this study were intended to allow adequate time for the equilibrium positions of the particles to be reached, there may be a longer length that allows the LPS caught in the middle of the flow to redistribute after the LPS close to the channel walls has been depleted. Additionally, it has been shown that the lateral migration rate and the effective diffusivity of the particles both increase with increasing shear rate. Continuation of this work should investigate bifurcation distance and the trade-offs between higher shear rates and reduction in residence time at higher flow rates.

Appendix A: Temperature Effects on Blood Deglycerolization

This section provides detail on deglycerolizing blood at elevated temperatures which we believe is a promising future direction for the work discussed in Chapters 2 and 3. Temperature effects for water and glycerol transport are well documented for human erythrocytes and Chapter 2 provides a review of the literature on the subject. At room temperature, water transport can already be considered near instantaneous, so increasing the glycerol transport rate by elevating temperatures is the primary concern for continuation of this work.

Transport kinetics follow the Arrhenius Law. As such, finding the permeability parameters at various temperatures allows one to determine the Arrhenius activation energy (E_a) for transport. In Section 2.5.2. we discuss the activation energy for glycerol transport in human erythrocytes. Values under normal conditions range from 15 kJ/mol, a fairly low temperature dependence, to 40 kJ/mol, a moderately high temperature dependence [38, 48, 59, 88].

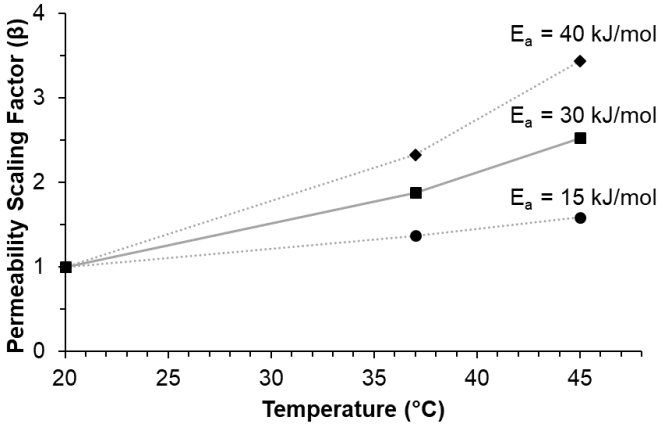

Figure A.1. Temperature effects on scaling of the glycerol permeability parameter. *β is defined as a scaling factor here as in Chapter 3, where $P_s A/W_{iso} = \beta(a_s/(b_s M + 1)$.*

The scaling is shown for the two extremes of the published activation energies (E_a) and the average of the two. The temperatures plotted are room temperature (20 °C), human body temperature (37 °C), and just below red blood cell spectrin denaturation temperature (45 °C).

Figure A.1 shows how the two activation energy extremes from the literature would scale the permeability parameter. At 37 °C, the temperature of the human body, a safe elevated deglycerolization temperature for human red blood cells, the permeability parameter is 1.9 times its normal speed when E_a = 30 kJ/mol, the average of the two E_a extremes. 45 °C is the maximum temperature to which erythrocytes should be heated, as spectrin denaturation and loss of membrane structural integrity occurs around 47 °C [209, 210]. We confirmed that 45 °C was a safe upper limit by subjecting frozen-thawed cells to elevated temperatures for 3 minutes. 45 °C was the highest temperature at which there was no additional hemolysis. At 45 °C the average E_a gives an increase in permeability of 2.5 times that of room temperature.

In order to test the effect of elevated temperatures on deglycerolization time, a series of experiments were carried out using the same three-step systematic investigation as described by Lusianti et al., but with some alterations [19]. Frozen blood aliquots were thawed at the specified elevated temperatures for 3 minutes to allow for equilibration before the experiments began. Then the cells were diluted with either a two, four, or tenfold dilution of 12% saline. Additionally, the deglycerolization solutions used in each step were stored at elevated temperatures. The flask where the deglycerolization took place was placed in an insulated beaker and water warmed to the specified investigative

temperature was placed in the beaker to maintain the temperature of the flask. With this method we measured less than a 1 °C difference from the start to end of a deglycerolization experiment.

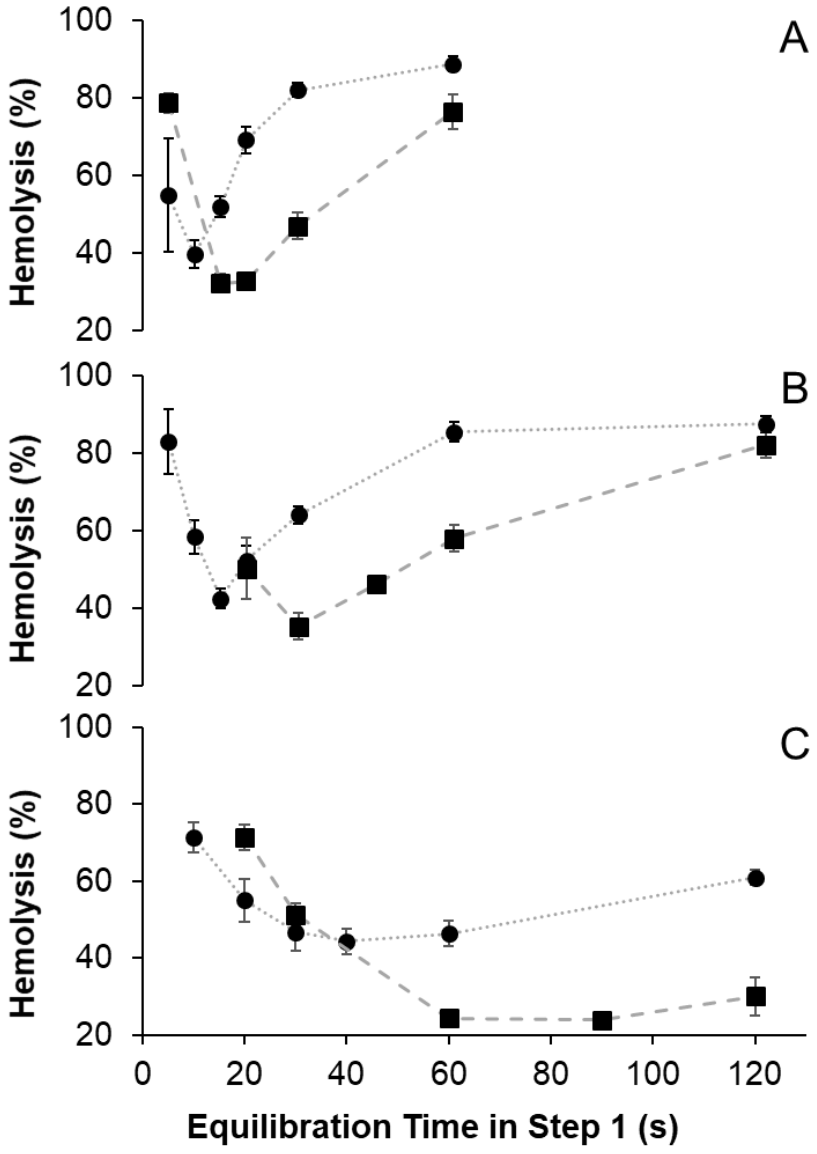

Figure A.2. Effect of equilibration time in the first step of a three-step deglycerolization procedure on hemolysis at room temperature of 20-22 °C (squares) vs. 37 °C (dots).

Either a tenfold (A), fourfold (B) or twofold (C) dilution was used. The procedure was carried out as described in Lusianti et al. at elevated temperature, and the room temperature data is the same data from Figure 6 of that publication [19]. Each time tested is the mean of a single experiment for three separate donors ±SEM.

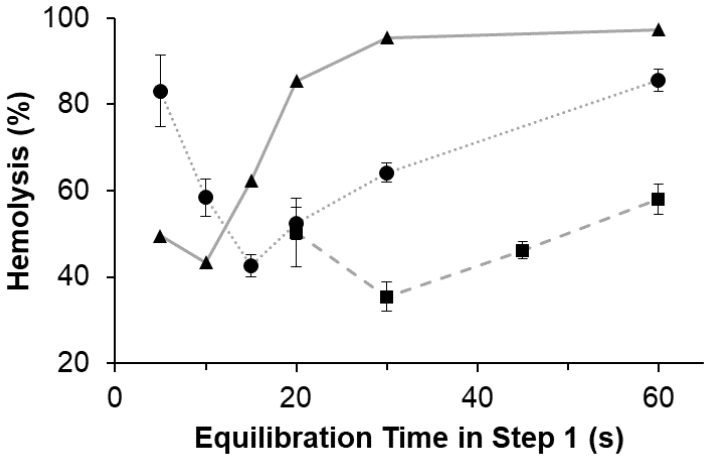

Figure A.3. Effect of equilibration time at 45 °C for a single donor (triangles) on hemolysis. *The data from Figure A.2 at 21 °C (squares) and 37 °C (dots) is shown for comparison purposes.*

Figure A.2 shows the room temperature (21–22 °C) deglycerolization data presented in Figure 6 of Lusianti et al. compared to the same experiments carried out here at 37 °C [19]. It should be noted that we were unable to achieve the low hemolysis levels found in the work of Lusianti et al in any of our experiments even at room temperature. This is most likely due to the use of different blood donors, and therefore cells with different permeability to glycerol, as discussed in detail in Chapter 3. Although the hemolysis may be higher overall, the time at which the hemolysis value reaches the

lowest value is what is of significance for these experiments. The ratio of time for lowest hemolysis at room temperature compared to the time at 37 °C is 0.67 for the twofold and tenfold dilutions and 0.50 for the fourfold experiment. Additional times around the lowest values should be tested to find the true minimum, especially for the tenfold dilution at 37 °C where small timing changes result in large changes in hemolysis. Nevertheless, deglycerolization appears to be up to twice as fast under these conditions. An additional experiment was carried out at 45 °C with the results shown in figure A.3. Here the fourfold dilution, which had the best results in the previous experiments, was tested for a single donor. The other temperature data from figure A.2 panel B is shown for comparison purposes. Here the time at which hemolysis is lowest is a third of the deglycerolization time at room temperature indicating deglycerolization may be up to three times as fast at elevated temperatures.

While this is only preliminary data, the possibility of reducing deglycerolization times to a third of what we presented in this investigation may make a continuous deglycerolization device a possibility. In Chapter 3 we presented a procedure that met the AABB standard of sub-20% hemolysis with 18 minutes of total deglycerolization time. If this time scaling could be applied to those procedures, deglycerolization in as little as 6 minutes may be a possibility. This would be 39 minutes faster than the currently accepted procedure carried out in the ACP215. Additionally, 6 minutes is a more reasonable residence time for a continuous deglycerolization device which may make on-demand use of frozen blood a possibility.

Appendix B: Lessons Learned from the Design and Fabrication of the Microfluidic Sepsis Treatment Device

This section details the changes made to the design of the sepsis treatment device in an attempt to show a positive impact of channel bifurcations on capture of lipopolysaccharide from blood. Additionally, the fabrication processes used throughout this project are outlined here including the development of techniques used for rapid prototyping of high aspect ratio devices.

Header Design and Impact on Bifurcated Flow

The first issue observed when testing the device design was an issue with the flow distribution at the bifurcations, discovered by taking high speed video under a microscope of the device during operation. The problem arose from a net positive movement of cells at each bifurcation which appeared to have very little effect on redistributing the flow. Figure B.1 shows ideal operation of the bifurcations. However, it was seen that cells would move upward after each bifurcation causing very little disruption to the RBCs flow streamlines. To investigate why this flow distribution occurred, we conducted CFD modeling of our designs using COMSOL Multiphysics (COMSOL, Inc., Burlington, MA).

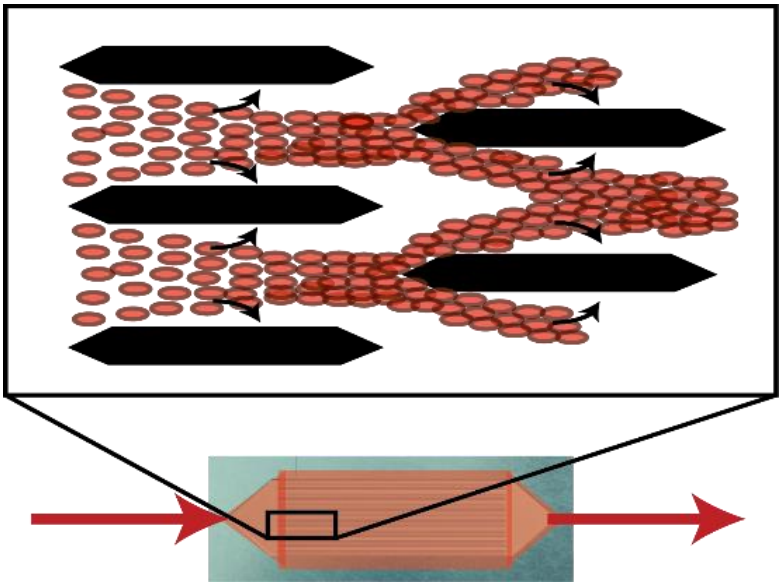

Figure B.1. Ideal operation of the bifurcations*. The blood flow is disrupted at each bifurcation after which it begins to laterally migrate pushing endotoxin, represented by the black arrows, toward the channel walls.*

Our COMSOL model was simplified to a system of water flowing under laminar flow conditions with a 1 minute residence time in each device we tested. We used a 2-D infinite plane geometry with directly imported models that were modified to show actual fabrication dimensions. The fabrication dimensions differed from the model due to over-etching during the photochemical machining process (photochemical machining is discussed in further detail below). This resulted in narrower wall width, larger channel width and a slightly larger gaps between bifurcations than on the original CAD model. After modeling several of our geometries what we found was that the asymmetrical "Z shaped" header shown in Figure B.2 was causing net positive movement in the y-direction of the cells from the inlet to the outlet. This is an issue distinct to the bifurcated

geometry since straight channels would not have these "short-circuit" paths at each bifurcation and therefore the Z-shape provides perfectly uniform pressure drop across the entire device due to the equal, but opposite design. Figures B.2, B.3, and B.4 show the CFD modeling for different header designs. The data displayed is velocity profiles taken at the entrance to the second set of bifurcations. For the most part the x component of the velocity in each channel is fairly uniform, however, the y component varies wildly, especially when considering the "Z-shaped" header in Figure B.2 compared to a symmetrical triangular shaped header as shown in Figure B.3.

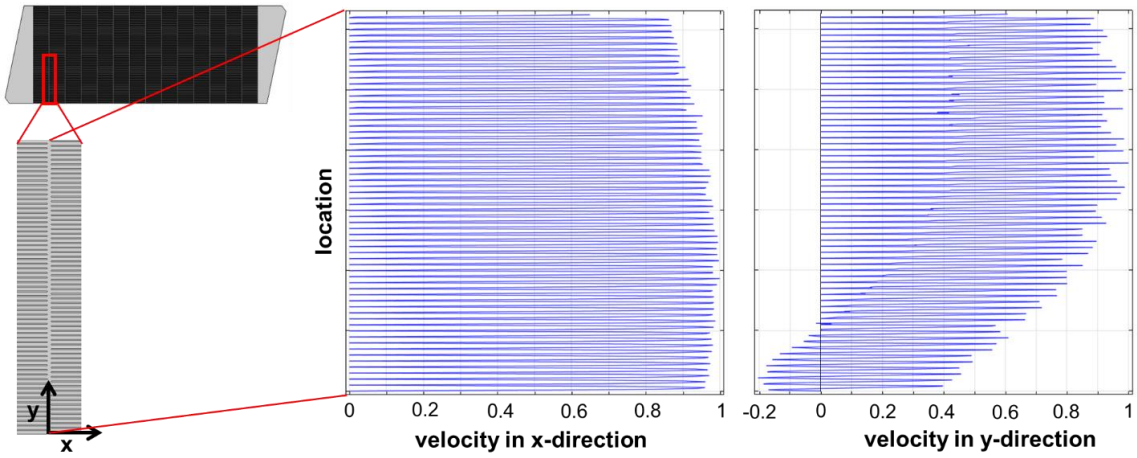

Figure B.2. Simulations of fluid flow at the first bifurcation for a lamina design with rhomboid "Z-shaped" headers*. The horizontal velocity (x-direction) is approximately the same in each microchannel. However, the vertical velocity (y-direction) shows that flow is not distributed evenly at the bifurcation; there is a net tendency for upward flow as expected based on the "short circuit" path between the inlet at the bottom left and the outlet at the top right.*

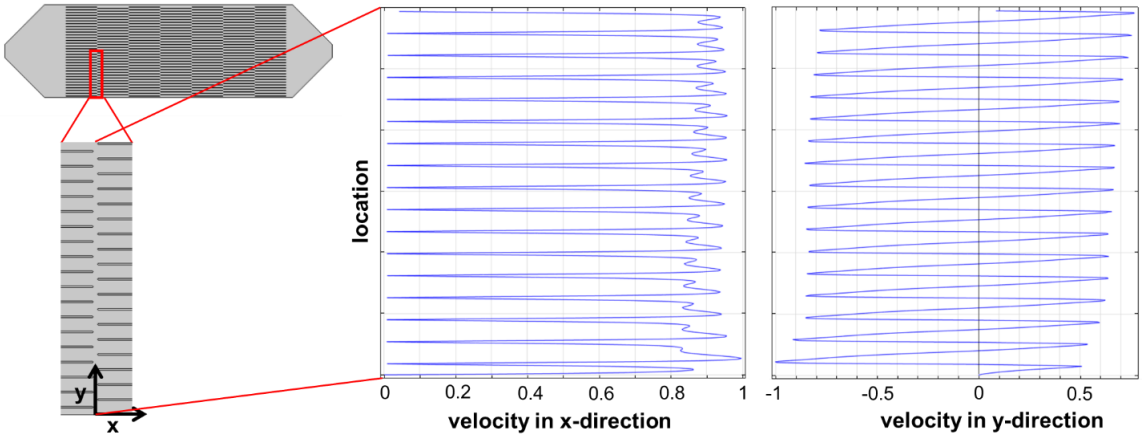

Figure B.3. Simulations of fluid flow at the first bifurcation for a simpler symmetrical triangular header design*. The horizontal velocity (x-direction) is approximately the same in each microchannel. The vertical velocity (y-direction) varies between positive and negative values, as expected for flow into the microchannels downstream of a bifurcation. Overall, there is slightly more downward flow than upward flow, which is a result of the spreading of flow from the centrally located inlet toward the channel walls.*

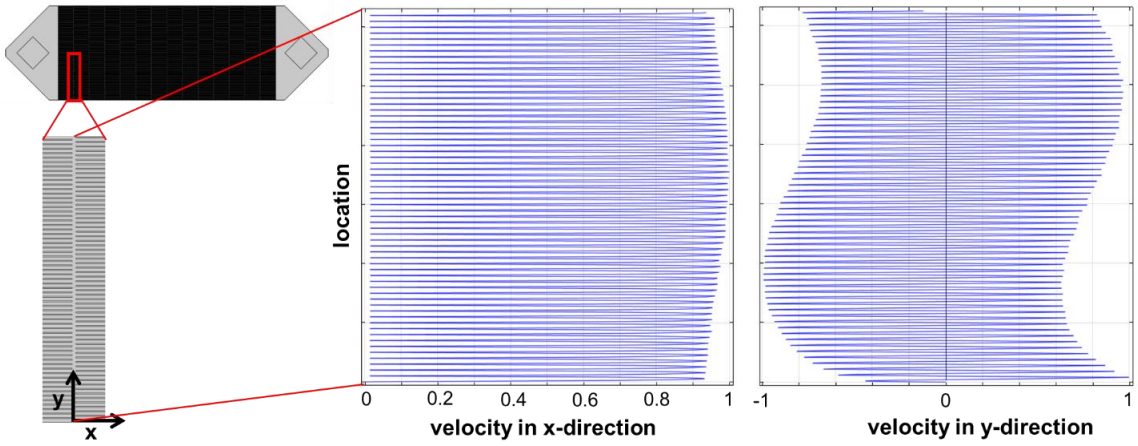

Figure B.4. Simulations of fluid flow at the first bifurcation for wider lamina with a subdivided header*. The diamond shaped posts in the header regions serve to better*

distribute flow across the device width and provide support for the PDMS gasket. The redesigned header results in more balanced flow at the bifurcations in wider devices without relying on extremely long headers.

Originally the "Z shape" design was selected for creation of wider devices with even flow distribution across all of the channels. Since this header design would not work with bifurcations, it was abandoned for the triangular header design seen in Figure B.3. If one were interested in making a wider device and still maintaining relatively even flow distribution across the channels without an extremely long header, one option is to use a diamond shape in the header region like that seen in Figure B.4. Functionally, this is like running two devices in parallel since the header region essentially forms two smaller triangular subheaders. Based on our previous experiences with air bubbles getting trapped when dividing flows, we chose the simpler header design with a narrower device like the one in Figure B.3 for further testing.

Microfluidic Device Architecture for High Aspect Ratio Channels

We expected devices with an improved header design to more uniformly distribute flow through the microchannel array. However, even with the improved header design, we were unable to detect a positive effect of bifurcations on particle removal. This continued failure to detect a positive effect of bifurcations led us to re-examine our original rationale for using bifurcations.

We had originally hypothesized that bifurcations would be beneficial due to their effect on RBCs, as discussed in detail in Chapter 4. In microchannels under laminar flow

conditions, RBCs experience shear-induced body forces that cause them to move away from the wall [27, 197, 206]. This lateral RBC movement pushes other blood constituents toward the wall into the margins of the flow [27, 206]. Bifurcations were expected to disrupt the equilibrium RBC location, resulting in lateral RBC movement to establish a new equilibrium state in the channels downstream of the bifurcation. Overall, the RBC movement caused by the bifurcations was expected to laterally mix the blood flowing through the device, enhancing delivery of particles (e.g., endotoxin) to the sidewalls seen in Figure B.5 panel A. In the previous low aspect ratio devices, the sidewalls make up a very small fraction of the surface area available for adsorption shown in Figure B.5 panel B. Therefore, our failure to detect a beneficial effect of bifurcations in low aspect ratio channels is consistent with our original hypothesis. When the geometry is changed to a high aspect ratio as in Figure B.5 panel C, the sidewalls become the most important binding surface. Therefore, to properly evaluate the potential for using bifurcations to enhance adsorption at the device surface, devices with higher aspect ratio channels would be needed.

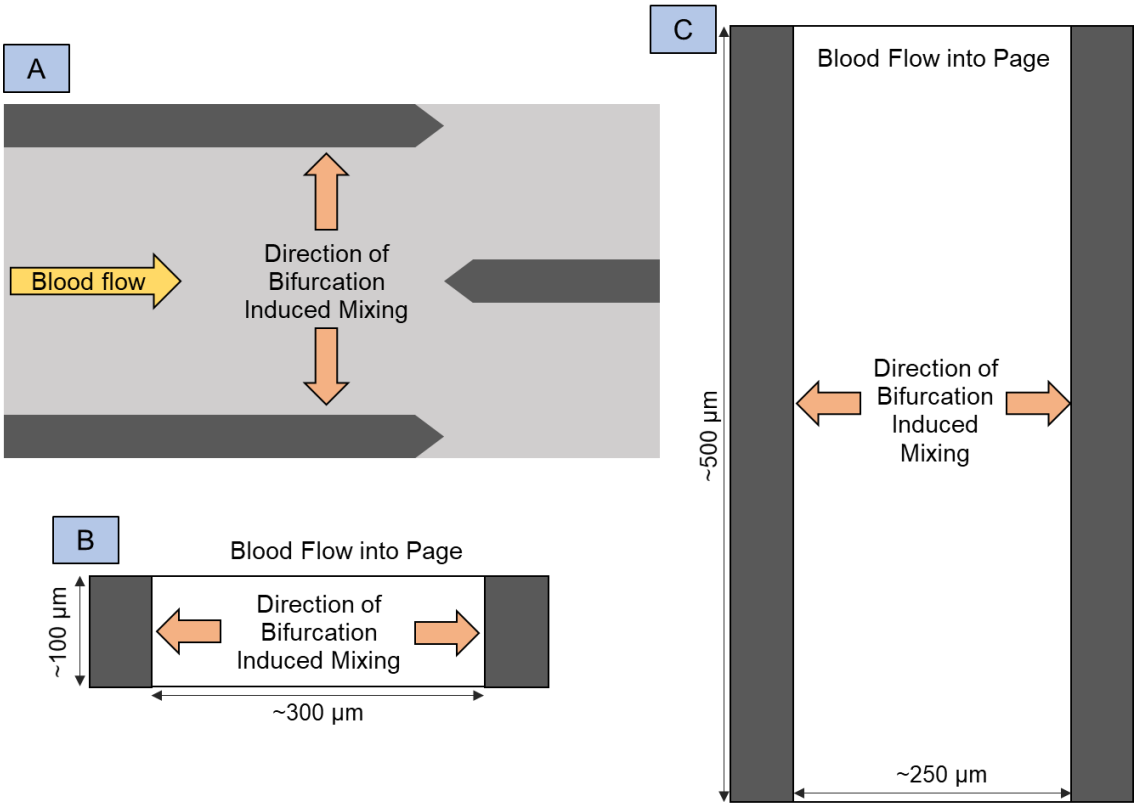

Figure B.5. Bifurcation induced mixing in low and high aspect ratio microchannels. *(A) Top-down view of the mixing strategy in which the flow is bifurcated to bring particles closer to the sidewalls. (B) Cross section and dimensions of the original low aspect ratio devices. The sidewalls make up small portion of the surface area, so splitting the flow at the bifurcations is expected to have relatively little effect on the binding potential for endotoxin. (C) Cross section of a high aspect ratio device, where the sidewalls make up most of the surface area. In this case, bifurcations are expected to have a substantial effect on endotoxin binding.*

Development of a rapid fabrication process for high aspect ratio devices

Different methods for fabrication of high aspect ratio microfluidic devices in thermoplastics and improving techniques to enable higher aspect ratios has been an active area of research [188, 192-194]. For the previously explained rationale, the goal was to dramatically increase the aspect ratio in our devices from ~1:3 (Figure B.5 panel B) to 2:1 (Figure B 5 panel C) or possibly even higher. We had originally had masters made by photochemical machining which resulted in robust stainless steel master plates that could be used almost indefinitely without breaking. However, this process could only achieve aspect ratios of about 1:2 with high variability in channel-to-channel depth. Figure B 6 shows the process flow for creating microfluidic devices with this method.

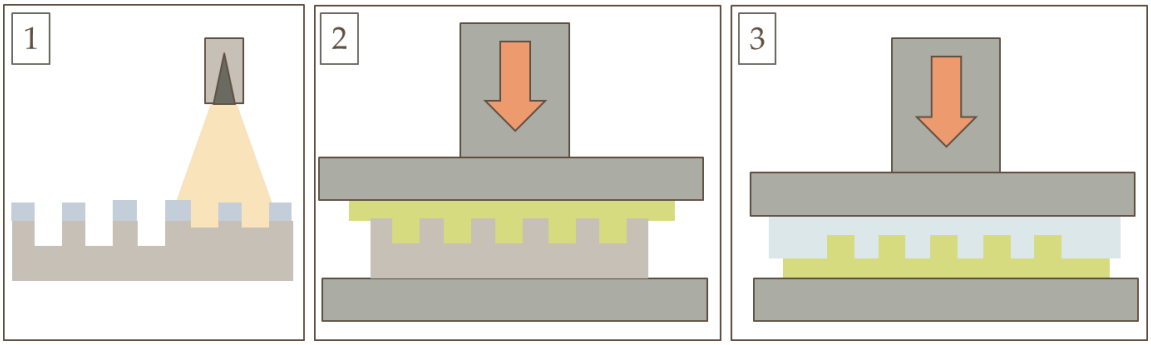

Figure B.6. Overview of the photochemical machining and hot embossing process. *(1) A metal master plate with negative features is etched by spraying an etchant to corrode the exposed metal under a patterned photoresist. (2) The metal master is embossed into PEI creating a PEI master with positive features. (3) The PEI master is hot embossed to create multiple polycarbonate lamina.*

In order to achieve such a high aspect ratio, direct laser machining of polyetherimide (PEI) was employed. PEI is very amiable to laser machining due to its high temperature tolerance and its ability to be ablated with laser machining. The lasered features would form the positive features in the polycarbonate lamina, so this needed to be done in a raised portion of the PEI. In order to achieve this, a PEI lamination process was developed in which a cutout piece of PEI that formed the outline of the device was heat laminated using the embossing machine onto a backing plate of PEI to form the raised features for patterning. This process is shown in further detail in Figure B 7. Due to the propensity of the laminated piece to separate from the backing plate, this heat lamination step was later replaced by embossing PEI against a milled aluminum block to provide the positive feature for laser patterning, which is discussed in detail in Chapter 4. Laser etching was performed using a modified laser protocol that performs each laser pass once instead of repeated passes on the same features to prevent thermal heat soak and resultant warping of the channels. The PEI master was thoroughly cleaned of carbon buildup with Alconox and water in a sonic cleaner and was then ready for polycarbonate embossing.

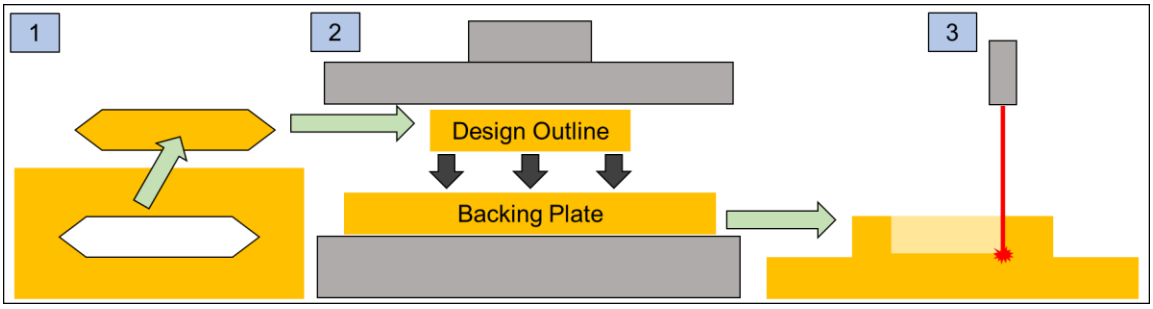

Figure B.7. The first "heat lamination" method for creating a high aspect ratio PEI master. *(1) Laser cut the outline of the device. (2) Heat and pressure laminate the design outline onto a backing plate creating the positive portion of the PEI master. (3) Laser ablate the PEI to create the desired microchannel array. Ablated regions will result in positive features (e.g., channel walls) in the polycarbonate after embossing.*

For polycarbonate embossing we used a modified procedure very similar to that used for the previous low aspect ratio devices. The main difference was that increased time and temperature was necessary to allow for the polycarbonate to flow to the bottom of the deeper channels. In addition, silicone mold release spray was used to facilitate separation of the polycarbonate from the PEI master after embossing. One artifact of the embossing process was a small lip around the outline of the device that appeared to be from the initial lamination of the two PEI pieces which was no longer present after switching to the process in Chapter 4. In order to remove this and also ensure a good seal along each channel, a quick polishing step was employed on the final piece. The polycarbonate lamina shown in Figure B.8 has a channel aspect ratio of about 2:1. The channel walls are about 100 μm wide and have an even higher aspect ratio of about 5:1.

We later were able to achieve even higher channel aspect ratios by decreasing the channel width, as discussed in Chapter 4.

Figure B.8. Magnified view of a high aspect ratio polycarbonate lamina showing the deeper header and the uniformly tall fins that form the channels*. The channels are 250 µm wide and over 500 µm tall before they are polished flat. The fins that form the channel walls are ~100 µm wide at the middle and form nearly rectangular channels.*

While none of these modifications produced a beneficial effect from bifurcation induced mixing, the work presented here represents a substantial step forward in both the design and fabrication of microfluidic devices. Decreasing the channel width improved device performance by promoting shear-induced RBC movement and the concomitant lateral mixing to drive endotoxin to the device sidewalls. Additionally, the height of these devices gives them a relatively large overall volume, allowing a larger processing volume

per device area which would result in simpler scale up. Finally, the fabrication process developed could benefit other fields of microfluidics outside of blood processing where high-aspect ratio polymer devices are needed.

BIBLIOGRAPHY

1. Jackson, W.A., *A short guide to humoral medicine.* Trends in Pharmacological Sciences, 2001. **22**(9): p. 487-489.
2. Kuriyama, S., *Interpreting the History of Bloodletting.* Journal of the History of Medicine and Allied Sciences, 1995. **50**(1): p. 11-46.
3. Botero, J.S.H. and M.C.F. Pérez, *The history of sepsis from ancient Egypt to the XIX century*, in *Sepsis-an ongoing and significant challenge*. 2012, InTech.
4. Giangrande, P.L.F., *The history of blood transfusion.* British Journal of Haematology, 2000. **110**(4): p. 758-767.
5. Hustin, A., *Note sure une nouvelle méthode de transfusion.* Annales et Bulletin des Séances Société des Sciences Médicales et Naturelles de Bruxelles, 1914. **72**: p. 104-111.
6. Weil, R., *Sodium citrate in the transfusion of blood.* Journal of the American Medical Association, 1915. **64**(5): p. 425-426.
7. Barrowcliffe, T., *History of heparin*, in *Heparin-A Century of progress*. 2012, Springer. p. 3-22.
8. Greenwalt, T., *A short history of transfusion medicine.* Transfusion, 1997. **37**(5): p. 550-563.
9. Hurst, J.W., W.B. Fye, and H.G. Zimmer, *The heart‐lung machine was invented twice—the first time by Max von Frey.* Clinical Cardiology: An International Indexed and Peer-Reviewed Journal for Advances in the Treatment of Cardiovascular Disease, 2003. **26**(9): p. 443-445.

10. Cross, T.A.N.R. *Blood Needs & Blood Supply*. 2018 [cited 2018 August 23]; Available from: https://www.redcrossblood.org/donate-blood/how-to-donate/how-blood-donations-help/blood-needs-blood-supply.html.

11. Saran, R., et al., *US renal data system 2016 annual data report: epidemiology of kidney disease in the United States.* American journal of kidney diseases, 2017. **69**(3): p. A7-A8.

12. *Report of the US Department of Health and Human Services. The 2009 national blood collection and utilization survey report*. 2011, Washington, DC: US Department of Health and Human Services, Office of the Assistant Secretary for Health.

13. Haynes, L.L., et al., *Clinical use of glycerolized frozen blood.* Jama, 1960. **173**(15): p. 1657-1663.

14. Pallotta, V., et al., *Red blood cell processing for cryopreservation: from fresh blood to deglycerolization.* Blood Cells Mol Dis, 2012. **48**(4): p. 226-32.

15. Arya, R.C., G. Wander, and P. Gupta, *Blood component therapy: which, when and how much.* Journal of anaesthesiology, clinical pharmacology, 2011. **27**(2): p. 278.

16. Valeri, C.R. and G. Ragno, *Cryopreservation of human blood products.* Transfus Apher Sci, 2006. **34**(3): p. 271-87.

17. Meryman, H.T. and M. Hornblower, *Method for Freezing and Washing Red Blood-Cells Using a High Glycerol Concentration.* Transfusion, 1972. **12**(3): p. 145-156.

18. Bandarenko, N., et al., *Extended storage of AS-1 and AS-3 leukoreduced red blood cells for 15 days after deglycerolization and resuspension in AS-3 using an automated closed system.* Transfusion, 2004. **44**(11): p. 1656-62.

19. Lusianti, R.E., et al., *Rapid removal of glycerol from frozen-thawed red blood cells.* Biotechnology Progress, 2013. **29**(3): p. 609-620.

20. Lusianti, R.E. and A.Z. Higgins, *Continuous removal of glycerol from frozen-thawed red blood cells in a microfluidic membrane device.* Biomicrofluidics, 2014. **8**(5): p. 054124.

21. Zhou, X.M., et al., *A Dilution-Filtration System for Removing Cryoprotective Agents.* Journal of Biomechanical Engineering-Transactions of the Asme, 2011. **133**(2).

22. Angus, D.C., et al., *Epidemiology of severe sepsis in the United States: analysis of incidence, outcome, and associated costs of care.* Critical care medicine, 2001. **29**(7): p. 1303-1310.

23. Center, M. and W. Virginia, *Human responses to bacterial endotoxin.* Circulatory shock, 1994. **43**: p. 137-153.

24. Dellinger, R.P., et al., *Surviving Sepsis Campaign: international guidelines for management of severe sepsis and septic shock, 2012.* Intensive care medicine, 2013. **39**(2): p. 165-228.

25. Davies, B. and J. Cohen, *Endotoxin removal devices for the treatment of sepsis and septic shock.* Lancet Infectious Diseases, 2011. **11**(1): p. 65-71.

26. Ilia, S., P. Briassoulis, and G. Briassoulis, *Polymyxin B hemoperfusion in septic shock: nothing overmuch (Meden Agan)!* Journal of thoracic disease, 2017. **9**(9): p. 2716.

27. Mach, A.J. and D. Di Carlo, *Continuous scalable blood filtration device using inertial microfluidics.* Biotechnology and bioengineering, 2010. **107**(2): p. 302-311.

28. Yung, C.W., et al., *Micromagnetic-microfluidic blood cleansing device.* Lab Chip, 2009. **9**(9): p. 1171-7.

29. Hou, W.H., et al., *A microfluidics approach towards high-throughput pathogen removal from blood using margination.* Biomicrofluidics, 2012. **6**(2): p. 24115-2411513.

30. Kang, J.H., et al., *An extracorporeal blood-cleansing device for sepsis therapy.* Nature medicine, 2014. **20**(10): p. 1211.

31. Armitage, W.J., *Effect of solute concentration on intracellular water volume and hydraulic conductivity of human blood platelets.* J Physiol, 1986. **374**: p. 375-85.

32. Rule, G.S., et al., *Water Permeability of Mammalian-Cells as a Function of Temperature in the Presence of Dimethylsulfoxide - Correlation with the State of the Membrane-Lipids.* Journal of Cellular Physiology, 1980. **103**(3): p. 407-416.

33. Hempling, H.G. and S. White, *Permeability of cultured megakaryocytopoietic cells of the rat to dimethyl sulfoxide.* Cryobiology, 1984. **21**(2): p. 133-43.

34. Gilmore, J.A., et al., *Effect of Cryoprotectant Solutes on Water Permeability of Human Spermatozoa.* Biology of Reproduction, 1995. **53**(5): p. 985-995.

35. McGrath, J.J., *Quantitative measurement of cell membrane transport: technology and applications.* Cryobiology, 1997. **34**(4): p. 315-34.

36. Elmoazzen, H.Y., J.A. Elliott, and L.E. McGann, *Osmotic transport across cell membranes in nondilute solutions: a new nondilute solute transport equation.* Biophys J, 2009. **96**(7): p. 2559-71.

37. Unhale, S.A., *Cryobiology of Cell and Tissue Cryopreservation: Experimental and Theoretical Analysis*, in *Mechanical Engineering*. 2011, University of Arizona.

38. Carlsen, A. and J.O. Wieth, *Glycerol transport in human red cells.* Acta Physiol Scand, 1976. **97**(4): p. 501-13.

39. Smith, A.U., *Prevention of Haemolysis During Freezing and Thawing of Red Blood Cells.* Lancet, 1950. **2**: p. 910-11.

40. Sloviter, H., *Recovery of human red blood-cells after freezing.* The Lancet, 1951. **257**(6659): p. 823-824.

41. Valeri, C.R., et al., *A multicenter study of in vitro and in vivo values in human RBCs frozen with 40-percent (wt/vol) glycerol and stored after deglycerolization for 15 days at 4 degrees C in AS-3: assessment of RBC processing in the ACP 215.* Transfusion, 2001. **41**(7): p. 933-939.

42. Brecher, M.E., *Technical Manual*. 2005, Bethesda, MD: AABB.

43. Scott, K.L., J. Lecak, and J.P. Acker, *Biopreservation of red blood cells: Past, present, and future.* Transfusion Medicine Reviews, 2005. **19**(2): p. 127-142.

44. Mathai, J.C., et al., *Functional analysis of aquaporin-1 deficient red cells. The Colton-null phenotype.* Journal of Biological Chemistry, 1996. **271**(3): p. 1309-13.

45. Yang, B. and A.S. Verkman, *Water and glycerol permeabilities of aquaporins 1-5 and MIP determined quantitatively by expression of epitope-tagged constructs in Xenopus oocytes.* Journal of Biological Chemistry, 1997. **272**(26): p. 16140-6.

46. Roudier, N., et al., *Evidence for the presence of aquaporin-3 in human red blood cells.* J Biol Chem, 1998. **273**(14): p. 8407-12.

47. Lucien, N., et al., *Antigenic and functional properties of the human red blood cell urea transporter hUT-B1.* Journal of Biological Chemistry, 2002. **277**(37): p. 34101-8.

48. Roudier, N., et al., *AQP3 deficiency in humans and the molecular basis of a novel blood group system, GIL.* Journal of Biological Chemistry, 2002. **277**(48): p. 45854-9.

49. Kleinhans, F.W., *Membrane permeability modeling: Kedem-Katchalsky vs a two-parameter formalism.* Cryobiology, 1998. **37**(4): p. 271-289.

50. Jacobs, M.H., *The exchange of material between the erythrocyte and its surroundings.* The Harvey Lectures, 1927. **22**: p. 146-164.

51. Jacobs, M.H. and D.R. Stewart, *A simple method for the quantitative measurement of cell permeability.* Journal of Cellular and Comparative Physiology, 1932. **1**(1): p. 71-82.

52. Finkelstein, A., *Water movement through lipid bilayers, pores, and plasma membranes: theory and reality*. 1987, New York: Wiley.

53. Kolber, A.R. and P.G. LeFevre, *Evidence for carrier-mediated transport of monosaccharides in the Ehrlich ascites tumor cell.* Journal of General Physiology, 1967. **50**(7): p. 1907-28.

54. Kedem, O. and A. Katchalsky, *Thermodynamic analysis of the permeability of biological membranes to non-electrolytes.* Biochimica et Biophysica Acta, 1958. **27**: p. 229-246.

55. McGrath, J. and K. Diller, eds. *Low Temperature Biotechnology: Emerging Applications and Engineering Contributions*. 1988, American Society of Mechanical Engineers: New York. 203-211.

56. Fettiplace, R. and D.A. Haydon, *Water Permeability of Lipid-Membranes.* Physiological Reviews, 1980. **60**(2): p. 510-550.

57. Moura, T.F., et al., *Thermodynamics of all-or-none water channel closure in red cells.* Journal of Membrane Biology, 1984. **81**(2): p. 105-11.

58. Papanek, T.H., *The Water Permeability of the Human Erythrocyte in the Temperature Range +25°C to -10°C, PhD Thesis*. 1978, Massachusetts Institute of Technology.

59. Campos, E., et al., *Lack of Aquaporin 3 in bovine erythrocyte membranes correlates with low glycerol permeation.* Biochem Biophys Res Commun, 2011. **408**(3): p. 477-81.

60. Vieira, F.L., R.I. Sha'afi, and A.K. Solomon, *The state of water in human and dog red cell membranes.* Journal of General Physiology, 1970. **55**(4): p. 451-66.

61. Macey, R.I., D.M. Karan, and R.E. Farmer, *Properties of water channels in human red cells.* Biomembranes, 1972. **3**: p. 331-40.

62. Wang, *Self-diffusion and Structure of Liquid Water. III. Measurement of the Self-diffusion of Liquid Water with H2, H3 and O18 as Tracers.* Journal of the American Chemical Society, 1953. **75**(2): p. 466-470.

63. Elmoazzen, H.Y., J.A.W. Elliott, and L.E. McGann, *The effect of temperature on membrane hydraulic conductivity.* Cryobiology, 2002. **45**(1): p. 68-79.

64. Verkman, A.S., et al., *Water transport across mammalian cell membranes.* American Journal of Physiology-Cell Physiology, 1996. **39**(1): p. C12-C30.

65. Cass, A. and A. Finkelstein, *Water permeability of thin lipid membranes.* Journal of General Physiology, 1967. **50**(6): p. 1765-84.

66. Brahm, J., *Diffusional water permeability of human erythrocytes and their ghosts.* Journal of General Physiology, 1982. **79**(5): p. 791-819.

67. Paganelli, C.V. and A.K. Solomon, *The rate of exchange of tritiated water across the human red cell membrane.* Journal of General Physiology, 1957. **41**(2): p. 259-77.

68. Osberghaus, U., H. Schonert, and B. Deuticke, *A simple technique of measuring high membrane permeabilities of human erythrocytes.* Journal of Membrane Biology, 1982. **68**(1): p. 29-35.

69. Terwilliger, T.C. and A.K. Solomon, *Osmotic water permeability of human red cells.* J Gen Physiol, 1981. **77**(5): p. 549-70.

70. Mlekoday, H.J., R. Moore, and D.G. Levitt, *Osmotic water permeability of the human red cell. Dependence on direction of water flow and cell volume.* Journal of General Physiology, 1983. **81**(2): p. 213-20.

71. Macey, R.I. and R.E. Farmer, *Inhibition of water and solute permeability in human red cells.* Biochimica et Biophysica Acta, 1970. **211**(1): p. 104-6.

72. Denker, B.M., et al., *Identification, purification, and partial characterization of a novel Mr 28,000 integral membrane protein from erythrocytes and renal tubules.* Journal of Biological Chemistry, 1988. **263**(30): p. 15634-42.

73. Preston, G.M. and P. Agre, *Isolation of the cDNA for erythrocyte integral membrane protein of 28 kilodaltons: member of an ancient channel family.* Proceedings of the National Academy of Sciences of the United States of America, 1991. **88**(24): p. 11110-4.

74. Preston, G.M., et al., *Appearance of water channels in Xenopus oocytes expressing red cell CHIP28 protein.* Science, 1992. **256**(5055): p. 385-7.

75. Yang, B. and A.S. Verkman, *Analysis of double knockout mice lacking aquaporin-1 and urea transporter UT-B. Evidence for UT-B-facilitated water transport in erythrocytes.* Journal of Biological Chemistry, 2002. **277**(39): p. 36782-6.

76. Saari, J.T. and J.S. Beck, *Hypotonic hemolysis of human red blood cells: a two-phase process.* Journal of Membrane Biology, 1975. **23**(3-4): p. 213-26.

77. Rich, G.T., et al., *Effect of osmolality on the hydraulic permeability coefficient of red cells.* J Gen Physiol, 1968. **52**(6): p. 941-54.

78. Farmer, R.E. and R.I. Macey, *Perturbation of red cell volume: rectification of osmotic flow.* Biochimica et Biophysica Acta, 1970. **196**(1): p. 53-65.

79. Levin, S.W., et al., *Improved stop-flow apparatus to measure permeability of human red cells and ghosts.* Journal of Biochemical and Biophysical Methods, 1980. **3**(5): p. 255-72.

80. Toon, M.R. and A.K. Solomon, *Transport parameters in the human red cell membrane: solute-membrane interactions of hydrophilic alcohols and their effect on permeation.* Biochim Biophys Acta, 1990. **1022**(1): p. 57-71.

81. Sha'afi, R.I., et al., *The effect of the unstirred layer on human red cell water permeability.* J Gen Physiol, 1967. **50**(5): p. 1377-99.

82. Sidel, V.W. and A.K. Solomon, *Entrance of water into human red cells under an osmotic pressure gradient.* J Gen Physiol, 1957. **41**(2): p. 243-57.

83. Naccache, P. and R.I. Sha'afi, *Patterns of nonelectrolyte permeability in human red blood cell membrane.* J Gen Physiol, 1973. **62**(6): p. 714-36.

84. Chuenkhum, S. and Z.F. Cui, *The parameter conversion from the Kedem-Katchalsky model into the two-parameter model.* Cryoletters, 2006. **27**(3): p. 185-199.

85. Le Fevre, P., *Evidence of active transfer of certain non-electrolytes across the human red cell membrane.* Journal of General Physiology, 1948. **31**(6): p. 505-27.

86. Jacobs, M.H., H.N. Glassman, and A.K. Parpart, *Osmotic properties of the erythrocyte. VII. The temperature coefficients of certain hemolytic processes.* Journal of Cellular and Comparative Physiology, 1935. **7**(2): p. 197-225.

87. de Gier, J., L.L. van Deenen, and K.G. van Senden, *Glycerol permeability of erythrocytes.* Experientia, 1966. **22**(1): p. 20-1.

88. Mazur, P. and R.H. Miller, *Permeability of Human Erythrocyte to Glycerol in 1 and 2 M Solutions at 0 or 20 Degrees C.* Cryobiology, 1976. **13**(5): p. 507-522.

89. De Gier, J., et al., *On the mechanism of non-electrolyte permeation through lipid bilayers and through biomembranes.* Biochimica et Biophysica Acta, 1971. **233**(3): p. 610-8.

90. Tirri, L.J., et al., *Studies on the hydrogen belts of membranes: II. Non-electrolyte permeability of liposomes of diester, diether, and dialkyl phosphatidylcholine and cholesterol.* Lipids, 1977. **12**(10): p. 863-8.

91. Jacobs, M.H. and S.A. Corson, *The influence of minute traces of copper on certain hemolytic processes.* Biological Bulletin, 1934. **67**(2): p. 325-326.

92. Stein, W.D. and J.F. Danielli, *Structure and function in red cell permeability.* Discussions of the Faraday Society, 1956. **21**: p. 238-251.

93. Deuticke, B., *Properties and structural basis of simple diffusion pathways in the erythrocyte membrane.* Rev Physiol Biochem Pharmacol, 1977. **78**: p. 1-97.

94. Stein, W.D., *Spontaneous and enzyme-induced dimer formation and its role in membrane permeability. II. The mechanism of movement of glycerol across the human erythrocyte membrane.* Biochim Biophys Acta, 1962. **59**: p. 47-65.

95. Echevarria, M., E.E. Windhager, and G. Frindt, *Selectivity of the renal collecting duct water channel aquaporin-3.* Journal of Biological Chemistry, 1996. **271**(41): p. 25079-82.

96. Ishibashi, K., et al., *Molecular cloning and expression of a member of the aquaporin family with permeability to glycerol and urea in addition to water expressed at the basolateral membrane of kidney collecting duct cells.*

Proceedings of the National Academy of Sciences of the United States of America, 1994. **91**(14): p. 6269-73.

97. Zeuthen, T. and D.A. Klaerke, *Transport of water and glycerol in aquaporin 3 is gated by H(+).* Journal of Biological Chemistry, 1999. **274**(31): p. 21631-6.

98. Zelenina, M., et al., *Copper inhibits the water and glycerol permeability of aquaporin-3.* Journal of Biological Chemistry, 2004. **279**(50): p. 51939-43.

99. Hunter, F.R., *Facilitated Diffusion in Human Erythrocytes.* Biochimica et Biophysica Acta, 1970. **211**(2): p. 216-222.

100. Ishii, M., et al., *Dual functional characteristic of human aquaporin 10 for solute transport.* Cellular Physiology and Biochemistry, 2011. **27**(6): p. 749-56.

101. Ohgusu, Y., et al., *Functional characterization of human aquaporin 9 as a facilitative glycerol carrier.* Drug Metabolism and Pharmacokinetics, 2008. **23**(4): p. 279-84.

102. Jay, A.W. and S. Rowlands, *The stages of osmotic haemolysis.* J Physiol, 1975. **252**(3): p. 817-32.

103. Du, J.Y., et al., *Human Spermatozoa Glycerol Permeability and Activation-Energy Determined by Electron-Paramagnetic-Resonance.* Biochimica et Biophysica Acta-Biomembranes, 1994. **1194**(1): p. 1-11.

104. Owen, J.D. and E.M. Eyring, *Reflection coefficients of permeant molecules in human red cell suspensions.* J Gen Physiol, 1975. **66**(2): p. 251-65.

105. Goldstein, D.A. and A.K. Solomon, *Determination of equivalent pore radius for human red cells by osmotic pressure measurement.* J Gen Physiol, 1960. **44**: p. 1-17.

106. Levitt, D.G. and H.J. Mlekoday, *Reflection coefficient and permeability of urea and ethylene glycol in the human red cell membrane.* J Gen Physiol, 1983. **81**(2): p. 239-53.

107. Macey, R.I. and D.M. Karan, *Independence of water and solute pathways in human RBCs.* Journal of Membrane Biology, 1993. **134**(3): p. 241-50.

108. Katkov, II, *A two-parameter model of cell membrane permeability for multisolute systems.* Cryobiology, 2000. **40**(1): p. 64-83.

109. Benson, J.D., A.J. Kearsley, and A.Z. Higgins, *Mathematical optimization of procedures for cryoprotectant equilibration using a toxicity cost function.* Cryobiology, 2012. **64**(3): p. 144-151.

110. Davidson, A.F., J.D. Benson, and A.Z. Higgins, *Mathematically optimized cryoprotectant equilibration procedures for cryopreservation of human oocytes.* Theoretical Biology and Medical Modelling, 2014. **11**.

111. Benson, J.D., *Modeling and Optimization of Cryopreservation*, in *Methods in Molecular Biology (Methods and Protocols)*, W. Wolkers and H. Oldenhof, Editors. 2015, Springer: New York, NY.

112. Mullen, S.F., et al., *Human oocyte vitrification: the permeability of metaphase II oocytes to water and ethylene glycol and the appliance toward vitrification.* Fertility and Sterility, 2008. **89**(6): p. 1812-1825.

113. Curry, M.R., B. Shachar-Hill, and A.E. Hill, *Single water channels of aquaporin-1 do not obey the Kedem-Katchalsky equations.* Journal of Membrane Biology, 2001. **181**(2): p. 115-23.

114. Toon, M. and A. Solomon, *Permeability and reflection coefficients of urea and small amides in the human red cell.* Journal of Membrane Biology, 1996. **153**(2): p. 137-146.

115. Verkman, A.S., *Aquaporins at a glance.* J Cell Sci, 2011. **124**(Pt 13): p. 2107-12.

116. Hara-Chikuma, M. and A.S. Verkman, *Physiological roles of glycerol-transporting aquaporins: the aquaglyceroporins.* Cell Mol Life Sci, 2006. **63**(12): p. 1386-92.

117. Prieto-Martinez, N., et al., *Aquaglyceroporins 3 and 7 in bull spermatozoa: identification, localisation and their relationship with sperm cryotolerance.* Reprod Fertil Dev, 2017. **29**(6): p. 1249-1259.

118. Jin, B., et al., *Rapid movement of water and cryoprotectants in pig expanded blastocysts via channel processes: its relevance to their higher tolerance to cryopreservation.* Biol Reprod, 2013. **89**(4): p. 87.

119. Wusteman, M.C., et al., *Vitrification media: toxicity, permeability, and dielectric properties.* Cryobiology, 2002. **44**(1): p. 24-37.

120. Mukherjee, I.N., Y.C. Song, and A. Sambanis, *Cryoprotectant delivery and removal from murine insulinomas at vitrification-relevant concentrations.* Cryobiology, 2007. **55**(1): p. 10-18.

121. Davidson, A.F., et al., *Toxicity Minimized Cryoprotectant Addition and Removal Procedures for Adherent Endothelial Cells.* PLoS One, 2015. **10**(11): p. e0142828.

122. Lovelock, J.E., *The mechanism of the protective action of glycerol against haemolysis by freezing and thawing.* Biochimica et Biophysica Acta, 1953. **11**(1): p. 28-36.

123. Valeri, C.R., et al., *In vivo survival of apheresis RBCs, frozen with 40-percent (wt/vol) glycerol, deglycerolized in the ACP 215, and stored at 4 degrees C in AS-3 for up to 21 days.* Transfusion, 2001. **41**(7): p. 928-932.

124. Henkelman, S., et al., *Utilization and quality of cryopreserved red blood cells in transfusion medicine.* Vox sanguinis, 2015. **108**(2): p. 103-112.

125. Lahmann, J.M., J.D. Benson, and A.Z. Higgins, *Concentration dependence of the cell membrane permeability to cryoprotectant and water and implications for design of methods for post-thaw washing of human erythrocytes.* Cryobiology, 2018. **80**: p. 1-11.

126. Lovelock, J.E., *The haemolysis of human red blood-cells by freezing and thawing.* Biochim Biophys Acta, 1953. **10**(3): p. 414-26.

127. Pegg, D.E. and M.P. Diaper, *On the mechanism of injury to slowly frozen erythrocytes.* Biophysical Journal, 1988. **54**(3): p. 471-88.

128. Mazur, P. and K.W. Cole, *Roles of unfrozen fraction, salt concentration, and changes in cell volume in the survival of frozen human erythrocytes.* Cryobiology, 1989. **26**(1): p. 1-29.

129. Fahy, G.M., *The Relevance of Cryoprotectant Toxicity to Cryobiology.* Cryobiology, 1986. **23**(1): p. 1-13.

130. Meryman, H.T., *Modified model for the mechanism of freezing injury in erythrocytes.* Nature, 1968. **218**(5139): p. 333-6.

131. Vian, A.M. and A.Z. Higgins, *Membrane permeability of the human granulocyte to water, dimethyl sulfoxide, glycerol, propylene glycol and ethylene glycol.* Cryobiology, 2014. **68**(1): p. 35-42.

132. Waterman, C.S., et al., *Improved measurement of erythrocyte volume distribution by aperture-counter signal analysis.* Clin Chem, 1975. **21**(9): p. 1201-11.

133. Kim, Y.R. and L. Ornstein, *Isovolumetric sphering of erythrocytes for more accurate and precise cell volume measurement by flow cytometry.* Cytometry, 1983. **3**(6): p. 419-427.

134. Fung, Y.C. and P. Tong, *Theory of the sphering of red blood cells.* Biophys J, 1968. **8**(2): p. 175-98.

135. Savitz, D., V.W. Sidel, and A.K. Solomon, *Osmotic Properties of Human Red Cells.* J Gen Physiol, 1964. **48**: p. 79-94.

136. Jay, A.W., *Geometry of the human erythrocyte. I. Effect of albumin on cell geometry.* Biophys J, 1975. **15**(3): p. 205-22.

137. Byrd, R.H., M.E. Hribar, and J. Nocedal, *An interior point algorithm for large-scale nonlinear programming.* Siam Journal on Optimization, 1999. **9**(4): p. 877-900.

138. Byrd, R.H., J.C. Gilbert, and J. Nocedal, *A trust region method based on interior point techniques for nonlinear programming.* Mathematical Programming, 2000. **89**(1): p. 149-185.

139. Waltz, R.A., et al., *An interior algorithm for nonlinear optimization that combines line search and trust region steps.* Mathematical Programming, 2006. **107**(3): p. 391-408.

140. Han, V., K. Serrano, and D.V. Devine, *A comparative study of common techniques used to measure haemolysis in stored red cell concentrates.* Vox Sanguinis, 2010. **98**(2): p. 116-23.

141. Dumaswala, U. and T. Greenwalt, *Human erythrocytes shed exocytic vesicles in vivo.* Transfusion, 1984. **24**(6): p. 490-492.

142. Greenwalt, T. and U. Dumaswala, *Effect of red cell age on vesiculation in vitro.* British journal of haematology, 1988. **68**(4): p. 465-467.

143. Bartosz, G., *Aging of the erythrocyte IV. Spin-label studies of membrane lipids, proteins and permeability.* Biochimica et Biophysica Acta (BBA)-Biomembranes, 1981. **644**(1): p. 69-73.

144. Bartosz, G. and K. Gwozdzinski, *Aging of the erythrocyte. 23. Changes in the permeation of spin-labeled electrolytes.* American journal of hematology, 1983. **14**(4): p. 377-379.

145. Gaczyńska, M. and G. Bartosz, *Crosslinking of membrane proteins during erythrocyte ageing.* The International journal of biochemistry, 1986. **18**(4): p. 377-382.

146. Kay, M., et al., *Oxidation as a possible mechanism of cellular aging: vitamin E deficiency causes premature aging and IgG binding to erythrocytes.* Proceedings of the National Academy of Sciences, 1986. **83**(8): p. 2463-2467.

147. Rifkind, J.M., K. Araki, and E.C. Hadley, *The Relationship between the Osmotic Fragility of Human-Erythrocytes and Cell Age.* Archives of Biochemistry and Biophysics, 1983. **222**(2): p. 582-589.

148. Waugh, R.E., et al., *Rheologic properties of senescent erythrocytes: loss of surface area and volume with red blood cell age.* Blood, 1992. **79**(5): p. 1351-1358.

149. Greenwalt, T.J., D.J. Bryan, and U.J. Dumaswala, *Erythrocyte membrane vesiculation and changes in membrane composition during storage in citrate-phosphate-dextrose-adenine-1.* Vox sanguinis, 1984. **47**: p. 261-270.

150. Bosman, G.J. and M.M. Kay, *Alterations of band 3 transport protein by cellular aging and disease: erythrocyte band 3 and glucose transporter share a functional relationship.* Biochemistry and Cell Biology, 1990. **68**(12): p. 1419-1427.

151. Heusinkveld, R.S., et al., *Effect of protein modification on erythrocyte membrane mechanical properties*, in *Red Cell Rheology*. 1978, Springer. p. 175-182.

152. Kay, M., et al., *Senescent cell antigen is immunologically related to band 3.* Proceedings of the National Academy of Sciences, 1983. **80**(6): p. 1631-1635.

153. Carruthers, A. and D. Melchior, *Study of the relationship between bilayer water permeability and bilayer physical state.* Biochemistry, 1983. **22(**25): p. 5797-5807.

154. Alshalani, A. and J.P. Acker, *Red blood cell membrane water permeability increases with length of ex vivo storage.* Cryobiology, 2017. **76**: p. 51-58.

155. Araki, K. and J.M. Rifkind, *The rate of osmotic hemolysis A relationship with membrane bilayer fluidity.* Biochimica et Biophysica Acta (BBA)-Biomembranes, 1981. **645**(1): p. 81-90.

156. Zade-Oppen, A.M., *Posthypertonic hemolysis in sodium chloride systems.* Acta Physiologica Scandinavica, 1968. **73**(3): p. 341-64.

157. Farrant, J. and G.J. Morris, *Thermal shock and dilution shock as the causes of freezing injury.* Cryobiology, 1973. **10**(2): p. 134-140.

158. Muldrew, K., *The salting-in hypothesis of post-hypertonic lysis.* Cryobiology, 2008. **57**(3): p. 251-256.

159. Rudenko, S.V. and S.V. Patelaros, *Cation-sensitive pore formation in rehydrated erythrocytes.* Biochimica et Biophysica Acta (BBA)-Biomembranes, 1995. **1235**(1): p. 1-9.

160. Conner, A.C., R.M. Bill, and M.T. Conner, *An emerging consensus on aquaporin translocation as a regulatory mechanism.* Molecular membrane biology, 2013. **30**(1): p. 101-112.

161. Kitchen, P., et al., *Identification and molecular mechanisms of the rapid tonicity-induced relocalization of aquaporin 4.* Journal of Biological Chemistry, 2015: p. jbc. M115. 646034.

162. Buemi, M., et al., *AQP1 in red blood cells of uremic patients during hemodialytic treatment.* Nephron, 2002. **92**(4): p. 846-852.

163. Antonelou, M.H., et al., *Oxidative stress-associated shape transformation and membrane proteome remodeling in erythrocytes of end stage renal disease patients on hemodialysis.* Journal of proteomics, 2011. **74**(11): p. 2441-2452.

164. Gottfried, E.L. and N.A. Robertson, *Glycerol lysis time as a screening test for erythrocyte disorders.* The Journal of laboratory and clinical medicine, 1974. **83**(2): p. 323-333.

165. Hashimoto, N., et al., *Cell electrophoretic mobility and glycerol lysis of human erythrocytes in various diseases.* Electrophoresis, 1998. **19**(7): p. 1227-1230.

166. Posteraro Jr, A. and E.L. Gottfried, *The diagnostic significance of a prolonged erythrocytic glycerol lysis time (GLT50).* American journal of clinical pathology, 1978. **70**(4): p. 637-641.

167. Zanella, A., et al., *Acidified glycerol lysis test: a screening test for spherocytosis.* British journal of haematology, 1980. **45**(3): p. 481-486.

168. Eber, S., et al., *Prevalence of increased osmotic fragility of erythrocytes in German blood donors: screening using a modified glycerol lysis test.* Annals of hematology, 1992. **64**(2): p. 88-92.

169. Bogadi-Are, A., et al., *Red blood cell glycerol lysis and hematologic effects in occupational benzene exposure.* Toxicology and industrial health, 1997. **13**(4): p. 485-494.

170. Sauer, A., et al., *Kinetics of hemolysis of normal and abnormal red blood cells in glycerol-containing media.* Biochimica et Biophysica Acta (BBA)-Biomembranes, 1991. **1063**(2): p. 203-208.

171. Van den Abbeel, E., et al., *Osmotic responses and tolerance limits to changes in external osmolalities, and oolemma permeability characteristics, of human in vitro matured MII oocytes.* Hum Reprod, 2007. **22**(7): p. 1959-72.

172. Paoli, C.J., et al., *Epidemiology and Costs of Sepsis in the United States-An Analysis Based on Timing of Diagnosis and Severity Level.* Critical care medicine, 2018.

173. Dellinger, R.P., *Cardiovascular management of septic shock.* Critical care medicine, 2003. **31**(3): p. 946-955.

174. Suffredini, A.F., et al., *The cardiovascular response of normal humans to the administration of endotoxin.* New England Journal of Medicine, 1989. **321**(5): p. 280-287.

175. Shum, H., W. Yan, and D. Chan, *Extracorporeal blood purification for sepsis.* Hong Kong Medical Journal, 2016.

176. Rimmelé, T. and J.A. Kellum, *Clinical review: blood purification for sepsis.* Critical Care, 2011. **15**(1): p. 205.

177. Shimizu, T., T. Miyake, and M. Tani, *History and current status of polymyxin B-immobilized fiber column for treatment of severe sepsis and septic shock.* Annals of gastroenterological surgery, 2017. **1**(2): p. 105-113.

178. Ronco, C. and D.J. Klein, *Polymyxin B hemoperfusion: a mechanistic perspective.* Critical Care, 2014. **18**(3): p. 309.

179. Zhang, M., et al., *Extracorporeal endotoxin removal by novel l-serine grafted PVDF membrane modules.* Journal of membrane science, 2012. **405**: p. 104-112.

180. Wu, Q., et al., *Fabrication of membrane absorbers based on amphiphilic carbonaceous derivatives for selective endotoxin clearance.* Journal of Materials Chemistry B, 2017. **5**(41): p. 8219-8227.

181. Hou, H.W., et al., *Microfluidic devices for blood fractionation.* Micromachines, 2011. **2**(3): p. 319-343.

182. Saadatmand, M., et al., *Fluid particle diffusion through high-hematocrit blood flow within a capillary tube.* Journal of biomechanics, 2011. **44**(1): p. 170-175.

183. Ahuja, A.S., W.R. Hendee, and P. Carson, *Transport phenomena in laminar flow of blood.* Physics in Medicine & Biology, 1978. **23**(5): p. 928.

184. Fujiwara, H., et al., *Red blood cell motions in high-hematocrit blood flowing through a stenosed microchannel.* Journal of Biomechanics, 2009. **42**(7): p. 838-843.

185. Cha, W. and R.L. Beissinger, *Evaluation of shear-induced particle diffusivity in red cell ghosts suspensions.* Korean Journal of Chemical Engineering, 2001. **18**(4): p. 479-485.

186. Aarts, P.A., et al., *Blood platelets are concentrated near the wall and red blood cells, in the center in flowing blood.* Arteriosclerosis: An Official Journal of the American Heart Association, Inc., 1988. **8**(6): p. 819-824.

187. Narasimhan, J. and I. Papautsky, *Polymer embossing tools for rapid prototyping of plastic microfluidic devices.* Journal of Micromechanics and Microengineering, 2003. **14**(1): p. 96.

188. Shiu, P.-P., et al., *Rapid fabrication of tooling for microfluidic devices via laser micromachining and hot embossing.* Journal of Micromechanics and Microengineering, 2008. **18**(2): p. 025012.

189. Becker, H., U. Heim, and O. Roetting. *Fabrication of polymer high-aspect-ratio structures with hot embossing for microfluidic applications*. in *Microfluidic Devices and Systems II*. 1999. International Society for Optics and Photonics.

190. Ng, S. and Z. Wang, *Hot roller embossing for microfluidics: process and challenges.* Microsystem technologies, 2009. **15**(8): p. 1149-1156.

191. Yeo, L., et al., *Investigation of hot roller embossing for microfluidic devices.* Journal of Micromechanics and Microengineering, 2009. **20**(1): p. 015017.

192. Greener, J., et al., *Rapid, cost-efficient fabrication of microfluidic reactors in thermoplastic polymers by combining photolithography and hot embossing.* Lab on a Chip, 2010. **10**(4): p. 522-524.

193. Jensen, M.F., et al., *Rapid prototyping of polymer microsystems via excimer laser ablation of polymeric moulds.* Lab on a Chip, 2004. **4**(4): p. 391-395.

194. Shiu, P.-P., G.K. Knopf, and M. Ostojic, *Fabrication of metallic micromolds by laser and electro-discharge micromachining.* Microsystem technologies, 2010. **16**(3): p. 477.

195. Vahidkhah, K., S.L. Diamond, and P. Bagchi, *Hydrodynamic interaction between a platelet and an erythrocyte: effect of erythrocyte deformability, dynamics, and wall proximity.* Journal of biomechanical engineering, 2013. **135**(5): p. 051002.

196. Carciati, A., *Red blood cells under flow: blood rheology and effect of vascular endothelial cells on haemodynamics in vitro.* 2017.

197. Lima, R., et al., *Blood flow behavior in microchannels: past, current and future trends.* Single and two-phase flows on chemical and biomedical engineering, 2012: p. 513-547.

198. Fahraeus, R. and T. Lindqvist, *The viscosity of the blood in narrow capillary tubes.* American Journal of Physiology-Legacy Content, 1931. **96**(3): p. 562-568.

199. Segre, G. and A. Silberberg, *Radial particle displacements in Poiseuille flow of suspensions.* Nature, 1961. **189**(4760): p. 209.

200. Richter, W., et al., *Morphology, size distribution, and aggregate structure of lipopolysaccharide and lipid A dispersions from enterobacterial origin.* Innate immunity, 2011. **17**(5): p. 427-438.

201. Risco, C. and P. Pinto da Silva, *Binding of bacterial endotoxins to the macrophage surface: visualization by fracture-flip and immunocytochemistry.* Journal of Histochemistry & Cytochemistry, 1993. **41**(4): p. 601-608.

202. Santos, N.C., et al., *Evaluation of lipopolysaccharide aggregation by light scattering spectroscopy.* Chembiochem, 2003. **4**(1): p. 96-100.

203. Ryder, M.P., et al., *Binding interactions of bacterial lipopolysaccharide and the cationic amphiphilic peptides polymyxin B and WLBU2.* Colloids Surf B Biointerfaces, 2014. **120**: p. 81-7.

204. Paulus, J.-M., *Platelet size in man.* Blood, 1975. **46**(3): p. 321-336.

205. Burris, S., D. Weiss, and J. White, *Comparison of bovine and human platelet deformability, using micropipette elastimetry.* American journal of veterinary research, 1989. **50**(1): p. 34-38.

206. Goldsmith, H.L. and S. Spain, *Margination of leukocytes in blood flow through small tubes.* Microvascular research, 1984. **27**(2): p. 204-222.

207. Gidaspow, D. and V. Chandra, *Unequal granular temperature model for motion of platelets to the wall and red blood cells to the center.* Chemical Engineering Science, 2014. **117**: p. 107-113.

208. Goldsmith, H.L. and T. Karino, *Microscopic considerations: the motions of individual particles.* Annals of the New York Academy of Sciences, 1977. **283**(1): p. 241-255.

209. Ivanov, I., *Impedance spectroscopy of human erythrocyte membrane: Effect of frequency at the spectrin denaturation transition temperature.* Bioelectrochemistry, 2010. **78**(2): p. 181-185.

210. Ivanov, I.T., et al., *Role of membrane proteins in thermal damage and necrosis of red blood cells.* Thermochimica Acta, 2007. **456**(1): p. 7-12.

211. Weber, P.C., et al., *Structural origins of high-affinity biotin binding to streptavidin.* Science, 1989. **243**(4887): p. 85-88.